Neutron and X-Ray Scattering Studies of Metal Halide Perovskites

Haritha Sindhu Rajeev
Kozhikode, Kerala, India

Master of Science in Physics,
Indian Institute of Science Education and Research, Pune, India,
May 2019

A Dissertation presented to the Graduate Faculty of the University of Virginia in Candidacy for the Degree of Doctor of Philosophy

Department of Physics
University of Virginia
November, 2024

Committee Members:
Prof. Seung-Hun Lee
Prof. Joe Poon
Prof. Gia-Wei Chern
Prof. Prasanna Balachandran

Abstract

Metal Halide perovskites (MHPs) have emerged as promising materials for photovoltaic and light-emitting device applications. The highly dynamic nature of these systems can be beneficial to their device performance depending on the type of materials present, the temperature, pressure, and doping. This thesis discusses a combination of studies on various crystal types (powders and single crystals) under varying external conditions like temperature and doping. We used neutron and X-ray scattering as a major tool to understand the interplay of various structural dynamics and their potential impact on optoelectronic properties.

Within the MHPs, two-dimensional Hybrid Organic-Inorganic Perovskites (HOIPs) are known for their enhanced stability compared to their three-dimensional counterparts. Using time-of-flight neutron spectroscopy, we identified and quantitatively separated the vibrational and rotational dynamics of two 2D HOIPs, butylammonium lead iodide $(BA)_2PbI_4$ and phenethyl-ammonium lead iodide $(PEA)_2PbI_4$. By examining the corresponding temperature dependence, we found that the lattice vibrations, as evidenced by neutron spectra, are consistent with the lattice dynamics obtained from Raman scattering. We revealed that the rotational dynamics of organic molecules in these materials tend to suppress their photoluminescence quantum yield (PLQY). In contrast, the vibrational dynamics did not show predominant correlations with the same. Additionally, we observed photoluminescence emission peak splitting for both systems, which becomes prominent above certain critical temperatures where the suppression of PLQY begins. This study suggests that the rotational motions of polarized molecules may reduce the exciton binding energy or break the degeneracy in exciton binding energy levels, thus enhancing the non-radiative recombination rates and reducing photoluminescence yield.

Beyond structural dynamics, doping in MHPs has been known to significantly effect their light-emitting efficiency and thus their applications in scintillator materials for radiation detection. Using small angle neutron scattering on six different PbS Quantum Dot (QD) loaded (0%, 0.01%, 0.05%, 0.1%, 0.5% 1%, 2%) $CsPbBr_3$ perovskite we were able to quantify the distribution of QDs in the perovskite matrix. Based on radioluminescence (RL) measurements, we correlated how varying QD spatial distribution can affect their luminescent properties. The distance between QDs decreased and the RL intensity increased with increasing QD loading to 0.5%, beyond which the QD separation did not show a significant change, and the RL intensity decreased. We suggest the possibility of an inhomogeneous distribution of QDs with closer QDs in some areas and farther apart in others at higher QD loadings, resulting in an increased emitted photon reabsorption and reduced luminescence. We could exploit the sensitivity of luminescence properties in these materials to the spatial distribution of dopants to optimize scintillator performance tailored to specific applications.

Structural dynamics in MHPs could result in local disorders while cooling and warming. Using X-ray diffuse scattering and inelastic neutron scattering on single crystals of $\mathrm{MAPbBr_3}$, we studied how lattice dynamics vary along different crystal directions. We identified overdamping of transverse acoustic phonons along the specific Brillouin zone directions, M-R (cubic phase) and X-M (tetragonal and cubic phases), as the system transitioned through its three structural phases upon warming. This overdamping can lead to local disorders, possibly enhancing halide ion diffusion and phonon scattering, thus reducing the charge carrier lifetime and stability. We emphasize that while these phonons are primarily dominated by atomic motions from the inorganic $\mathrm{PbBr_3}$ layer, molecular rotation and organic cation diffusion appear to indirectly affect their behavior and visualization in experiments.

Overall, our studies offer a deeper understanding of the fundamental interactions in MHPs and could guide the design of more efficient light-emitting and photovoltaic materials for advanced technological applications. We emphasize the need for a more comprehensive analysis on the interplay of rotational and lattice dynamics, organic cation and halide anion diffusions, and its possible impacts on the efficiency of HOIPs in functional devices.

Author's Biogrophical Sketch

Haritha Sindhu Rajeev was born in Kozhikode, Kerala, India. She completed her bachelor's and master's degrees in Physics at the Indian Institute of Science Education and Research, Pune. After finishing her master's in 2019, she joined the PhD program in Physics at the University of Virginia. She began her research under Prof. Seung-Hun Lee in the summer of 2020. In Prof. Lee's group, she has studied crystal structures, lattice vibrational dynamics, rotational dynamics, and other optoelectronic properties of Metal Halide Perovskites, with the goal of enhancing the performance of these materials in photovoltaic and light-emitting device applications. Her collaborative projects within the research group have provided insights into the fundamental interactions in Metal Halide Perovskites, guiding the design of more efficient optoelectronic devices for advanced technological applications.

Acknowledgements

I am writing to express my sincere gratitude to my Ph.D. advisor, Prof. Seung-Hun Lee, for his continuous support and guidance throughout my research. The collaborative opportunities I received through his network helped me initiate new project ideas and advance ongoing projects to completion. I am grateful to Prof. Joshua J. Choi for allowing me to participate in various projects within applied physics and chemical engineering. I would also like to thank the members of my defense committee, Prof. Gia-Wei Chern and Prof. Prasanna Balachandran, for their valuable comments and suggestions. I would like to mention Prof. Joe Poon's continuous support and insights as a member of my PhD progress committee.

I would like to thank Dr. Maiko Kofu, Dr. Ryoichi Kajimoto, Dr. Mitsutaka Nakamura, Dr. Jong Dae Jang, Dr. Sangho Lee, Dr. Young Soo Han, Dr. Daniel M. Pajerowski, and Garrett E. Granroth for their immense help with the neutron scattering experiments. I want to thank Dr. Wei Liang Chen and Dr. Yu-Ming Chang for their assistance with Raman scattering and photoluminescence measurements and Alfred Q. R. Baron and Dr. MANJO Taishun for their support with diffuse X-ray scattering measurements. I thank Dr. Diane A. Dickie for her help with X-ray transmission measurements and Dr. Mina Yoon and Dr. Sinchul Yeom for their guidance with Density Functional Theory calculations. I sincerely thank Eric C. Johnson, Sammy Fieser, Dr. Alexander Z. Chen, and Dr. Grayson C. Johnson for providing high-quality samples for the projects. I would also like to thank Dr. Grayson C. Johnson again for assisting me in setting up a lab for single crystal synthesis and supporting my endeavors to obtain high-quality crystals successfully. I want to thank Dr. Despina Louca and Dr. John Scheenloch for their support.

I express my deepest gratitude to Dr. Xiao Hu for teaching me essential skills, from proposal writing to conducting experiments and analyzing data. The support I received from Dr. Hu as a senior student in the lab was invaluable, and it ultimately led to my coauthoring a paper with him. I am also grateful to Dr. Depei Zhang, Dr. Tianren Chen, and Dr. Sharon S. Phillip for establishing lessons and building a solid foundational platform in our research groups, which made the journey easier for new

PhD students. I would also like to thank my fellow research mates, Asiri Thennakoon and Srimal Rathnayake, for their hands-on assistance in advancing projects and all the memorable times we shared.

I am deeply grateful to my parents, Dr. N. E Rajeevan and C. V Sindhu and sister Dr. Gayathri Sindhu Rajeev for providing me with the privilege and support to focus solely on building my career without other worries. I specifically thank Ravisankar Rajagopal for being a solid pillar of emotional support throughout the ups and downs of this six-year journey. I also thank my friends Meera Mohan, Sidharth Adithyan, Archana Narayanan, Dr. Ananthesh Sundaresh and Supriyo Ghosh for their support and encouragement.

Finally, I would like to acknowledge the U.S. Department of Energy, Office of Science, Office of Basic Energy Sciences, under Award No. DE-SC001644, for supporting the work at the University of Virginia. We also express our gratitude for the support from the Material Science and Life Science Experimental Facility at the Japan Proton Accelerator Research Complex, the Korea Atomic Energy Research Institute in South Korea, Oak Ridge National Laboratory in the United States, SPring-8 (Super Photon Ring-8 GeV) in Japan, and the Institute of Physical and Chemical Research (RIKEN) in Japan for the scattering experiments conducted. We thank the Center for Condensed Matter Sciences at the National Taiwan University, the Department of Chemistry, and the Department of Chemical Engineering at the University of Virginia for their assistance with other essential experiments. The U.S. Department of Energy Office of Science, Office of Basic Energy Sciences, Materials Sciences, and Engineering Division partly supported the theoretical work. Computational work utilized resources from the Oak Ridge Leadership Computing Facility at Oak Ridge National Laboratory, supported by the Office of Science of the U.S. Department of Energy under Contract No. DE-AC05-00OR22725, as well as resources from the National Energy Research Scientific Computing Center, a DOE Office of Science User Facility supported by the Office of Science of the U.S. Department of Energy under Contract No. DE-AC02-05CH11231, utilizing NERSC award BES-ERCAP0024568.

Contents

Related Publication

The material and results of Chapter 3 of the thesis are also featured in the original archived publication of the author, along with collaboartors.

1. **H. S. Rajeev**, X. Hu, W.-L. Chen, D. Zhang, T. Chen, M. Kofu, R. Kajimoto, ...& S. -H. Lee,
   The influence of Structural Dynamics in Two-Dimensional Hybrid Organic-Inorganic Perovskites on their Photoluminescence Efficiency–Neutron scattering analysis,
   arXiv preprint arXiv:2402.15658.

The motivation in Chapter 4 of the thesis first appeared in the following publications in which the author partly collaborated.

1. A. M. Conley, E. S. Sarabamoun, K. A. Dagnall, L. U. Yoon, **H. S. Rajeev**, S.-H. Lee, J. J. Choi,
   Quantum-Dot-Doped Lead Halide Perovskites for Ionizing Radiation Detection,
   ACS Applied Optical Materials 1 (3) (2023) 715–723.

2. K. A. Dagnall, A. M. Conley, L. U. Yoon, **H. S. Rajeev**, S.-H. Lee, J. J. Choi,
   Ytterbium-Doped Cesium Lead Chloride Perovskite as an X-ray Scintillator with High Light Yield,
   ACS Omega 7 (24) (2022) 20968–20974.

List of Abbreviations

PV	Photovoltaic
LED	Light Emitting Device
MHP	Metal Halide Perovskite
HOIP	Hybrid Organic-Inorganic Perovskite
DFT	Density Functional Theory
QENS	Quasi Elastic Neutron Scattering
INS	Inelastic Neutron Scattering
SANS	Small Angle Neutron Scattering
XDS	X-Ray Diffuse Scattering
PL	Photoluminescence
RL	Radioluminescence
QD	Quantum Dot
...	

List of Figures

List of Tables

Chapter 1

Introduction - Metal Halide Perovskites

Metal halide perovskites (MHPs) have attracted substantial research interest due to their wide range of applications, including next-generation solar cells [1–6], light-emitting diodes [7–9], lasers [10, 11], and photodetectors [12, 13]. These materials are celebrated for their extended carrier lifetimes, long carrier diffusion lengths, and remarkable resistance to defects. However, challenges such as the toxicity of heavy metals and low stability under ambient conditions still remain [14, 15]. Neverthless, the high tunability of MHPs enables the synthesis and customization of new perovskite variants for a variety of functional device applications.

In this chapter, we will explore the potential of MHPs in optoelectronic applications, investigate their crystal structure, and examine their structural dynamics. We will highlight how these factors influence the performance of MHPs in optoelectronic devices.

1.1 Photovoltaic Devices

Photovoltaic (PV) devices are an essential component in the present-day world, where steps are being taken to transition from nonrenewable to renewable energy sources. Semiconductor materials used for PV applications have a band gap suitable for the efficient absorption of sunlight which photoexcites electrons, creating free charge carriers and generating electric current [16]. Compared to other power-generating sources such as fossil fuels, nuclear energy, and hydroelectric power, PV devices have their own disadvantages [17, 18]. The performance of PV devices can be significantly affected by weather conditions and they generally require a higher amount of raw materials for sufficient power generation. However, PV devices offer significant advantages over the harmful impacts of dams on aquatic resources, the geographical limitations of suitable sites for large-scale hydroelectric projects, carbon emissions from fossil fuels, the long-term disposal of nuclear waste, and the limited supply of nuclear fuels. Thus significant efforts to improve PV devices are ongoing because they offer a cleaner, more sustainable, and increasingly cost-effective solution for energy generation.

Silicon (Si) based semiconductors are conventionally used in PV devices [19]. One major drawback with Si is that it is scarce in its pure form. Hence extracting Si from their raw materials like sand and Quartzite, is highly energy intensive leading to increased production costs and carbon emissions. Additionally, obtaining high-quality Si is cruicial as even minor defects can significantly effect the optoelectronic performance in Si-based semiconductors. This is where Metal Halide Perovskites (MHPs) become a promising material for PV device applications. MHPs exhibit high defect tolerance and can function efficiently even with minor defects [20–22]. They also benefit from a straightforward solvent-based synthesis method, which makes mass production cost-effective and allows for easier tailoring of properties for diverse applications [23, 24].

Figure 1.1 shows the National Renewable Energy Laboratory (NREL) efficiency chart of various promising optoelectronic device materials [25]. Cell efficiency is defined as the ratio of the electrical power output to the power of incident sunlight. For conventional Si single crystal PV cells, the highest efficiency reported is approxi-

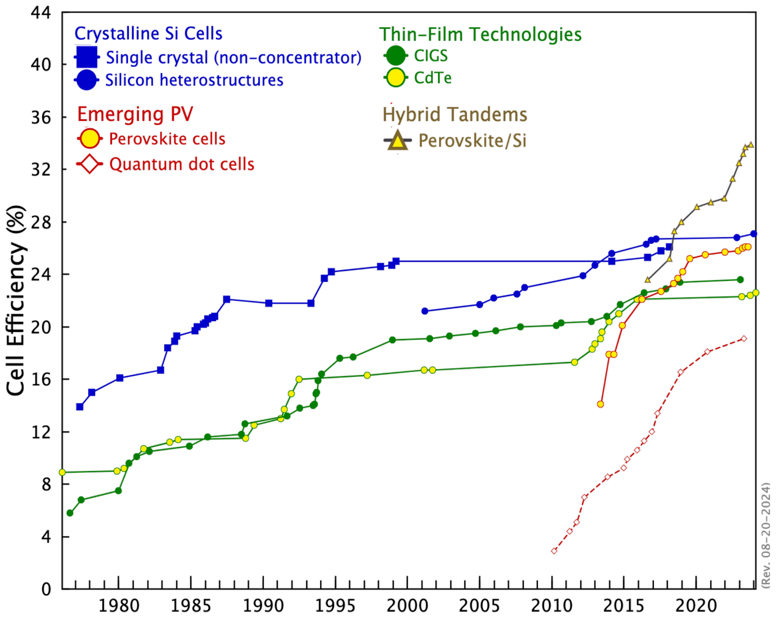

Figure 1.1: Efficency chart of various PV device materials

mately 26%. By 2024, perovskite PV cells have achieved cell efficiencies on par with Si-based semiconductors. Other PV materials, such as cadmium telluride (CdTe) thin films and quantum dots etc, have also shown promising efficiencies in the market. Recently, tandem PV cells — combining Si and perovskite PV cells — have emerged as a promising technology, showing efficiencies near 32%. However, challenges remain for scaling these tandem systems for widespread use. Nevertheless, efforts to improve the performance of all promising materials are necessary for compensating the drawbacks of one material with the strengths of another. While some materials may not be ideal for large-scale utility applications, they can be highly efficient for small-scale PV applications. Here, our main focus is on MHPs, which are now found to be the potential candidates for PV cells.

1.2 Light Emitting Devices

Light Emitting Devices (LEDs), as the name suggests emit light on absorbtion of radiation. LEDs includes devices such as light-emitting diodes, laser diodes, electroluminescent devices, and scintillators, each tailored for unique applications. Low-cost materials for efficient detection of ionizing radiation are highly desirable in fields such as high-energy physics [26], medical and non-medical X-ray imaging [27], and national security [28, 29].

There are two commonly used methods for radiation detection: direct detectors and scintillators. Direct detectors convert incoming radiation, such as X-rays, gamma or electrons, directly into an electrical signal [30–32]. In contrast, scintillators work by indirectly down-converting high-energy incoming radiation into visible or infrared light, which can then be detected by standard photodetectors [33, 34]. For direct detectors, there is a trade-off between charge carrier generation and high-energy photon stopping power [32]. High stopping power often comes with a disadvantage of increased radiation damage, which can effect the charge carrier generation and charge transport properties in detectors. Scintillators mitigate this issue differently: they use a luminescent mechanism to convert high-energy photons into lower-energy visible or infrared photons, which are then detected by photodetectors that convert the light into an electrical signal. By separating the functions of photon absorption and signal generation into two different materials, scintillators avoid the direct trade-off faced by direct detectors, but they still rely on the efficiency of both the scintillation and detection processes for optimal performance.

Conventional scintillator materials such as Cesium Iodide with Thallium Dopant (CsI:Tl) and Lutetium Iodide with Cerium Dopant (LuI_3:Ce^{3+}) are typically grown as single crystals [35]. This is expensive and difficult to apply in large devices. This is where the low-cost solvent-based synthesis and easy tunability of MHPs become advantageous. Research efforts are now focused on developing scintillator materials based on Lead Halide Perovskites (LHPs), with lead (Pb) being an element with a high atomic number (Z) [36, 37]. Compared to conventional scintillator materials, LHPs offer additional benefits such as defect tolerance, long carrier diffusion length, long charge carrier lifetime, and a tunable, relatively narrow band gap. The performance of a scintillator material is quantified by its light yield, which is a measure of the number of emitted photons per unit energy deposited. The light yield of CsI:Tl is 60,000 photons/MeV [33] and LuI3:Ce3+ is 100,000 photons/MeV [38] . Literature studies report, a light yield >6000 photons/MeV for two dimensional (2D) LHPs [39] and >100,000 photons/MeV for doped three-dimensional (3D) LHPs [40]. The difference between 2D and 3D perovskites will be explained in the next section. It is important to note that, the light yield achieved with doped LHPs is on par with conventional scintillator materials. However, more studies are needed to address the challenges associated with scaling these materials and developing less toxic elements for commercial use.

1.3 Structural Varieties of Metal Halide Perovskites

The perovskite structure is named after the mineral calcium titanate ($CaTiO_3$), which exhibits a distinctive crystalline structure characterized by corner-shared TiO_6 octahedra extending along all three dimensions [41]. This structural feature later became the defining characteristic of a broader class of materials known as perovskites. A perovskite structure generally has the chemical formula ABX_3. Metal Halide Perovskites (MHPs) are a specific class of perovskites, where A is typically a monovalent cation (such as cesium, methylammonium, or formamidinium), B is a divalent metal cation (commonly lead or tin), and X is a halide anion (chlorine, bromine, or iodine) [42–44]. The structure of a typical MHP that crystallizes in a cubic structure is shown in Fig. 1.2 [44]. The compound $CsPbBr_3$ has a Pm-3m space group, with Cs, the A-site cation, occupying the body center of the cube, Pb, the B-site cation, at the corners of the cube and center of the octahedra, and bromine (Br), the X-site anion, at the corners of the octahedra. Typically, the valence band maximum and conduction band minimum in these materials originate from the inorganic octahedral layer. As the octahedra extend in all three dimensions, these materials are referred to as 3D MHPs, due to its conduction along all three dimensions [45–47].

In the previous example of MHP crystal structure, an inorganic atom occupied the A-site. When the A-site is occupied by an organic molecule they are classified as Hybrid Organic-Inorganic Perovskites (HOIPs) [47]. A typical example of an orthorhombic 3D HOIP is $MAPbBr_3$ ($MA=CH_3NH_3$) (Fig. 1.3) [48]. In this structure, Pb and Br form the octahedral layer, with Pb occupying the corners of the orthorhombic structure and the center of the octahedra, while Br occupies the corners of the octahedra. The MA organic molecule occupies the A-site.

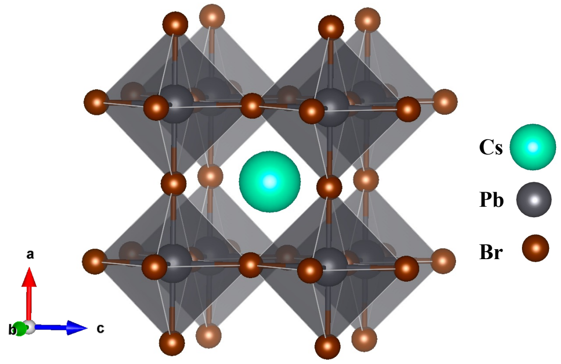

Figure 1.2: Crystal strcuture of $CsPbBr_3$ (Pm-3m), generated using the software VESTA [49] based on the crystallographic information file (CIF) obtained from [44]

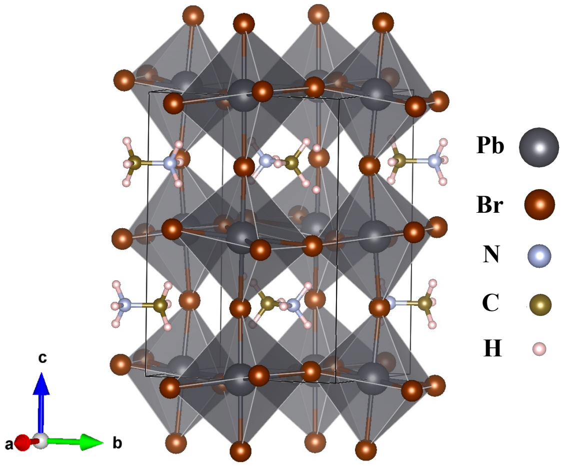

Figure 1.3: Crystal strcuture of $MAPbBr_3$ (Pnma), generated using the software VESTA [49] based on the crystallographic information file (CIF) obtained from [44]

Two-dimensional (2D) layered HOIPs represent another distinct class of MHPs. In 2D HOIPs, the inorganic framework that extends in three dimensions in 3D HOIPs is confined to two-dimensional planes, which are separated by layers of organic molecules [50–52]. These materials generally follow the chemical formula $(A)_{n-1}B_nX_{3n+1}$, where

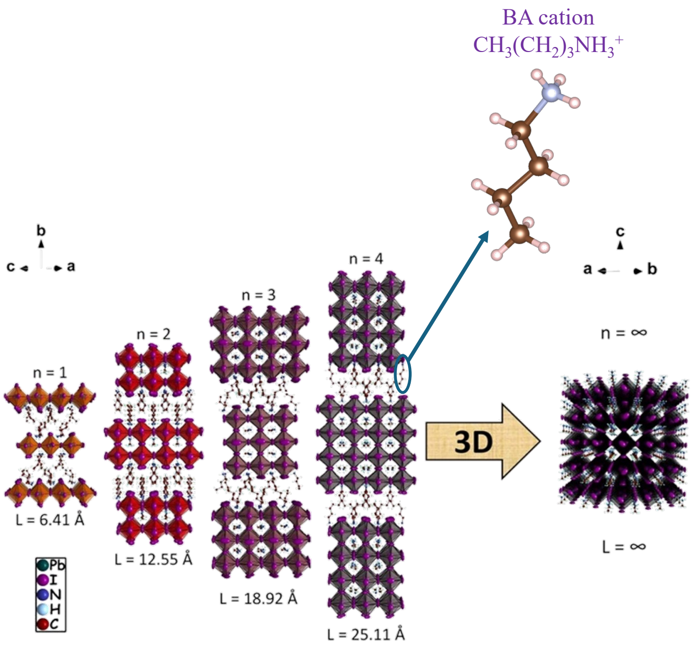

Figure 1.4: Crystal structure of 2D HOIPs of general formula $(A)_{n-1}B_nX_{3n+1}$, $(n = 1, 2, 3, 4, \infty)$ [50].

n is the number of inorganic layers separating each organic layer $(n = 1, 2, 3, 4, \ldots, \infty)$. As n approaches infinity $(n \to \infty)$, the structure of 2D HOIPs converges to that of 3D HOIPs. Figure 1.4 illustrates schematics of 2D HOIPs with increasing values of n [50]. Similar to 3D HOIPs, electrical conduction in 2D HOIPs is confined to the inorganic octahedral layers. Due to the layered structure, there is no conduction perpendicular to the inorganic planes, as the organic layers typically do not contribute to the conduction or valence bands. This restriction of conduction to the inorganic 2D planes is the reason they are referred to as 2D HOIPs.

1.4 Structural Dynamics in Metal Halide Perovskites

Metal Halide Perovskites (MHPs) have emerged as promising semiconductor materials for luminescent and energy applications. Unlike conventional semiconductors used in these applications, such as Si, CdTe, and GaAs, MHPs possess low elastic constants and low-energy phonon modes at room temperature, which makes them more prone to dynamic lattice disorder [53–55]. Due to this, to tune the optoelectronic properties of MHPs for better performance, it is necessary to understand the microscopic details of various structural dynamics.

When semiconductor materials absorb photons with energies comparable to their bandgap, they generate excitons, which are quasiparticles formed by bound electron-hole pairs with notable binding energies (often tens to hundreds of meV) [56, 57]. In photovoltaic materials, excitons are typically separated into free electrons and holes at p-n junctions, contributing to electrical conduction [58–60]. The energy required to separate an exciton into a free electron and a free hole is called the exciton binding energy (EBE) [53]. In MHPs, the interplay of structural distortions, molecular rotations, librations, and phonon dynamics creates a complex environment that makes it challenging to quantify EBE accurately [61–63]. This is evident from the significant spread of EBE values reported for the same material by different studies [64–67]. For example, an EBE of 511 meV and 349 meV was reported for $(PEA)_2PbBr_4$ (phenethylammonium lead bromide) by two different studies [64, 65]. The accurate determination of EBE is necessary for practical applications.

The optoelectronic performance of a material is affected when photo-excited excitons or free charge carriers lose energy to heat through scattering from defects and phonons [68, 69]. For LEDs, a high EBE is preferred because stable excitons at room temperature increase the likelihood of radiative recombination, where electrons and holes recombine to emit photons, which is essential for light emission [35, 64]. In contrast, when excitons dissociate into free charge carriers, they are more susceptible to phonon scattering, leading to energy loss via non-radiative recombination mechanisms, where the energy is dissipated as heat rather than light. This difference contributes to the greater success of 2D HOIPs as LEDs compared to 3D HOIPs.

2D HOIPs can be described as self-assembled quantum well structures, where the organic cation layer acts as a potential ‘wall,’ and the inorganic layer, consisting of metal cations and halide anions, functions as a potential ‘well’ [50–52]. Due to quantum confinement, excitons are confined to move only within the 2D plane of the inorganic layer, reducing the spatial separation between electron-hole pairs compared to 3D HOIPs. This results in a stronger Coulomb interaction in the 2D HOIP excitons, thereby enhancing the EBE [8, 70]. A higher EBE increases the light yield in LEDs. For example, a light yield of less than 1000 photons/MeV was observed for the 3D HOIP, $MAPbBr_3$, while 9000 photons/MeV was observed for the 2D HOIP, $(EDBE)PbCl_4$ (EDBE = (2,2’-ethylenedioxy)-bis(ethylamine)) [70, 71] at room temperature. However, recent studies have shown significant improvements in the light yield of doped 3D MHPs, such as in Yb-doped $CsPbCl_3$ and PbS quantum dot-embedded $MAPbBr_3$, where light yields have exceeded 30,000 photons/MeV [35, 40].

For PV devices, a low EBE is beneficial because it facilitates the separation of electron-hole pairs into free charge carriers, which can then be collected at the electrodes [64, 72]. High EBEs in PV devices would hinder efficient charge separation, leading to recombination before the carriers reach the p-n junction, thereby reducing overall efficiency. In PV devices, free charge carriers can also be affected by phonon scattering, which leads to energy losses [68, 69]. Owing to this, an MHP with both low EBE and minimal phonon scattering is ideal for PV applications

Stability is another important parameter affecting the performance of MHPs, as they tend to degrade quickly under ambient conditions. 2D HOIPs are generally more stable compared to 3D HOIPs due to the hydrophobic organic layer, which makes them more resistant to moisture [73]. However, the band gap of 2D HOIPs is typically higher compared to 3D HOIPs, which can reduce their efficiency. Studies have suggested that using perovskites with distorted octahedra can improve stability [74]. For instance, cubic $CsPbI_3$ is not thermodynamically favorable and tends to transit to less efficient distorted orthorhombic phase under ambient conditions; however, by adjusting the synthesis method, researchers were able to produce a more stable distorted orthorhombic $CsPbI_3$ that demonstrated an enhanced efficiency from 11.4% to 15.06% [75]. This approach resulted in a more promising material for PV applications.

Both 3D and 2D hybrid organic-inorganic perovskites (HOIPs) often undergo inorganic layer distortion due to the reorientation of organic molecules [76–78]. Studies on $(BA)_2PbI_4$ have shown an increased bandgap and reduced bandwidth when the system underwent higher octahedral tilting [76]. Thus a wide variety of properties, including enhanced stability, optimized band gap, and exciton binding energy (EBE), can be realized by tuning the chemical structure of MHPs [79–81].

Photoexcited charge carriers with higher lifetimes are required for the overall efficiency of PV and LED devices. A longer charge carrier lifetime means that the carrier energy is not lost as heat through non-radiative recombination mechanisms. For three-dimensional (3D) HOIPs, experimental evidence suggests that the reorientation of organic molecules aids in polaron formation [82–85]. Polarons, quasiparticles formed by the Coulomb interaction between an excess charge (an electron or a hole) and the molecule [86], screen or protect the carriers from defects, impurities, and phonon scattering, thereby prolonging their lifetime [69]. Conversely, pure inorganic MHPs, despite lacking organic molecules, have also demonstrated moderate photovoltaic performance [75, 87], highlighting the significant role of the inorganic perovskite framework vibrations through their interactions with charge carriers. Generally, there are two scenarios for phonon-mediated polaron formation: (1) Polaron formation facilitated by optical phonons [62, 82]. Free charge carriers interact with polarized optical phonons via Coulomb interaction, enhancing the screening effects and thus extending their lifetime. (2) Melting of acoustic phonons [88–90]. Most of the excess energy of photoexcited charge carriers is dissipated via scattering from acoustic phonons. Upon heating, acoustic phonons in the sample could melt, which can reduce the charge carriers scattering from phonons and result in a long charge carrier lifetime. Thus, investigations into both the rotation of organic molecules and lattice vibrations are necessary to determine the charge carrier lifetime and overall efficiency of these materials in optoelectronic devices.

Various techniques can be used to probe the tunable dynamic physical and structural properties of MHPs discussed above. Structural characterization to quantify distortions can be performed using X-ray diffraction and its refinement [91, 92]. Neutron, X-ray, and Raman scattering are commonly used tools to understand the details of phonon and rotational dynamics [61, 93–95]. Additionally, neutron and X-ray scattering can provide insights into the size and shape of domains and the distribution of dopants within the systems [96, 97]. All these methods are complementary, and their advantages and disadvantages will be discussed in the later sections. Optoelectronic properties such as luminescent mechanisms, band gap, excitonic emission, and recombination mechanisms can be understood using photoluminescence and radioluminescence measurements. A combination of these tools can provide insights into how certain structural dynamics impact the optoelectronic properties of these systems. Accordingly, the upcoming sections are divided into four chapters: Chapter 2 will focus on the various experimental techniques used relevant to our research goals. Chapter 3 will discuss the contribution of rotational and phonon dynamics to the optoelectronic properties of 2D HOIPs. Chapter 4 will focus on quantum dot-embedded MHP scintillators and the quantification of the spatial distribution of quantum dots within them. Chapter 5 will explore the structural dynamics along different unit cell directions in single crystals of a specific 3D HOIP. The final chapter will focus on the general conclusions, future directions and how we contributed to the research efforts in the field of MHPs.

1.5 Summary

In this chapter, we focused on understadning why MHPs are promising materials for optoelectronic device applications, along with their advantages and disadvantages compared to conventional semiconductors. We examined their crystal structure and the highly tunable dynamic structural and physical properties. Understanding these microscopic details is important to optimize the optoelectronic properties of MHPs for efficient device preformance.

Chapter 2

Methods

In this chapter, we will discuss inelastic, quasi-elastic, and small-angle neutron scattering, Raman scattering, and X-Ray Diffuse Scattering techniques, along with photoluminescence and radioluminescence in the context of optoelectronic measurements. We will highlight how these techniques can be complimetary to each other. These techniques were selected for their advantages in probing specific structural dynamics where the other techinique can be disadvantageous. All these techniques provided relevant informations for our specific research objectives.

2.1 Scattering Techniques

2.1.1 Inelastic and Quasi-Elastic Neutron Scattering

The optoelectronic properties of 3D/2D hybrid organic-inorganic perovskites are influenced by both phonon dynamics and rotational dynamics from the inorganic and organic components. The typical wavelength used in X-ray scattering does not probe lighter atoms, such as hydrogen, carbon, and nitrogen, effectively, as X-rays interact primarily based on atomic charge density. Hence, stronger scattering is observed for elements with higher atomic numbers. Neutrons, on the other hand, are not charged and, therefore, do not encounter a Coulomb barrier. They can penetrate deeply into the nucleus and are scattered by nuclear forces. Thus neutrons are an effective tool for probing dynamics involving lighter atoms such as hydrogen, nitrogen, carbon, etc [98].

Neutron energies can vary across a wide range: cold neutrons have energies typically between 1-10 meV (millielectronvolt) and are useful for probing large structures or slow dynamics, thermal neutrons have energies in the range of 10-100 meV (corresponding to room temperature) and are well-suited for studying atomic vibrations, while hot neutrons have energies above 100 meV, ideal for investigating faster dynamics or higher energy excitations. While these energy definitions are fairly standard, the exact energy cutoffs (e.g., the distinction between cold and thermal or thermal and hot) may vary slightly depending on the neutron source, experimental setup, or specific research focus. For our purposes, we mainly focused on neutrons with energies around 3 meV to probe the slow dynamics like rotation of organic molecules and neutrons with energies in the range 7 meV to 712 meV to probe the low and high energy phonons specific to different systems [99].

For an inelastic neutron scattering experiment, the incident neutron beam interacts with the atoms in the target sample and scatters. The energy and direction of the scattered neutrons are measured using detectors. Since neutrons have no electrical charge, they cannot directly produce ionization in a detector. Instead, neutron detectors rely on a conversion process where the incident neutron interacts with a nucleus to produce a secondary charged particle. He-3 detectors work based on this principle, where secondary charged particles are produced when the He-3 atom absorbs a neutron. These secondary charged particles are then detected later through their ionization of gas within the detector. The ionization creates an electrical signal, which is further amplified and recorded. Another form of detector is a scintillator, where the absorbed neutron causes the emission of photons within the scintillator material, which is then detected by photomultiplier tubes or photodiodes that convert the light into an electrical signal [100].

Based on the information from these detectors, we obtain the number of scattered neutrons (counts) in a given direction as a function of energy. If the direction of the scattered neutrons is θ and ϕ, the differential cross-section is given by:

$$\frac{d^2\sigma}{d\Omega dE'} = \frac{\mathrm{n}}{\Phi d\Omega dE'} \tag{2.1.1}$$

where n is the number of scattered neutrons per second into a solid angle $d\Omega$ in the direction θ, ϕ, with final energy between E' and $E' + dE'$. The momentum transfer from the neutron to the sample is defined as $Q = k - k'$ where k and k' are the wave vectors of the incident and scattered neutron, respectively. The amount of energy the sample gained from neutron is $\hbar\omega = \frac{\hbar^2}{2m}\left(k^2 - k'^2\right)$ where m is the mass of the neutron [98].

There are two types of measurement mechanisms in neutron scattering: constant wavelength and time-of-flight. In the constant wavelength technique, the incident neutron beam has a fixed wavelength selected by a monochromator, covering a specific Q range. In contrast, in time-of-flight measurements, a polychromatic beam is incident, and the scattered pulse is analyzed based on the time it takes to reach the detector. This method allows a broad range of Q values within the incident pulse to be analyzed simultaneously. Time-of-flight is particularly useful when the exact Q range of interest is not known beforehand. For our purposes, we use time-of-flight measurements. [101].

The intensity of nuclear scattering is proportional to the spatial correlation function of nuclei [98].

$$\frac{d^2\sigma}{d\Omega d\omega} = \frac{k'}{k}\frac{1}{2\pi\hbar}\sum_{jj'}\overline{b_j b_{j'}}\int_{-\infty}^{\infty}\langle\exp\left(-i\boldsymbol{Q}\cdot\boldsymbol{R}_j(0)\right)\exp\left(i\boldsymbol{Q}\cdot\boldsymbol{R}_{j'}(t)\right)\rangle\exp(-i\omega t)dt \tag{2.1.2}$$

where b_j is the scattering length for the nuclei j. The total nuclear scattering length b of an atom depends on the isotope and the spin state of the nucleus. In disordered or mixed isotope systems, the scattering lengths can vary randomly for different nuclei. We assume that there is no correlation between the scattering lengths of two different nuclei. Owing to this, the cross terms in the scattering equations that depend on correlations between these values are cancelled out. This assumption simplifies the analysis by treating each nucleus's scattering as an independent event. Based on this, we have:

$$\begin{aligned}\overline{b_j b_{j'}} &= (\bar{b})^2, \quad j' \neq j\\ \overline{b_j b_{j'}} &= \overline{b^2}, \qquad j' = j\end{aligned} \tag{2.1.3}$$

As a result, the differential cross section simplifies to:

$$\begin{aligned}\frac{d^2\sigma}{d\Omega d\omega} &= \frac{k'}{k}\frac{1}{2\pi\hbar}(\bar{b})^2\sum_{jj'}\int\langle j', j\rangle\exp(-i\omega t)\,dt\\ &+\frac{k'}{k}\frac{1}{2\pi\hbar}\left\{\overline{b^2}-(\bar{b})^2\right\}\sum_{j}\int\langle j, j\rangle\exp(-i\omega t)\,dt\end{aligned} \tag{2.1.4}$$

where

$$\langle j', j\rangle = \langle\exp\left(-i\boldsymbol{Q}\cdot\boldsymbol{R}_j(0)\right)\exp\left(i\boldsymbol{Q}\cdot\boldsymbol{R}_{j'}(t)\right)\rangle\,.$$

.

The first term in Eq. 2.1.4 represents coherent scattering, which occurs when the scattering amplitudes from different nuclei interfere constructively or destructively. Coherent scattering provides information about the long range ordering in the crystal lattice. It reflects how the position of an atom at time t1 is correlated with its position at time t2, as well as with the position of a different atom at time t2. The second term represents incoherent scattering, which results from random variations in the scattering lengths between nuclei. Incoherent scattering does not provide structural information but instead gives details about individual atomic dynamics. It only reveals how the position of an atom at t1 is correlated with its position at t2 without providing information about the positions of other atoms at different times.

Phonon dynamics are observed in neutron scattering as inelastic coherent scattering. In contrast, the rotational dynamics of molecules are typically seen as incoherent scattering. A phonon vibration with a relaxation time τ has a scattering intensity that is proportional to $\exp\left(-\frac{t}{\tau}\right)$ and manifests as a Lorentzian profile centered at its normal mode after Fourier transforming from the time domain to the energy domain. We will need to perform DFT calculations to quantify which atoms in the system contribute to these phonon modes. For the rotation of an organic molecule with a relaxation time τ, the intensity is also proportional to $\exp\left(-\frac{t}{\tau}\right)$, resulting in a Lorentzian profile centered at the elastic channel ($\hbar\omega = 0$) after Fourier transforming from the time domain to the energy domain. Typically, the peaks from phonon dynamics are much sharper and narrower in energy than those of atomic rotations. This difference arises because phonons involve long-range correlated interactions that decay slowly over time, resulting in sharper Lorentzian peaks in the energy domain. Molecular rotations generally involve larger-scale movements than phonons and hence occur on longer time scales. However, in contrast to phonons, rotations are short-range as they are not correlated with surrounding atoms. Thus, rotations have faster energy dissipation or decay over time, producing broader Lorentzian signals in the energy domain. Considering the instrument resolution function to be Gaussian, the phonon intensities at different energies and the rotational intensity at $\hbar\omega = 0$ can be analyzed using a Voigt fit, which is a convolution of a Gaussian (instrument resolution) and a Lorentzian function (effects from the sample).

Additionally, when there is no energy transfer between the incident neutron and the target sample, the coherent scattering is elastic. The differential cross-section, in this case, is given by

$$\left(\frac{d\sigma}{d\Omega}\right)_{\text{coh,el}} = \frac{N(2\pi)^3}{v_0}\sum_{\tau}\delta(\boldsymbol{Q}-\boldsymbol{\tau})\left|F_N(\boldsymbol{Q})\right|^2 \tag{2.1.5}$$

where v_0 is the unit cell volume, $\boldsymbol{\tau}$ is the reciprocal lattice vector for a certain nuclear Bragg peak, and

$$F_N(\boldsymbol{Q}) = \sum_d \overline{b_d}\exp(i\boldsymbol{Q}\cdot\boldsymbol{d})\exp(-W)$$

is the nuclear structure factor. Here, $\boldsymbol{d}$ is the position of a certain atom in the unit cell, and $\exp(-W)$ accounts for averaged atomic displacements, with $W = \langle(\boldsymbol{Q}\cdot\boldsymbol{u})^2\rangle$. Neutron elastic coherent scattering, in other words, neutron diffraction, provides information about the crystal structure of a material, similar to X-ray diffraction. Since energy changes are not measured in diffraction, the temporal or time-dependent behavior of a system is lost. For our projects, the main focus was to understand phonon and rotational dynamics. We employed inelastic neutron scattering to investigate the phonon dynamics. The typical energy of phonon modes in MHPs varies from low-energy phonons around 1.5 meV to higher-energy phonons < 500 meV. Interactions due to incoherent scattering, such as atomic rotations, ion diffusions, and reorientations, involve very low energy transfers, typically below 2 meV [102]. Therefore, we utilize quasi-elastic neutron scattering to study these processes, as it probes regions of low energy transfers with minimal excitations of the low-energy phonons.

2.1.2 Small Angle Neutron Scattering

Small-Angle Neutron Scattering (SANS) is designed to probe large-scale structural features of a system, typically larger than interatomic distances. In contrast to inelastic neutron scattering, where the typical incident neutron wavelength ranges from 1.5 to 2 Å to match interatomic distances, SANS utilizes an incident wavelength typically between 4 and 20 Å [103]. For inelastic or quasi-elastic neutron scattering, the scattered neutron intensity, $S(Q, \hbar\omega)$, is measured as a function of energy transfer and the scattered solid angle. In contrast, SANS measures scattered intensity S(Q) solely as a function of scattered solid angle which is called the static scattering. During static scattering, the detector collects neutrons at a given solid angle for all different energies, making energy transfer irrelevant and resulting in the loss of energy information. This approach differs from purely elastic scattering, where $\hbar\omega = 0$. In many cases, elastic and quasi-elastic scattering dominates for static scattering, making elastic scattering a good approximation for the same (Eq. 2.1.5) [104].

For SANS, using the elastic scattering approximation, the scattering vector Q is given by:

$$Q = \frac{4\pi}{\lambda} \sin\left(\frac{\theta}{2}\right), \tag{2.1.6}$$

where θ and λ are the scattering angle and wavelength, respectively. To achieve small angles, and thus probe very low Q values and large real-space distances, the sample-to-detector distances must typically be larger than those used in inelastic neutron scattering. This distance can range from 1 m to 20 m. The 1 m to 5 m range typically covers a Q-range similar to that of inelastic neutron scattering, but beyond 10 m, the focus shifts to the region where $0.001\,\text{Å}^{-1} < Q < 0.01\,\text{Å}^{-1}$. At such large distances and small angles, the real-space distance d from Q can be approximated by $Q \sim \frac{1}{d}$ [105].

A wide variety of modeling functions have been reported for SANS, depending on the state of the system (solid, liquid), the shapes of particles (spherical, cylindrical, micellar), and the types of scatterers present. The differences in the types of scatterers: some of which dominate at a particular Q range while others dominate at different Q ranges can lead to observable changes in the slope of S(Q). The Q value at which the S(Q) dependence change is generally referred to as the crossover region. This crossover region can be identified using various functions, ranging from linear and quadratic forms to power laws, Gaussian, Lorentzian, and other scatterer shape-incorporated functions. The choice of model depends on the type of signals obtained during a SANS measurement and the assumptions made based on initial knowledge about the sample, which may come from crystal structure analysis, surface morphology analysis, or existing literature [104].

With the higher resolution at small-angle scattering enabled by a large sample-to-detector distance, large incident wavelength to probe features larger than interatomic distances, and various analysis models, SANS is an ideal tool to characterize complex materials and understand their structural properties over a broad range of length scales.

2.1.3 Raman Scattering

Raman scattering is the inelastic scattering of photons when light interacts with a crystal [106–108]. When a photon of incident momentum k_i and incident energy E_i interacts with a crystal, it gets scattered with an energy E_f and momentum k_f. It is important to note that typically, for Raman scattering, the incident photon and scattered photon have wavelengths much larger than the interatomic distances. Thus, unlike inelastic X-ray or neutron scattering, where the scattering potential depends on the atomic charge density and nuclear density, for Raman, the scattering potential depends upon the polarizability of the scatterer. When an electromagnetic wave interacts with the scatterers, it could temporarily distort the electron cloud around the atoms, inducing polarization. Additionally, phonons or lattice vibrations change the distance between atoms, which could alter their polarizability. In Raman scattering, when the incident light interacts with atoms, if the polarizability changes during the atomic vibrations, the scattered light will have a different energy than the incident light, leading to a shift in frequency (Raman shift). This shift gives us information about the phonons. Change in polarizability is necessary for the Raman shift. Due to this selection rule, not all atomic vibrations are active in Raman scattering. Though polarizability is influenced by the local electronic environment around atoms, Raman scattering measures the collective polarizability changes, making it more of a bulk property.

Due to the much longer wavelength of visible light used in Raman spectroscopy, it is insensitive to the detailed atomic positions within the lattice. Additionally, the available momentum transfer Q is much smaller than the momentum of many phonons. Hence, $|Q|$ is essentially zero in Raman scattering, while scattering along different Q can be measured in neutron/X-ray scattering [106].

Generally, group theory calculations are used to interpret Raman data. Based on the character table of a molecule, we can identify the irreducible representations contributing to active Raman modes. Density functional theory (DFT) calculations are often employed for complex systems to predict and confirm these modes. Our study used Raman scattering as a complementary technique to neutron scattering to understand the phonon dynamics. Although Raman scattering does not capture all phonon modes, the scattering intensity tends to be more sharply resolved, as we observe only modes with$|Q|$=0 momentum transfer. This reduces the overlap and difficulty in resolving phonon peaks from various Q values typically encountered in neutron scattering.

Additionally, in neutron scattering, the Debye-Waller factor e^{-2W}, where W depends on atomic displacements, tends to suppress and broaden the inelastic coherent scattering intensity upon warming due to large atomic displacements. However, since Raman scattering is insensitive to atomic-scale details due to the long incident wavelength, as mentioned before, its intensities are not significantly affected by temperature-dependent atomic displacements. Thus, for our studies, we used Raman scattering as a complimentary technique to get a clearer picture of the high-temperature phonon modes.

2.1.4 X-Ray Diffuse Scattering

X-ray diffuse Scattering (XDS) is a technique used to investigate deviations from perfectly ordered crystals, such as short-range interactions like charge density waves, defects, thermal vibrations, and other types of disorder [109]. The incident beam undergoes Bragg scattering during X-ray or neutron diffraction, resulting in sharp diffraction peaks. Diffraction peaks originate from the long-range order of the crystal lattice, thus providing information about the crystal structure. When a material is amorphous and lacks an extended range of periodic atomic arrangements, the scattered pattern will be more diffuse, which could appear as continuous streaks or scattering rods. It is important to note that defects or phonon overdamping in a perfectly crystalline system can pose local disorders [110], which can also appear as diffuse signals away from the Bragg peaks in scattering. The intensity of this diffuse signal varies depending on the type and degree of disorder. Generally, the intensity of the diffuse scattering is significantly weaker than that of the Bragg peaks. Therefore, diffuse scattering offers a way to resolve these weak diffuse intensities with the help of a more intense and focused incident beam, often provided by synchrotron sources [111].

Phonons manifest as diffuse intensity along various directions in the crystal. If the phonons tend to overdamp with increasing temperature, this results in broader diffuse signals, indicating a more significant lattice disorder [112]. Due to hydrogen's strong incoherent scattering background in neutron experiments, observing clear phonon features might require deuterating the samples or using inelastic X-ray scattering (IXS) [98]. However, IXS can cause radiation damage, especially in structurally dynamic materials like MHPs, because the energy transfer from the incident X-rays to the sample during phonon excitation can ionize the material and lead to structural degradation. In contrast, XDS is an elastic process with quasi-elastic or no energy transfer, protecting the sample from ionizing radiation. Thus, XDS does not provide direct information about the normal modes of phonons but allows us to observe phonon-related diffuse intensity along different crystallographic directions in the reciprocal space (Q). As the scattered intensity is time-averaged, temporal coherence is lost, and we cannot track the atomic motion in a specific time sequence [29, 113]. Inelastic measurements are required to achieve this, where energy transfer is measured, providing information about nuclear positions and lifetimes during phonon vibrations.

There are various models to quantify the diffuse scattering. As the phonons decay exponentially considering spatial correlations, the diffuse rods associated are fit using a Lorentzian function by the Ornstein-Zernike (OZ) theory [114].

$$S(Q) = \frac{A}{\left(\frac{Q-Q_0}{\gamma}\right)^2 + 1} \tag{2.1.7}$$

where A is the scaling constant, γ is the half width half maximum (HWHM), $\xi = \frac{1}{\gamma}$ is the correlation length and Q the momentum transfer. In the context of phonon-induced diffuse scattering, the OZ equation can be adapted to describe the correlation between displacements of atoms caused by phonons.

2.2 Optoelectronic Characterization

2.2.1 Photoluminescence Measurements

Photoluminescence (PL) measurement is a technique used to understand the luminescence response of a material. PL measurements are widely used to characterize the optoelectronic properties of light-emitting and solar-cell device materials and thus to ensure their quality [76,115]. During a PL measurement, a light source in the infrared, visible, or UV range is incident on the material, exciting electrons. As the excited electrons undergo radiative recombination, they emit light, which is then detected using optical sensors such as photomultiplier tubes or photodiodes. The difference in energy of the absorbed and emitted photons is known as the Stokes shift, and it provides essential information about the electronic and vibrational states of the material [116].

The presence of defects, impurities, and phonons can influence the PL efficiency of a material and how well the material can absorb and emit light [117]. Complex materials like MHPs, which are known for their electron-phonon coupling, can affect the relaxation pathways of excited electrons, thus improving or quenching the emitted intensity [115]. The PL spectrum along the photon's wavelength typically shows a sharp peak corresponding to the optical band gap. When electrons undergo phonon scattering and lose energy in the form of non-radiative recombination, the number of electrons undergoing radiative recombination decreases, thus suppressing the PL intensity. Additionally, phonon scattering can broaden or shift the dominant emission peak (optical band gap) [76, 88]. Thus, PL measurements are an alternative way to study the influence of phonons. Since we aim to identify how lattice or rotational dynamics affects the material efficiency in PV or LED devices, PL measurements are a crucial tool to determine how phonons or rotations observed from scattering techniques affect their optoelectronic properties.

2.2.2 Radioluminescence Measurements

Radioluminescence (RL) is also a technique used to understand the luminescence response of a material. Unlike PL measurements, where incident radiation is in the UV, Visible, or infrared region, in RL measurements, ionizing radiations like X-ray, alpha, or beta particles are used [118]. Typically, the emission from RL is broader in wavelength because the absorbed radiation causes a broader range of excitation due to its high energy. In comparison, PL has a much narrower emission as the optical band gap of the material is primarily excited. RL techniques are used in various applications, including radiation detection, scintillation counting, and lighting technologies, etc. During a radioluminescence measurement, ionizing radiation is incident on the material, which excites the electrons and leads to light emission as the excited electrons return to their ground state. A sensitive optical sensor, typically a photomultiplier tube or a photodiode, detects this emitted light, converts it into an electrical signal, and measures the overall light intensity as counts (individual light pulses) [119]. The counts of emitted photons accumulated over a specific period reflect the material's overall luminescence response. [35, 40].

The efficiency of RL depends on factors such as the type of ionizing radiation, the material's crystal structure, and impurities or defects. As mentioned in Chapter 1, scintillators are efficient emitters of multiple low-energy photons after the absorption of high-energy photons, and hence a higher RL intensity is generally expected. Therefore, for our study on quantum dot (QD)-loaded MHPs as potential scintillator material, RL measurements will be an important tool for understanding how the optoelectronic properties change with different QD loadings.

Chapter 3

Vibrational and Rotational dynamics of 2D HOIPs

Two-dimensional (2D) HOIPs have achieved notable success in light-emitting applications, due to their strong excitonic effects, tunable bandgaps, and enhanced environmental stability compared to their 3D counterparts [120–124]. However, the underlying microscopic mechanisms that contribute to their photoluminescence efficiency, including exciton dynamics and charge transport, have not been comprehensively studied. The impacts of inorganic layers are often emphasized, while the roles of polarized molecules appear to be underexplored and underestimated.

Previous studies [125] on these soft lattice perovskites showed that the valence band maximum (VBM) is determined by the halide p-orbital hybridized with metal s-orbital and the conduction band minimum (CBM) is mainly contributed from metal p-orbitals, which reflects the fact that the inorganic framework plays a leading role in the electronic band structure construction and hence optoelectronic properties. For example, Gong and his colleagues [115] reported that the Photoluminescence Quantum Yield (PLQY), defined as the ratio of emitted to absorbed photons, of 2D HOIPs could be influenced by electron-phonon interactions with different crystal rigidity levels. They characterized the role of crystal rigidity in two 2D HOIPs, $(BA)_2PbBr_4$ and $(PEA)_2PbBr_4$ by comparing atomic displacements, spin-lattice relaxation, and time-variation in the electronic band structure. They proposed lower crystal rigidity and a much stronger electron-phonon interaction in $(BA)_2PbBr_4$ to account for its pronounced drop of PLQY at room temperature. Nevertheless, the general crystal rigidity cannot well explain their temperature-dependent measurements of PLQY (Fig. S9(a) in Ref. [115]) – Below 150 K, both materials persist a high-level PLQY ($> 90\%$); upon further heating up to room temperature, the PLQY of $(BA)_2PbBr_4$ dramatically drops down to 17% while that of $(BA)_2PbBr_4$ remains above 70%. The intriguing behavior of PLQY indicates the activation of some hidden mechanism around 150 K in $(BA)_2PbBr_4$, which our work proposed to be a rotational motion of the polarized organic molecule. In any case, a detailed comparative study among lattice dynamics, molecular rotational dynamics, and photoluminescence performance is essential to complete the big picture of 2D HOIP optoelectronics.

In this work, we focus on two iodine counterparts, $(BA)_2PbBr_4$ and $(PEA)_2PbBr_4$, which would have similar optoelectronic properties with the corresponding bromides [126]. We have used temperature-dependent X-ray diffraction to characterize their crystal structures and octahedral distortions, which could be closely related to variations in electronic band structure. We used Quasi-Elastic Neutron Scattering (QENS) to directly probe the rotational motion of hydrogen-contained molecules as a function of temperature, from which we have quantitatively identified the rotational modes of different rotors in these two materials with the help of group theory and Jump model analysis [127]. Moreover, temperature-dependent Inelastic Neutron Scattering (INS) and Raman scattering measurements were conducted to systematically analyze relevant lattice vibrations (i.e., phonons). All these results were compared with the temperature-dependent evolution of photoluminescence performance. Based on our comparison, we suggest that in these two 2D HOIPs, increasing temperature activates and enhances the rotational motion of polarized organic molecules, which inversely correlates with the temperature-dependent variation of PLQY, while lattice vibrations do not exhibit a clear relationship. We thus proposed a scenario that the rotational motion of polarized organic molecules works as dynamical perturbations to the inorganic framework which fundamentally dominates the construction of electronic band structure. These perturbations interfere with the dielectric environment surrounding confined excitons, potentially reducing the exciton binding energy or breaking binding energy degeneracy, enhancing the non-radiative decay of charge carriers, and thereby suppressing the PLQY [126].

3.1 Experimental Details

Powder samples of $(BA)_2PbI_4$ and $(PEA)_2PbI_4$ were used for all the measurements. The sample synthesis was performed at the Department of Chemical Engineering, University of Virginia, through collaboration, (synthesis details provided in Appendix A). Powder X-ray diffraction (XRD) from 80 K to 300 K was performed at the University of Virginia on a Bruker D8 VENTURE dual-wavelength Mo/Cu Kappa four-circle diffractometer equipped with an Oxford Cryostream 800 low-temperature device. The 2-D XRD measurements were collected as a series of correlated phi scans which were integrated using the XRD Eval plugin within the Bruker APEX5 [128] software suite at the University of Virginia. Quasi-elastic neutron scattering (QENS) measurements were conducted on the cold neutron disk chopper spectrometer, AMATERAS [129], at the Japan Proton Accelerator Research Complex (J-PARC), with incident energies E_i=3.3 meV and 8 meV, and an energy resolution of approximately 1% of E_i. Inelastic neutron scattering data were collected on the 4D Space Access Neutron Spectrometer (4SEASONS) [130,131], also at J-PARC. A series of incident neutron energies (E_i=10, 30, 62, 115, 280, and 712 meV) were selected to cover the entire phonon spectrum upon heating from 8 K to 300 K, with an energy resolution of about 5% of E_i. Raman scattering and photoluminescence measurements were performed at the Center for Condensed Matter Sciences, National Taiwan University. To gain further insights into lattice vibrations, density-functional theory (DFT) calculations were carried out using the Vienna Ab-initio Simulation Package (VASP) [132], employing the projected augmented wave method [133] and the Perdew-Burke-Ernzerhof exchange-correlation potential [134]. A plane-wave basis set with a 400 eV cut-off energy was used for the calculations.

3.2 Results and Analysis

3.2.1 X-Ray Diffraction

The structures of 1-layer lead iodide perovskite $(BA)_2PbI_4$ and $(PEA)_2PbI_4$ are shown in Figure 3.1. These structures were obtained by refining the X-ray Diffraction (XRD) patterns at 300 K (Fig.3.2). In both structures, the inorganic Pb-I layers are intercalated with bulky organic molecules. In $(BA)_2PbI_4$, the BA molecule is a long alkyl chain $CH_3CH_2CH_2CH_2NH_3$, whereas for $(PEA)_2PbI_4$, the PEA molecule has a toluene ($C_6H_5CH_2$) connected to a methylamino group (CH_2NH_3). At room temperature, $(BA)_2PbI_4$ crystallizes in the orthorhombic *Pbca* space group, with lattice constants $a<b$. The system undergoes a structural phase transition at 275 K (Tc), after which it still crystallizes in the orthorhombic *Pbca* space group but with lattice constants $a>b$. In contrast, $(PEA)_2PbI_4$ does not undergo a structural transition from 80 K to 300 K and crystallizes in the triclinic $P\bar{1}$ space group. These findings are consistent with other literature studies on these materials [91,135–139]. The details of unit cell parameters obtained from the refinement of XRD patterns are shown in Table 3.1. The initial reference crystal structure for refinement of our XRD patterns were taken from [135] for $(BA)_2PbI_4$ and [91] for $(PEA)_2PbI_4$.

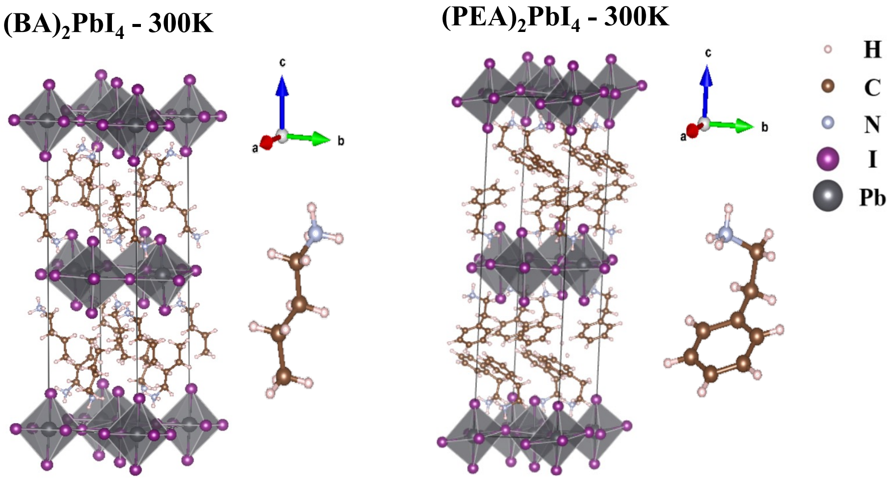

Figure 3.1: Crystal structure of $(BA)_2PbI_4$ and $(PEA)_2PbI_4$ generated using VESTA [49] at 300K based on structural parameters obtained from XRD pattern refinement.

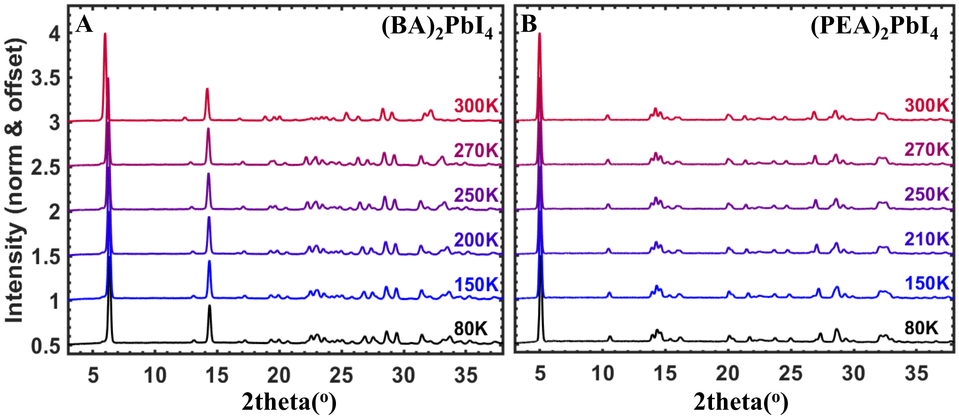

Figure 3.2: Temperature dependent X-Ray diffraction patterns obtained from Bruker D8 VENTURE dual wavelength Mo/Cu Kappa four-circle diffractometer for (A)$(BA)_2PbI_4$ and (B)$(PEA)_2PbI_4$

In these layered HOIPs, inorganic layer distortions are considered an important parameter that affects the structural and electronic properties. The distortions are generally manifested as octahedral tilts or re-alignment in these materials. Previous studies by Ziegler et al. [76] and Dyksik et al. [77] reported a decrease in the out-of-plane octahedral tilt angle in $(BA)_2PbI_4$ as the system transitions from the low-temperature (LT) phase (T<275 K) to the high-temperature (HT) phase (T>275 K). Similar observations were made in this work based on refining the temperature-dependent XRD patterns (Fig.3.3). The octahedral tilt angle (δ) was measured according to the schematic in Fig.3.3(A) [77].

Table 3.1: Summary of crystal structure parameters based on the refinement of XRD patterns for $(BA)_2PbI_4$ and $(PEA)_2PbI_4$ using GSASII [140]

Compound	$(BA)_2PbI_4$		$(PEA)_2PbI_4$	
T/K	300	80	300	80
Space group	*Pbca*	*Pbca*	$P\bar{1}$	$P\bar{1}$
$a/\AA$	8.8842(6)	8.4145(3)	8.762(1)	8.687(3)
$b/\AA$	8.6963(5)	8.9777(3)	8.729(1)	8.674(3)
$c/\AA$	27.6322(12)	26.0739(7)	33.017(11)	32.336(10)
α (°)	90	90	84.39(3)	85.39(3)
β (°)	90	90	84.79(1)	85.15(2)
γ (°)	90	90	89.64(1)	89.46(1)

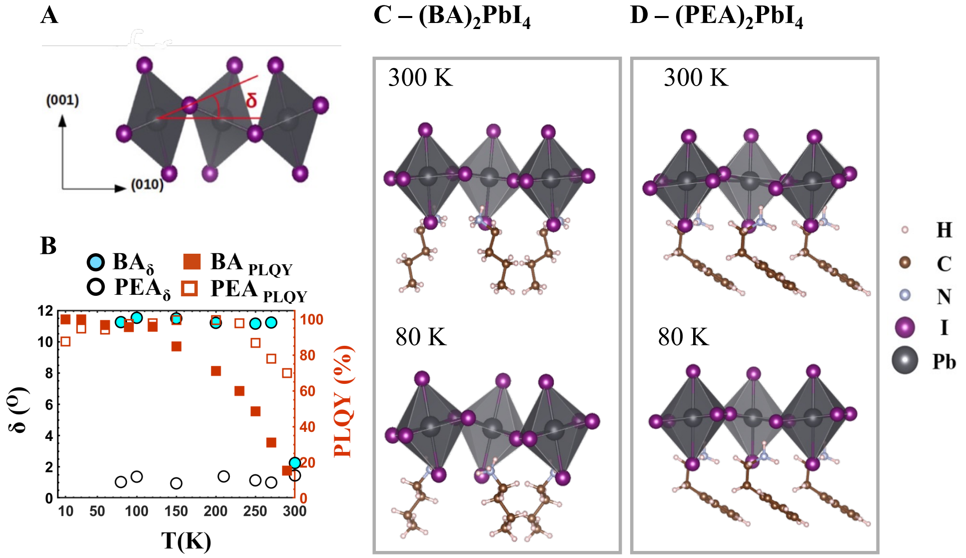

Figure 3.3: (A) Schematic of out of plane octahedral tilt angle (δ) referenced from [77] (B) Comparison of variation of δ and PLQY with temperature for $(BA)_2PbI_4$. The black closed circles with cyan face color represent the δ values obtained on performing structural refinement on XRD patterns. Orange closed squares represent the temperature dependent PLQY of $(BA)_2PbBr_4$ and $(PEA)_2PbBr_4$ reported in [115] Schematic of octahedral distortion observed in (C) $(BA)_2PbI_4$ at 80K and 300K and (D) $(PEA)_2PbI_4$ at 80K and 300K. The images of crystal structures were generated using VESTA [49] after structural refinement on the XRD patterns using GSAS II [140].

For $(BA)_2PbI_4$, δ does not show much change on warming from 80 K to 270 K (Fig.3.3(B)), above which it drops from approximately 11.20° to 2.20° at the room temperature. This aligns with the structural phase transition at 275 K. For $(PEA)_2PbI_4$, we couldn't find any major changes in the average structure from 80 K to 300 K.

As reported by Gong and his colleagues [115], upon warming, PLQY remains almost constant up to 150 K for ($(BA)_2PbBr_4$ and 225 K for $(PEA)_2PbBr_4$, and upon further warming it starts to decrease, which we think would be similar in $(BA)_2PbI_4$ and $(PEA)_2PbI_4$. Note that the study by Ziegler et al [76] indeed showed that for $(BA)_2PbI_4$, though octahedral tilts can be correlated to the electronic band gap, they do not have a dominant influence in the exciton binding energy, rather they remain more robust at the phase transition. Thus, the observed temperature-dependent evolution of octahedral tilts indicates that the distortion of inorganic layers does not correlate explicitly with PLQY in these two 2D HOIPs. A pictorial representation of these octahedral distortions in both $(BA)_2PbI_4$ and $(PEA)_2PbI_4$ is shown in Fig.3.3(C) and (D).

3.2.2 Rotational Dynamics

In a quantum well confinement structure, where the polarized organic molecule layer serves as the 'wall' and the inorganic layer serves as the 'well', the dynamics behaviors of both the 'wall' and 'well' are expected to dominate exciton dynamics. Inspired by influences from molecular re-orientations in 3D HOIPs [69], we first concentrated on the rotational dynamics of polarized organic molecules in these 2D HOIPs. Due to neutrons' high sensitivity to hydrogen, the rotational motion of hydrogen-rich molecules can be directly probed as incoherent diffuse intensity, using Quasi Elastic Neutron Scattering (QENS) (Fig. 3.4). At 180 K, the neutron scattering intensity concentrates sharply in the elastic channel for both systems. Upon heating, in $(BA)_2PbI_4$ the intensity quickly diffuses into the quasi-elastic region while in $(PEA)_2PbI_4$ the intensity mostly stays in the elastic channel and shows only slight increments in the quasi-elastic region. The enhanced QENS intensity in $(BA)_2PbI_4$ indicates much stronger molecular rotational dynamics in $(BA)_2PbI_4$ than in $(PEA)_2PbI_4$. Note that in both materials, the number of molecules in one unit cell is two and the number of hydrogen atoms on each molecule is the same, which means the incoherent QENS intensity is a direct manifestation of the robustness of molecular rotations.

To quantitatively understand the rotational motion of organic molecules, we applied the Jump model analysis [102, 127] along with group theory analysis. The rotation model that accounts for the preferential molecular orientation is called the Jump model. The rotational dynamics of the organic cation are determined by its

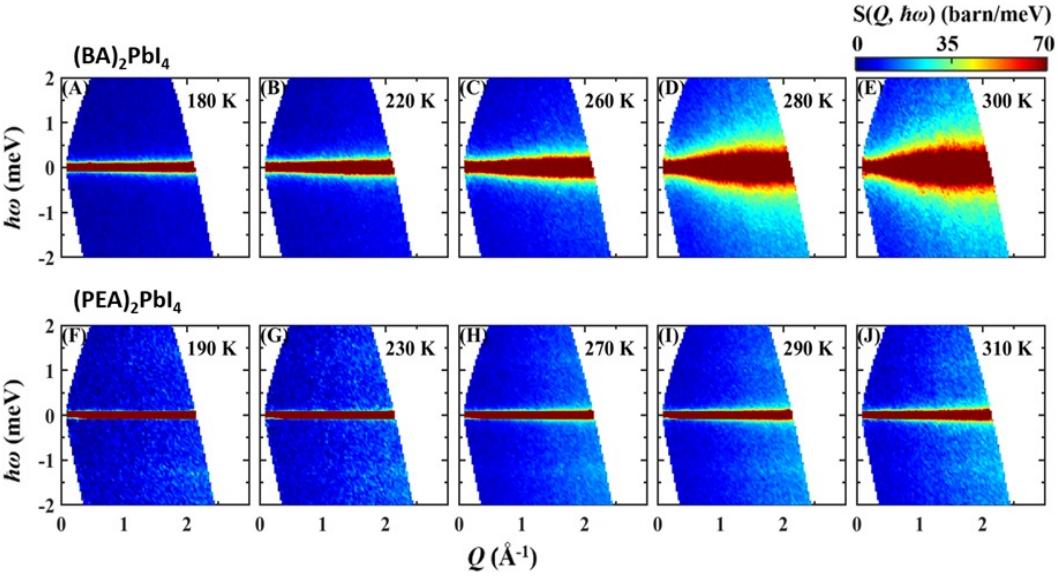

Figure 3.4: Temperature-dependent quasi-elastic neutron scattering spectra of (BA)$_2$PbI$_4$ (A-E) and (PEA)$_2$PbI$_4$(F-J) obtained from AMATERAS upon heating

symmetry and the local crystal symmetry. The possible rotational modes are described as the irreducible representations of the direct product $\Gamma = C \otimes M$ where C and M are the point groups of the local crystal symmetry and the molecule symmetry. In group theory, the static and dynamic structure factor for rotational motions of molecules in a crystal can be written as [35]

$$S_{cal}(Q, \hbar\omega) = e^{-\langle u^2 \rangle Q^2} \left(\sum_{\gamma} A_{\gamma}(Q) \frac{1}{\pi} \frac{\omega_{\gamma}}{1 + \omega^2 \tau_{\gamma}^2} \right) \tag{3.2.1}$$

where the sum over γ runs over all the irreducible representations of the system group $\Gamma\,(\Gamma_{\gamma})$; $e^{-\langle u^2 \rangle Q^2}$ is the Debye Waller factor, $\langle u^2 \rangle$ is the mean squared atomic displacement. For a polycrystalline sample, $A_{\gamma}(Q)$ is given by [127]

$$A_{\gamma}(Q) = \frac{l_{\gamma}}{g} \sum_{\alpha} \sum_{\beta} \chi_{\gamma}^{\alpha\beta} \sum_{C_{\alpha}} \sum_{M_{\beta}} j_0 \left(Q \left| R - C_{\alpha} M_{\beta} R \right| \right) \tag{3.2.2}$$

Here g is the order of group Γ and l_{γ} is the dimensionality of Γ_{γ}. The sums over α and β run over all the classes of C and M, respectively, and the sums over C_{α} and M_{β} run over all the rotations that belong to the crystal class, α, and to the molecule class, β, respectively. The characters of Γ_{γ}, $\chi_{\gamma}^{\alpha\beta}$,are the products of the characters of $C_{\gamma C}$ and $M_{\gamma M}$; $\chi_{\gamma}^{\alpha\beta} = \chi_{\gamma C}^{\alpha} \chi_{\gamma M}^{\beta} \cdot j_0(x)$ is the zeroth spherical Bessel function and, $|R - C_{\alpha} M_{\beta} R|$, is the distance between the initial atom position R and final atom position $C_{\alpha} M_{\beta} R$, called the Jump distance. The relaxation time for the Γ_{γ} mode, τ_{γ}, is written as [35]

$$\frac{1}{\tau_\gamma} = \sum_\alpha \frac{n_\alpha}{\tau_\alpha}\left(1 - \frac{\chi_\gamma^{\alpha e}}{\chi_\gamma^{Ee}}\right) + \sum_\beta \frac{n_\beta}{\tau_\beta}\left(1 - \frac{\chi_\gamma^{E\beta}}{\chi_\gamma^{Ee}}\right) \tag{3.2.3}$$

where n_α, n_β are the number of symmetry rotations of the classes, α and β, respectively. E and e represent the identity operations of C and M, respectively.

To fit the quasi-elastic neutron scattering spectra, the calculated $S_{\mathrm{cal}}\left(Q, \hbar\omega\right)$ has to be convoluted with the instrument resolution. The phonon contributions are also estimated in the form of incoherent phonon scattering. Then we have the fitting function as

$$S(Q, \hbar\omega) = A_{rot} \int_{-\infty}^{\infty} S_{cal}\left(Q, \hbar\omega - \hbar\omega'\right) S_{res}\left(\hbar\omega'\right) d\left(\hbar\omega'\right) + A_{vib} Q^2 e^{-\left\langle u^2 \right\rangle Q^2} \tag{3.2.4}$$

where $S_{\mathrm{res}}\left(\hbar\omega\right)$ is the instrument resolution function. A_{rot} and A_{vib} are the scaling factors for the rotational contributions and the vibrational contributions.

Based on our previous study on the Jump model analysis of $\mathrm{MAPbI_3}$ [127], we propose two rotational modes for $\mathrm{(BA)_2PbI_4}$: three-fold ($\mathrm{C_3}$) and four-fold ($\mathrm{C_4}$) modes. Table 3.2 shows the character tables for point group C_3 and C_4. The terminal $\mathrm{NH_3}$ and $\mathrm{CH_3}$ groups experience rotational mode $\Gamma = C_4 \otimes C_3$ and the rest of $\mathrm{CH_2}$ groups experience $\Gamma = C_4$. Based on direct product rules in group theory and equivalent atomic position distributions (Fig. 3.5), we can calculate the corresponding τ_γ and $A_\gamma(Q)$ for them (Table 3.4, 3.5). Eventually, we will see if the proposed rotational model works well with our experimental data.

Table 3.2: Character tables for C_3 and C_4. The point group $\mathrm{C_3}$ has two irreducible representations: one one-dimensional representation A, and one two-dimensional representation E. The point group $\mathrm{C_4}$ has three irreducible representations: two one-dimensional representations A and B, and one two-dimensional representation E.

C_3 group	E	$2C_3$
A	1	1
E	2	-1

C_4 group	E	$2C_4$	C_2
A	1	1	1
B	1	-1	1
E	2	0	-2

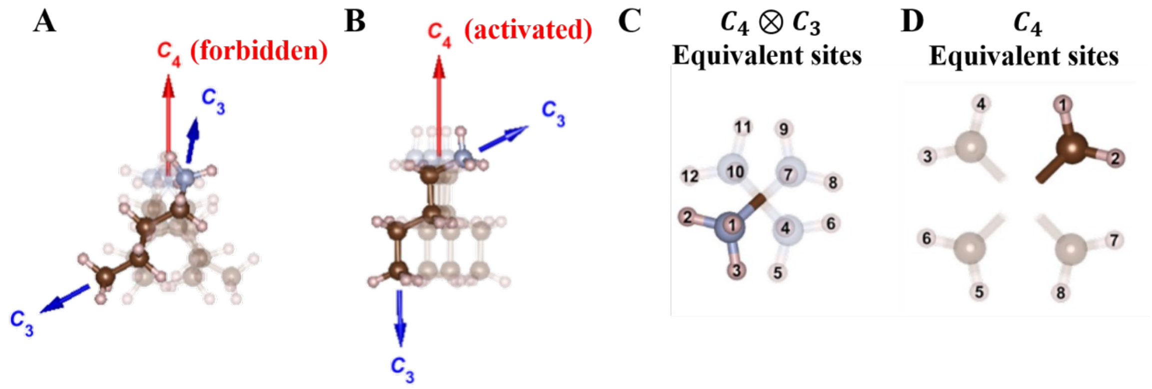

Figure 3.5: Rotational modes of $(BA)_2PbI_4$ and equivalent H sites for NH_3, CH_3, and CH_2 groups. (A and B) show the rotational modes of BA^+molecules (A) when C_4 is frozen and terminal NH_3 and CH_3 groups experience $\Gamma = C_3$ (B) when the terminal NH_3 and CH_3 groups experience $\Gamma = C_4 \otimes C_3$ and the CH_2 groups experience $\Gamma = C_4$. (C) presents the 12 equivalent H sites for the $C_4 \otimes C_3$ mode of NH_3 and CH_3 groups. (D) presents the 8 equivalent H sites for the C_4 mode of CH_2 groups.

Table 3.4: Model details for Jump mode $\Gamma = C_4 \otimes C_3$.

Γ_γ	$\frac{1}{\tau_\gamma}$	$36 \cdot A_\gamma(Q)$
A ⊗ A	0	$3 + 6j_1 + 2j_2 + 2j_3 + 2j_4 + j_5 + 2j_6 + 2j_7 + 2j_8 + 2j_9$ $+2j_{10} + 2j_{11} + j_{12} + 2j_{13} + 2j_{14} + 2j_{15} + j_{16}$
A ⊗ E	$\frac{3}{\tau_{C_3}}$	$6 - 6j_1 + 4j_2 - 2j_3 - 2j_4 + 2j_5 - 2j_6 - 2j_7 - 2j_8 - 2j_9$ $+4j_{10} - 2j_{11} + 2j_{12} - 2j_{13} - 2j_{14} + 4j_{15} + 2j_{16}$
B ⊗ A	$\frac{4}{\tau_{C_4}}$	$3 + 6j_1 - 2j_2 - 2j_3 - 2j_4 + j_5 + 2j_6 + 2j_7 - 2j_8 - 2j_9$ $-2j_{10} - 2j_{11} + j_{12} + 2j_{13} - 2j_{14} - 2j_{15} + j_{16}$
B ⊗ E	$\frac{4}{\tau_{C_4}} + \frac{3}{\tau_{C_3}}$	$6 - 6j_1 - 4j_2 + 2j_3 + 2j_4 + 2j_5 - 2j_6 - 2j_7 + 2j_8 + 2j_9$ $-4j_{10} + 2j_{11} + 2j_{12} - 2j_{13} + 2j_{14} - 4j_{15} + 2j_{16}$
E ⊗ A	$\frac{2}{\tau_{C_4}}$	$6 + 12j_1 - 2j_5 - 4j_6 - 4j_7 - 2j_{12} - 4j_{13} - 2j_{16}$
E ⊗ E	$\frac{2}{\tau_{C_4}} + \frac{3}{\tau_{C_3}}$	$12 - 12j_1 - 4j_5 + 4j_6 + 4j_7 - 4j_{12} + 4j_{13} - 4j_{16}$

Here j_i represent the zeroth spherical Bessel function $j_0\left(Qr_i\right)$, where r_i are the Jump distances corresponding to the Jump positions in Fig. 3.5: $r_1 = R_{1,2}, r_2 = R_{1,4}, r_3 = R_{1,5}, r_4 = R_{1,6}, r_5 = R_{1,7}, r_6 = R_{1,8}, r_7 = R_{1,9}, r_8 = R_{1,11}, r_9 = R_{1,12}, r_{10} = R_{2,5}, r_{11} = R_{2,6}, r_{12} = R_{2,8}, r_{13} = R_{2,9},\ r_{14} = R_{2,12}, r_{15} = R_{3,6}, r_{16} = R_{3,9}. R_{i,j} = |\mathbf{R_i} - \mathbf{R_j}|$, where $\mathbf{R_i}$ is the position of the i-th H site. The 12 equivalent H sites for NH_3 and CH_3 are marked in Fig. 3.5(C).

Table 3.5: Model details for Jump mode $\Gamma = C_4$.

Γ_γ	$\frac{1}{\tau_\gamma}$	$8 \cdot A_\gamma(Q)$
A	0	$2 + 2j_2 + j_4 + 2j_7 + j_8$
B	$\frac{4}{\tau_{C_4}}$	$2 - 2j_2 + j_4 - 2j_7 + j_8$
E	$\frac{2}{\tau_{C_4}}$	$4 - 2j_8$

Here j_i represents the zeroth spherical Bessel function $j_0(Qr_i)$, where r_i are the Jump distances corresponding to the Jump positions in Fig. 3.5: $r_2 = R_{1,3}, r_4 = R_{1,5}, r_7 = R_{2,4}, r_8 = R_{2,6}.R_{i,j} = |\mathbf{R_i} - \mathbf{R_j}|$, where $\mathbf{R_i}$ is the position of the i-th H site. The 8 equivalent H sites for CH_2 groups are marked in Fig. 3.5(D).

For $(PEA)_2PbI_4$, only one rotational mode is proposed: the C_3 mode of the terminal NH_3 group (Table. 3.2). The structure factors $A_\gamma(Q)$ for $\Gamma = C_3$ is calculated in Table 3.6.

Table 3.6: Model details for Jump mode $\Gamma = C_3$

Γ_γ	$\frac{1}{\tau_\gamma}$	$9 \cdot A_\gamma(Q)$
A	0	$3 + 6j_0(Qr)$
E	$\frac{3}{\tau_{C_3}}$	$6 - 6j_0(Qr)$

j_0(Qr) is the zeroth spherical Bessel function. r is the Jump distance between H atoms of the NH_3 group.

The proposed rotational models for the two samples work well with the experimental data (Fig. 3.6 and Fig. 3.7), demonstrating their validity. The fitted parameters are reported in Table 3.7. The fitting based on proposed models suggests that there are two intrinsic rotational modes for $(BA)_2\,PbI_4$: a C_3 mode of the terminal NH_3 and CH_3 groups in BA molecule at both low-temperature (LT) Pbca phase ($T < 275$ K) and high-temperature (HT) Pbca phase ($T > 275$ K), and a C_4 mode of the entire BA molecule about the crystallographic c-axis which gets activated only at the HT Pbca phase. For $(PEA)_2PbI_4$, our analysis suggests a single C_3 mode of the terminal NH_3 group throughout the temperature of interest. At the base temperature for both systems (10 K for $(BA)_2PbI_4$ and 8 K for $(PEA)_2PbI_4$) any rotations are frozen so that the elastic channel intensity of QENS data can be described just with the instrument resolution function ($S_{res}(\hbar\omega)$).

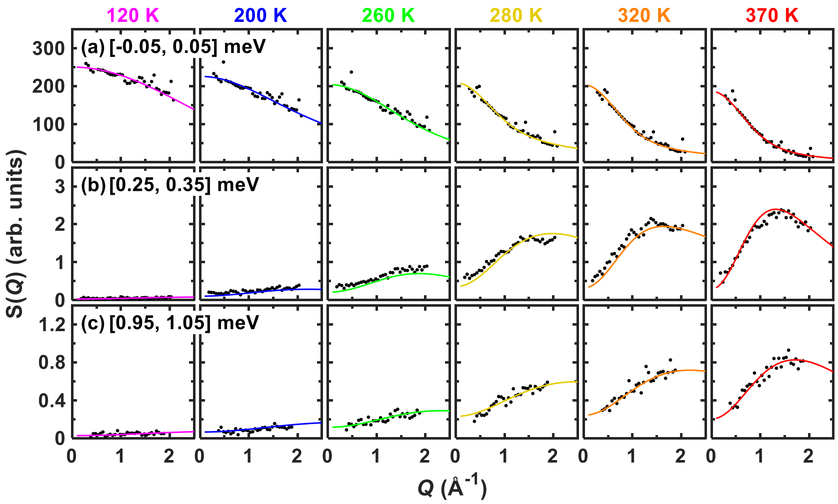

Figure 3.6: Constant energy slices of QENS spectra and fitting results of $(BA)_2PbI_4$. (A - C) the $\hbar\omega$ integrated QENS data, S(Q), over three different energy ranges, $-0.05 < \hbar\omega < 0.05$meV (A), $0.25 < \hbar\omega < 0.35$meV (B), $0.95 < \hbar\omega < 1.05$meV (C), with five selected temperatures, 180 K, 220 K, 260 K (low-T Pbca orthorhombic phase), 280 K, 300 K (high-T Pbca orthorhombic phase). The black dots are the measured data, and the colored solid lines are the model-fitted QENS intensity.

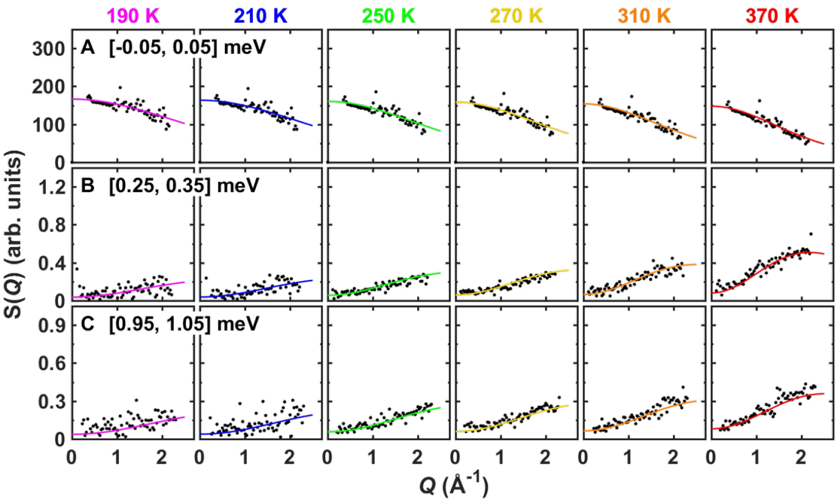

Figure 3.7: Constant energy slices of QENS spectra and fitting results of $(PEA)_2PbI_4$. (A - C) the $\hbar\omega$ integrated QENS data, S(Q), over three different energy ranges, $-0.05 < \hbar\omega < 0.05$meV(A), $0.25 < \hbar\omega < 0.35$meV (B), $0.95 < \hbar\omega < 1.05$meV (C), with five selected temperatures, 190 K, 230 K, 270 K, 290 K, 310 K (triclinic $P-1$ single phase). The black dots are the measured data, and the colored solid lines are the model-fitted QENS intensity.

Table 3.7: Estimated relaxation times, τ_{C_4} and τ_{C_3}, and the mean squared displacement for the rotations of organic molecules in $(BA)_2PbI_4$ and $(PEA)_2PbI_4$ that are extracted from the model fitting to the QENS data

$(BA)_2PbI_4$				$(PEA)_2PbI_4$		
T(K)	τ_{C_4}(ps)	τ_{C_3}(ps)	$\langle u^2 \rangle$ ($\AA^2$)	T(K)	τ_{C_3}(ps)	$\langle u^2 \rangle$ ($\AA^2$)
160	∞	342(10)	0.110(4)	170	588(90)	0.067(4)
180	∞	201(4)	0.108(3)	190	497(66)	0.073(4)
200	∞	104(2)	0.116(3)	210	408(50)	0.079(4)
220	∞	87(2)	0.104(3)	230	243(20)	0.087(4)
240	∞	70(2)	0.122(4)	250	177(12)	0.095(4)
260	∞	45(1)	0.156(3)	270	125(7)	0.103(3)
280	60(3)	6.8(2)	0.085(2)	290	92(5)	0.110(3)
300	25(2)	3.5(2)	0.082(3)	310	71(4)	0.118(3)

In 3D HOIPs, our previous study [141] showed that the entropy contribution to the Gibbs free energy caused by rotations of polarized organic molecules plays a significant role in structural phase transition. Here in these 2D HOIPs, the BA molecule possesses larger rotational moments of inertia than the PEA molecule, which brings it higher rotational entropy. Therefore, it is reasonable to expect that molecular rotations would have a greater impact on the dynamics of the inorganic framework and the dielectric environment surrounding confined excitons in $(BA)_2PbI_4$ compared to $(PEA)_2PbI_4$. It is important to note that the elastic channel intensity ($-0.05 < \hbar\omega < 0.05$ meV) decays much faster in Q , for $(BA)_2PbI_4$ above 180 K (Fig. 3.6(A)), while for $(PEA)_2PbI_4$ (Fig. 3.7(A)), it do not show a significant change. This is reflected in the lifetimes of the C_3 rotational modes for both systems (Fig. 3.8). Comparing similar temperatures, the C_3 rotational modes for $(BA)_2PbI_4$ has shorter rotational relaxation times than $(PEA)_2PbI_4$. This suggests more robust molecular rotational motions in $(BA)_2PbI_4$. These observations imply that the rotational dynamics of organic molecules in these 2D HOIPs could significantly influence charge dynamics and optoelectronic performance. To demonstrate this, we compare the temperature-dependent evolution of QENS spectra with that of PLQY, which will be discussed in later sections.

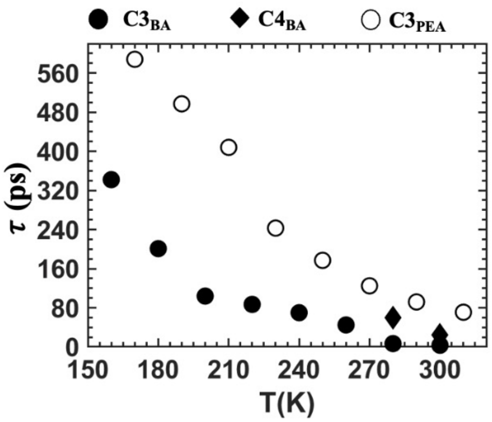

Figure 3.8: Estimated relaxation times (τ) for the rotations of organic molecules in $(BA)_2PbI_4$ and $(PEA)_2PbI_4$ that are extracted from the model fitting to the QENS data. The closed circles represent three-fold (C_3) mode of the terminal NH_3 and CH_3 groups in BA molecule. The closed diamonds represent four-fold (C_4) mode along the crystallographic c-axis of BA molecule. The open circles represent the three-fold (C_3) mode of the terminal NH_3 group in PEA molecule.

3.2.3 Vibrational Dynamics

To properly evaluate the potential influences from lattice vibrations, we need to carefully categorize the multiple types of phonons in these 2D HOIPs as they carry different functionalities in optoelectronic performance. Based on their refined crystal structures, we performed DFT calculations of their phonon band structures and simulated base temperature Inelastic Neutron Scattering (INS) spectra using OCLIMAX [142]. The simulated INS spectra of $(BA)_2PbI_4$ reproduced the observed data decently well (Fig. 3.9 and Fig. 3.11(A)), but for $(PEA)_2PbI_4$ there are some discrepancies in the low energy ($\hbar\omega < 10$meV) region (Fig. 3.10 and Fig. 3.11(B)). This could be due to the low crystal symmetry (triclinic $P\overline{1}$) of $(PEA)_2PbI_4$ with many 188 atoms in one crystal unit cell, which brings in structural instability and makes the calculation of low-energy acoustic and optical phonons much more challenging.

Based on the DFT calculations, we characterized the phonon modes into three different types: inorganic phonon modes, hybrid phonon modes, and organic phonon modes based on the vibration energy fraction (VEF) calculation. VEF determines the fractional energy contribution of each atomic type in the unit cell, for the phonon modes present (see Appendix B for VEF calculation details). Figures 3.9(D) and 3.10(D), show the VEF for $(BA)_2PbI_4$ and $(PEA)_2PbI_4$ respectively. The phonon

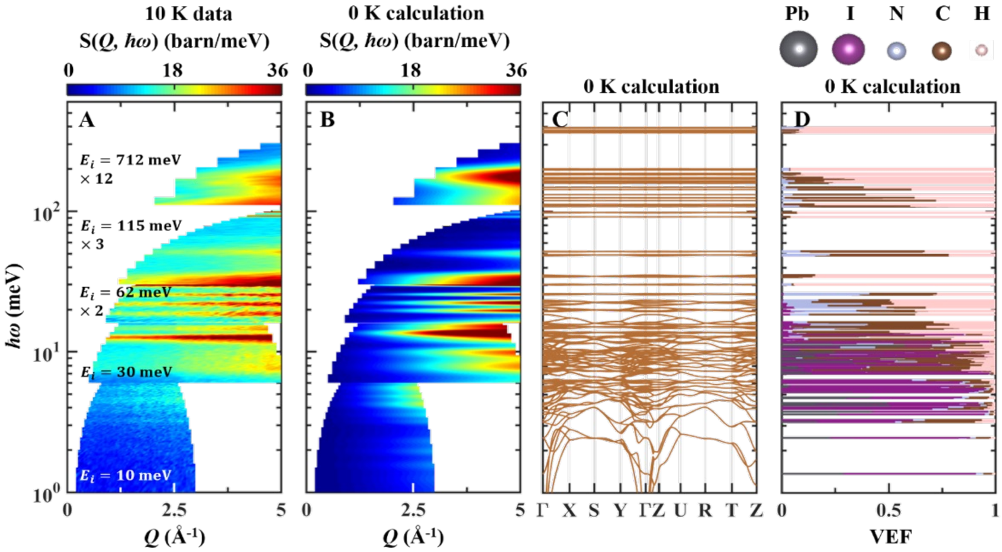

Figure 3.9: Experimental phonon spectra and DFT calculation results of $(BA)_2PbI_4$. (A) shows the experimental phonon spectra of $(BA)_2PbI_4$ taken at 10 K with $\mathrm{E_i} = 10, 30, 62, 115, 712\mathrm{meV}$. The intensities of $E_i = 62, 115$, and 712 meV are rescaled by 2,3 , and 12 respectively. (B) shows the simulated phonon spectra using software OCLIMAX [142]. (C) presents the calculated phonon band structure along high-symmetry reciprocal $\mathbf{Q}$ points, $\Gamma = (0,0,0), \mathrm{X} = \left(\frac{1}{2},0,0\right), \mathrm{S} = \left(\frac{1}{2},\frac{1}{2},0\right), \mathrm{Y} = \left(0,\frac{1}{2},0\right), Z = \left(0,0,\frac{1}{2}\right), U = \left(\frac{1}{2},0,\frac{1}{2}\right), R = \left(\frac{1}{2},\frac{1}{2},\frac{1}{2}\right)$, and $T = \left(0,\frac{1}{2},\frac{1}{2}\right)$. (D) contains the vibrational energy fractions at the Γ point for each phonon mode of $(BA)_2PbI_4$. Here the gray, violet, cyan, brown, and pink spheres represent the energy fractions of $\mathrm{Pb}, \mathrm{I}, \mathrm{N}, \mathrm{C}$, and H atoms, respectively.

modes are classified as inorganic when the majority of atomic vibrations originate from inorganic atoms, Pb and I , with $\mathrm{VEF}_{Pb,I} > 60 \sim 70\%$. Hybrid phonons have significant contributions from both inorganic and organic atoms ($\mathrm{C}, \mathrm{H}, \mathrm{N}$) with $2\% < \mathrm{VEF}_{Pb,I} < 60\%$ and organic phonons with dominant contributions from organic atoms with $\mathrm{VEF}_{Pb,I} < 2\%$. The inorganic phonons mostly reside below $\hbar\omega < 10\mathrm{meV}$, the hybrid phonons between $10\mathrm{meV} < \hbar\omega < 35\mathrm{meV}$, and the pure organic phonons above $\hbar\omega >\sim 35\mathrm{meV}$. The inorganic and hybrid phonons are expected to affect the optoelectronic properties of ionic crystals since they could change the highly polarized ionic bonds inside the samples, which can influence the charge carrier dynamics via Coulomb interactions. Whereas, the pure organic phonons, which involve molecular internal vibration and covalent bond deformation, play a minor role in the optoelectronic performance of the material as they barely show significant temperature dependence (Fig. 3.12). For $(BA)_2PbI_4$ above 35 meV , the scattering intensity do not show much change with temperature (Fig. 3.12(A)). $(PEA)_2PbI_4$ other than a

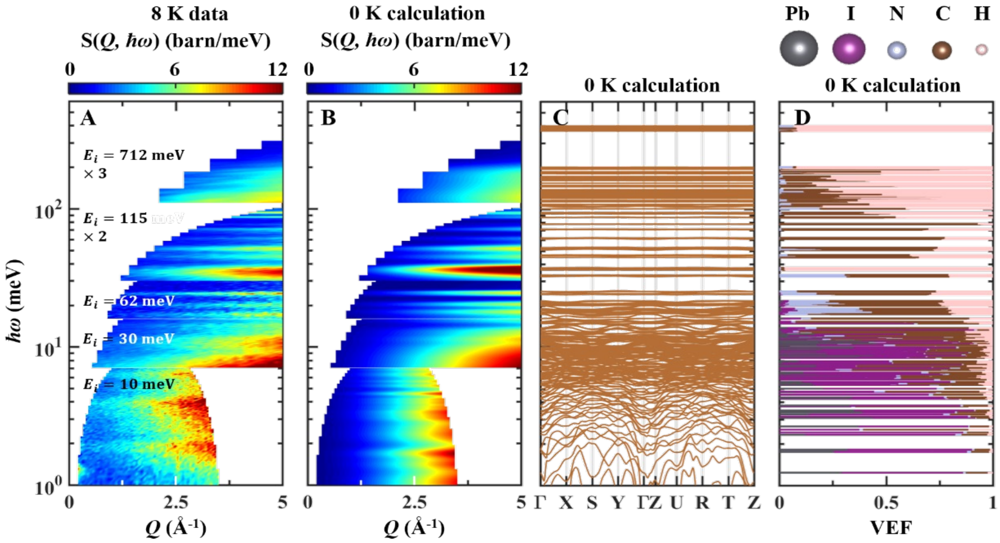

Figure 3.10: Experimental phonon spectra and DFT calculation results of $(PEA)_2PbI_4$. (A) shows the experimental phonon spectra of $(PEA)_2PbI_4$ taken at 10 K with $\mathrm{E_i} = 10, 30, 62, 115, 712\mathrm{meV}$. The intensities of $E_i = 62, 115,$ and 712 meV are rescaled by 2,3 , and 12 respectively. (B) shows the simulated phonon spectra using software OCLIMAX [142]. (C) presents the calculated phonon band structure along high-symmetry reciprocal $\mathbf{Q}$ points, $\Gamma = (0, 0, 0), \mathrm{X} = \left(\frac{1}{2}, 0, 0\right), \mathrm{S} = \left(\frac{1}{2}, \frac{1}{2}, 0\right), \mathrm{Y} = \left(0, \frac{1}{2}, 0\right), Z = \left(0, 0, \frac{1}{2}\right), U = \left(\frac{1}{2}, 0, \frac{1}{2}\right), R = \left(\frac{1}{2}, \frac{1}{2}, \frac{1}{2}\right)$, and $T = \left(0, \frac{1}{2}, \frac{1}{2}\right)$. (D) contains the vibrational energy fractions at the Γ point for each phonon mode of $(PEA)_2PbI_4$. Here the gray, violet, cyan, brown, and pink spheres represent the energy fractions of Pb, I, N, C, and H atoms, respectively.

shift in scattering intensity from base temperature (8 K) to higher temperatures, which we attribute to the increased thermal population, we do not see major temperature dependence above 35 meV (Fig. 3.12(B)). Therefore, we focused on evaluating inorganic and hybrid phonons.

For a comprehensive analysis, combining neutron scattering spectra from different incident energies is crucial to ensure a continuous dataset across all energy transfers. This requires normalizing the measured neutron scattering intensities to absolute units. Due to the large number of hydrogen atoms, the incoherent scattering background is prominent in both systems. Thus, we normalized the neutron scattering using elastic incoherent scattering intensities [143] (Appendix C). After normalization, we connected the QENS spectra collected on AMATERAS to the INS spectra from 4SEASONS at $\hbar\omega \sim 2.25$meV (Figure 3.13(A)(B)). To separate the rotational intensity contributions from vibrational contributions, we applied a single Voigt function centered at $\hbar\omega = 0$ with elastic energy resolution convoluted to represent the molecular rotational contribution and multiple inelastic Voigt functions representing phonon peaks to interpret the rest of INS spectra (Fig. 3.13(C-F)). Upon warming, the phonon peaks become ill-defined and almost smear out at 300 K, which makes it difficult to identify. By fixing the number of phonon peaks and limiting their energy shifts, we managed to reproduce the phonon damping process (peak broadening), although this approach posed significant challenges. In addition, in $(BA)_2PbI_4$ the hybrid phonon intensity counter-intuitively decreased upon warming (Fig. 3.13(A)).

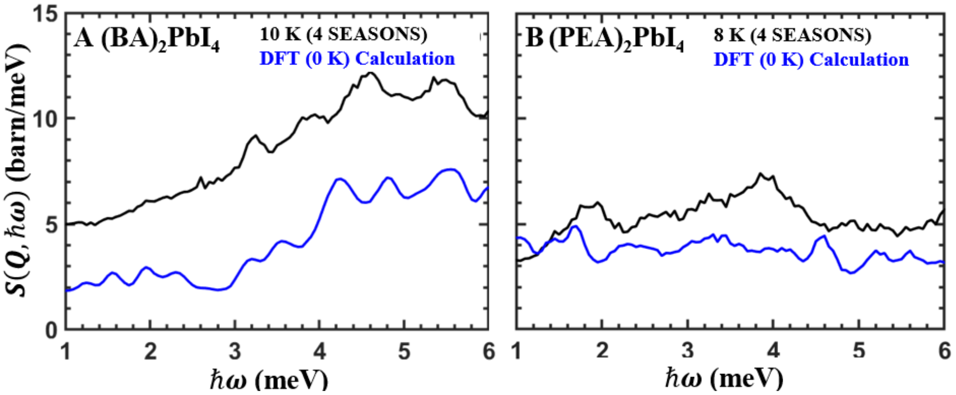

Figure 3.11: Q-integrated phonon spectra obtained from 4 SEASONS for $(BA)_2PbI_4$(A) and $(PEA)_2PbI_4$ (B). The Q-integration range is selected as $[1.5-2]\mathring{A}^{-1}$ which covers dominant phonon signal for both systems.

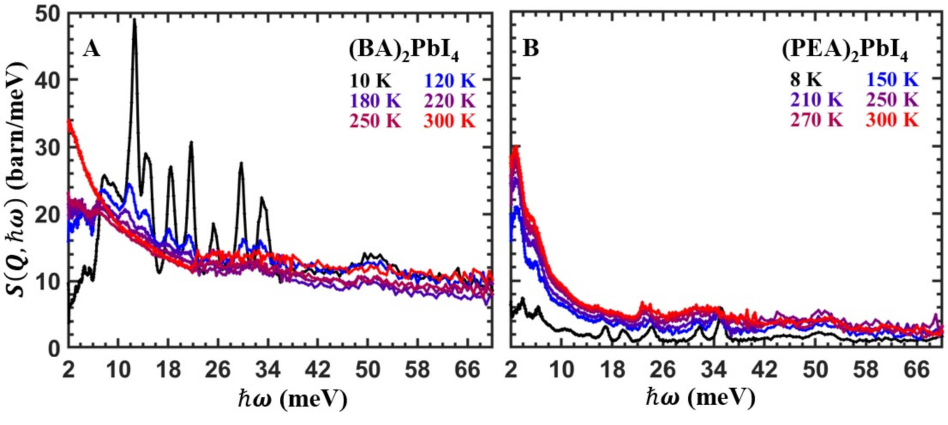

Figure 3.12: Q-integrated phonon spectra obtained from 4 SEASONS for $(BA)_2PbI_4$(A) and $(PEA)_2PbI_4$ (B). The Q-integration range is selected as $[1.5-2]\mathring{A}^{-1}$ which covers dominant phonon signal for both systems.

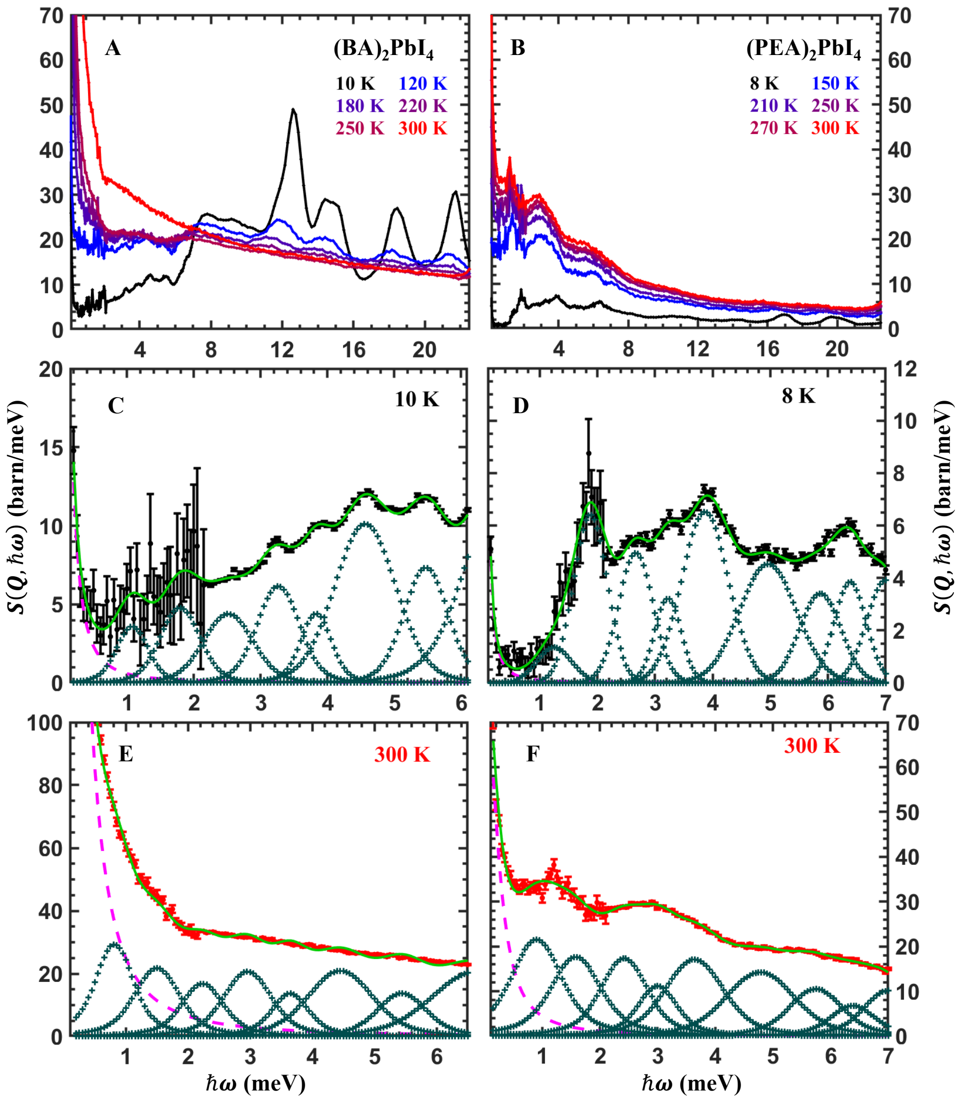

Figure 3.13: Q-integrated phonon spectra of $(BA)_2PbI_4$ (A) and $(PEA)_2PbI_4$ (B) as a function of temperature. The above phonon spectra is plotted after connecting the AMATERAS and 4SEASONS data at 2.25 meV . The Q-integration range is selected as $[1.5-2]\mathring{A}^{-1}$ which covers dominant phonon signal for both systems. Panel C, E and D, F shows the rotational and vibrational contributions after fitting for $(BA)_2PbI_4$ and $(PEA)_2PbI_4$ respectively. The rotational contributions are represented as the magenta dashed lines and the vibrational contributions as (+) dark green symbols.

To back up our analysis, we performed temperature-dependent Raman scattering measurements on powder samples of the two materials (Fig. 3.14). In Raman scattering the Raman inactive rotational modes would be 'filtered' out, leaving the dominant features arising from lattice vibrations. In other words, Raman spectroscopy could help better analyze low energy lattice vibration spectra, which would be 'con-

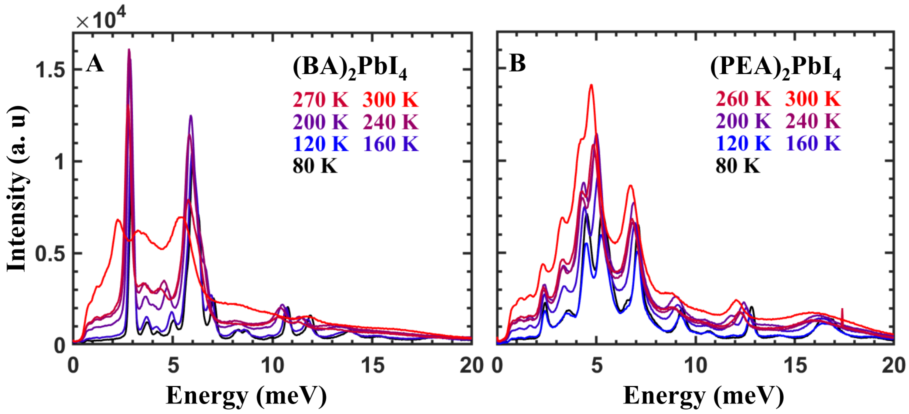

Figure 3.14: Temperature dependent Raman scattering spectra of $(BA)_2PbI_4$ (A) and $(PEA)_2PbI_4$ (B)

taminated' in neutron scattering by the huge incoherent scattering cross section of hydrogen atoms. On the other hand, due to the same factor, the rotational dynamics of hydrogen-rich molecules could be well analyzed in QENS spectra. Comparing the inelastic neutron scattering spectra to Raman spectra for similar temperatures, for both $(BA)_2PbI_4$ (Fig. 3.14(A)) and $(PEA)_2PbI_4$ (Fig. 3.14(B)), the phonon peaks are better defined in the Raman spectra. This is because of the difference in the scattering techniques. In Raman scattering, the wavelength of the incident visible light of 785 nm is much larger than the interatomic distances. Hence the Raman scattering can probe only the phonons with wavevectors (momentum transfers) $8 \times 10^{-4} \mathring{A}^{-1}$, in other words, the Raman scattering probes phonons at Γ point ($Q = 0$) [106], while our neutron scattering probes the powder averaged contribution as a function of Q . Additionally, both the inorganic and hybrid phonon intensities in the Raman spectra intuitively get enhanced upon warming along with graduate peak broadening. All these inelastic spectra will be used in later comparison with the temperature-dependent PLQY.

3.2.4 Photoluminescence

The photoluminescence (PL) spectra of powder samples of $(BA)_2PbI_4$ and $(PEA)_2PbI_4$ are shown in Figure 3.15 (A, B) and (E, F) respectively. At 100 K, $(BA)_2PbI_4$ showed three emission peaks, one peak at $\sim$ 2.4 eV ($P1_{BA}$) and two close peaks at $\sim$ 2.53 eV ($P2_{BA}$) and $\sim$ 2.55 eV ($P3_{BA}$) (Fig. 3.15(C)). Literature studies intensively reported the presence of dual-excitonic emission peak in $(BA)_2PbI_4$ [144–147]. They predict that $(BA)_2PbI_4$ has a dual bandgap formed in the inside and the surface of the crystal - the surface emission ($\sim$ 2.55 eV) and interior emission ($\sim$ 2.4 eV). Our PL emissions confirm the presence of a dual band gap, except that the surface emission shows signatures of two peaks ($P3_{BA}$ and $P3_{BA}$) at 100 K. Up to 220 K the interior emission peak shifts to higher energies beyond which it starts shifting to lower energies. Both surface emission peaks shift to lower energies with an increase in temperature. We observed a sudden drop in both interior and surface emission peak energy above 275 K . This is expected due to the structural phase transition [138, 146].

$(PEA)_2PbI_4$ showed a single emission peak at low temperatures ($P1_{PEA}$) which then underwent a peak splitting above 200 K (Fig. 3.15(G)) The $P1_{PEA}$ shifts to lower emission energies with an increase in temperature. At 200 K a shoulder emission peak emerges at $\sim$ 2.35 eV ($P2_{PEA}$), and the peak splitting becomes more prominent above 220 K (above a minimum energy separation of 0.03 eV) (See Appendix D for specific temperature fitted curves for both systems). Both peaks undergo thermal broadening upon warming (Fig. 3.15(H)). We emphasize that the emission peak splitting becoming prominent in both systems; T 150 K for $(BA)_2PbI_4$ and and T 220 K for $(PEA)_2PbI_4$ occurs despite no change in crystal structure. On the other hand, it is interesting to note that the onset of decrease in PLQY upon heating occurs at similar temperatures for both systems. Additionally, our QENS data shows the activation of rotational dynamics at similar critical temperatures for both systems, which will be discussed in the following section. This suggests that molecular rotation might affect the emission and recombination mechanisms in 2D HOIPs.

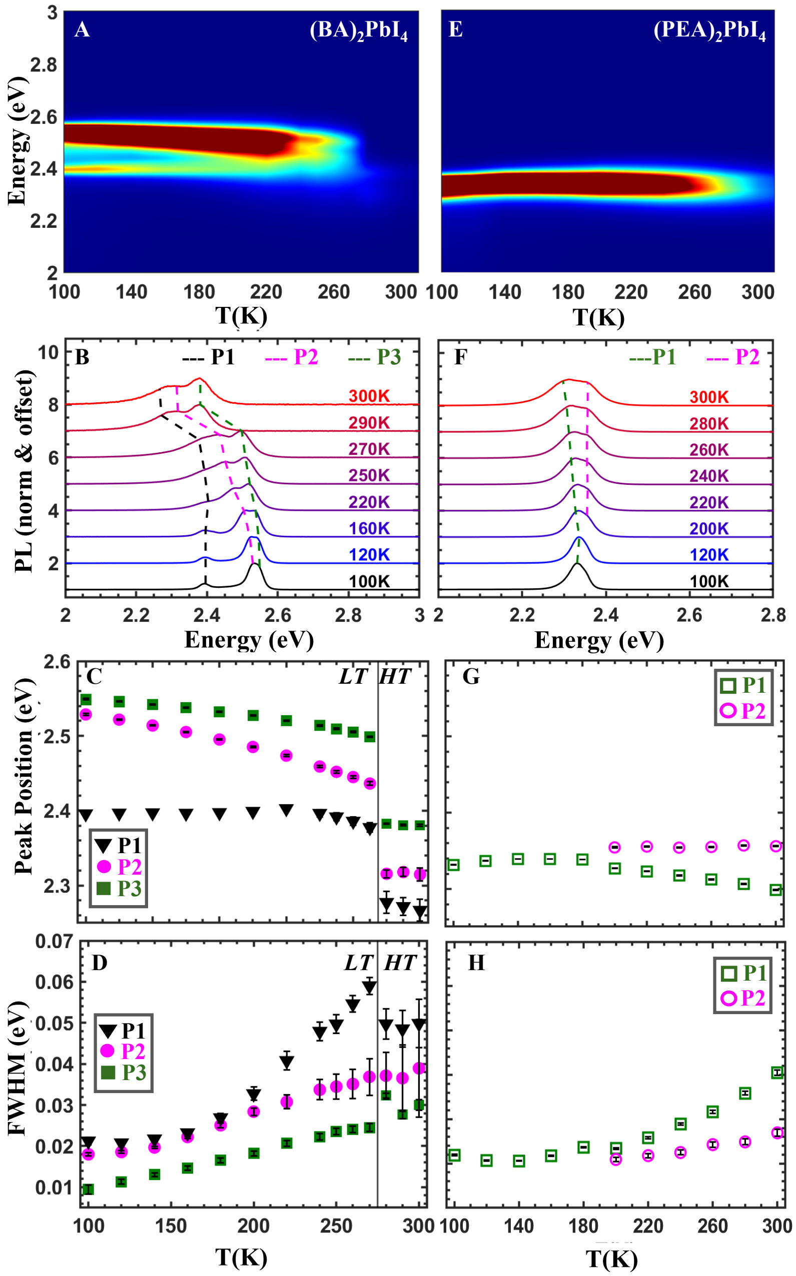

Figure 3.15: Temperature dependent PL Spectra for (BA)$_2$PbI$_4$ (A, B) and (PEA)$_2$PbI$_4$ (E, F). (C)(D) shows the PL emission peak position and peak width respectively for (BA)$_2$PbI$_4$ based on a triple peak fitting. (G)(H) shows the PL emission peak position and peak width respectively for (PEA)$_2$PbI$_4$ based on single peak fitting below 200 K and dual peak fitting from 200 K

3.3 Discussions & Conclusions

In this work, to directly compare the temperature-dependent PLQY of $(BA)_2PbI_4$ and $(PEA)_2PbI_4$, we choose to evaluate the temperature-dependence of corresponding neutron scattering and Raman scattering phonon intensities, neutron scattering intensities from molecular rotations, and PL emission peak widths based on our previous analyses.

Figure 3.16(A)(B) presents the temperature-dependence of inorganic and hybrid phonon intensities probed by Raman and neutron scattering. Both the Raman-probed and neutron-probed inorganic phonons ($[1.5, 4.0]$meV) show consistent temperature dependence - get enhanced monotonically upon warming, which validates our method of separating rotational and vibrational contributions in low-energy INS spectra (Fig. 3.16(A(I)), 3.16(B(I))). Interestingly the hybrid phonons ($[12, 15]$meV) exhibit different behaviors in Raman and neutron scattering for $(BA)_2PbI_4$, while for $(PEA)_2PbI_4$ they are consistent (Fig. 3.16(A(II)), 16((3.16(II)). Comparing the temperature dependence of these phonon intensities with that of PLQY (Fig. 3.16(C)), it tends to suggest that the inorganic and hybrid phonons do not show explicit correlations with this characteristic optoelectronic property.

Figure 3.16(C) showcases the rotational dynamics in these two systems along with the PLQY of their bromide equivalents. Below $\sim$ 140 K and $\sim$ 220 K, respectively, the molecular rotations in $(BA)_2PbI_4$ and $(PEA)_2PbI_4$ are 'frozen', manifested as negligible QENS intensities. Upon heating above these critical temperatures up to 300 K , the rotational dynamics of BA molecules gets greatly enhanced while that of PEA molecules gets slightly strengthened, which is inversely proportional to the temperature dependence of PLQY for both materials. These observations indicate that the molecular rotations in these two HOIPs have non-negligible influences on the intrinsic optoelectronic property. Additionally, the signatures of PL emission peak splitting becoming prominent above 150 K for $(BA)_2PbI_4$ and 220 K for $(PEA)_2PbI_4$ can also be observed as a more dynamic broadening of the emission peaks $P2_{BA}$ and $P2_{PEA}$ (Fig. 3.16(D)) above these critical temperatures. Both $P2_{BA}$ and $P2_{PEA}$ become shoulder peaks to the emission peaks $P3_{BA}$ and $P1_{PEA}$ respectively above their corresponding critical temperatures. The peak splitting could be an indication of breaking of the degeneracy of exciton binding energy levels. This could be due to some local perturbation of the dielectric environment around the exciton. Additionally, the dominant emission peaks ($P3_{BA}$ and $P1_{PEA}$) shifting to lower energies with increase in temperature might be suggesting a reduced exciton binding energy.

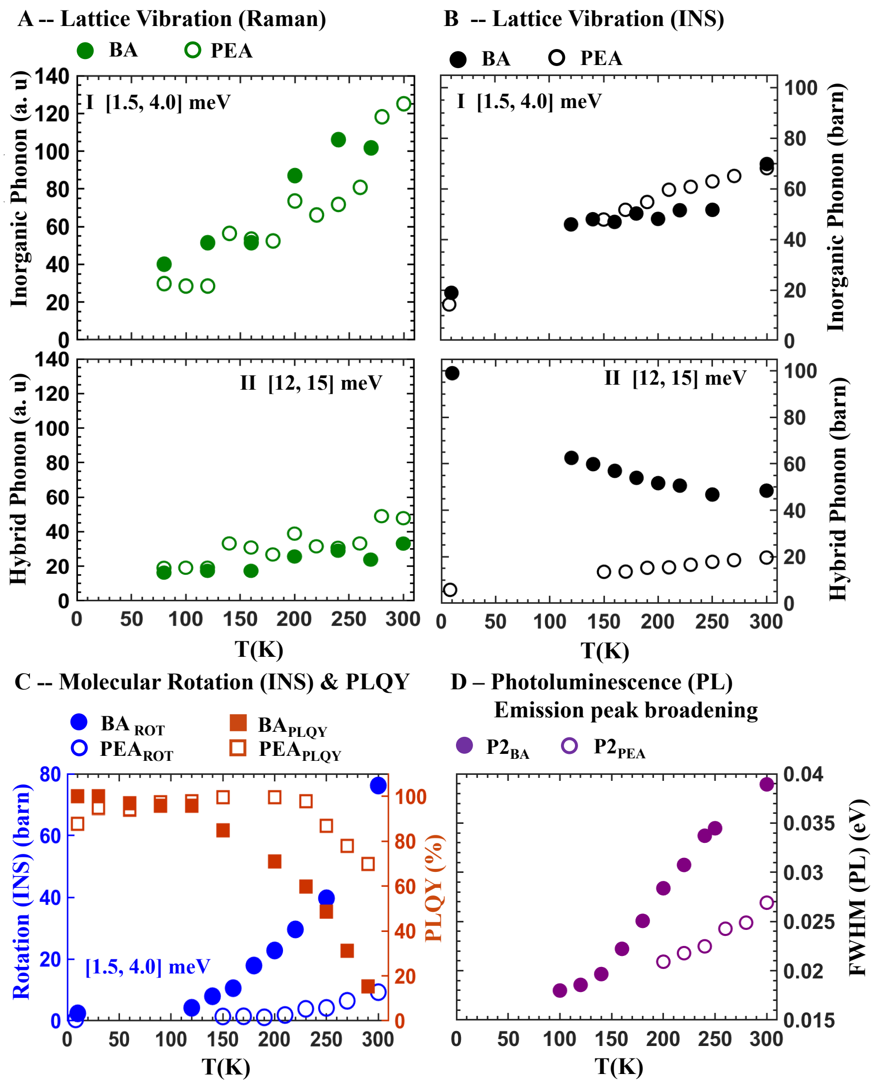

Figure 3.16: (A) Temperature-dependent integrated phonon intensities from Raman scattering for $(BA)_2PbI_4$ and $(PEA)_2PbI_4$ over the energy range of $1.5 \leq \hbar\omega \leq 4.0$meV (I) and over the energy range of $12 \leq \hbar\omega \leq 15$meV (II) and a Q range of $1 \sim 2.5\mathring{A}^{-1}$. (B) Temperature dependent integrated phonon intensities from INS for $(BA)_2PbI_4$ and $(PEA)_2PbI_4$ over the energy range of $1.5 \leq \hbar\omega \leq 4.0$meV and over the energy range of $12 \leq \hbar\omega \leq 15$meV (II) and the same Q range. (C) Blue circles show the rotational intensity contributions of $(BA)_2PbI_4$ and $(PEA)_2PbI_4$ from INS spectra over the energy range of $1.5 \leq \hbar\omega \leq 4.0$meV and same Q range. Orange squares represent the temperature dependent PLQY of $(BA)_2PbBr_4$ and $(PEA)_2PbBr_4$ reported by Ref. [33]. (D) Temperature dependent broadening PL emission peaks for $(BA)_2PbI_4$ $P2_{BA}$ and $(PEA)_2PbI_4$ ($P2_{PEA}$)

But given the complex dynamics in 2D HOIPs and the discrepancies in the reported and calculated exciton binding energies in these systems [64], quantifying them will not be of interest of this research work. Thus, combined with the observations on lattice vibrations, we could propose that: The rotational motion of polarized organic molecules works as dynamical perturbations to the inorganic framework which fundamentally dominates the construction of electronic band structure. These perturbations interfere with the dielectric environment surrounding excitons, potentially reducing the exciton binding energy or breaking the binding energy degeneracy, which can enhance the non-radiative decay of charge carriers and, consequently, suppress the photoluminescence quantum yield (PLQY). To confirm this hypothesis temperature dependent dielectric measurements can be done for these two systems as a next step. More detailed investigations with single-crystals on molecular orientations could reveal the detailed mechanism underlying this rotation-induced optoelectronic effect.

3.4 Summary

In this chapter we discussed our study in understanding the influence of structural dynamics in two 2D HOIPs, $(BA)_2PbI_4$ and $(PEA)_2PbI_4$, on their photoluminescence efficiency. The temperature dependent X-ray diffraction analysis indicates that the distortion of inorganic layers is mainly associated with structural phase transition and does not correlate explicitly with their PLQY. By using QENS and group theory we quantitatively identified the rotational modes of different rotors in these two HOIPs. We carefully separated the rotational intensity contributions and vibrational contributions in the total INS spectra. Complemented by Raman scattering measurements on lattice vibrations and photoluminescence measurements on emission characteristics, we asserted that in these two 2D HOIPs the molecular rotations have non-negligible impacts on their intrinsic opto-electronic property (PLQY) while lattice vibrations do not show explicit correlations. These findings could make essential contributions to the big picture of 2D HOIPs optoelectronics and may guide the design of more efficient light-emitting materials for advanced technological applications.

Chapter 4

PbS Quantum Dot in $CsPbBr_3$ Perovskite Scintillator

Lead halide perovskites (LHPs), such as $CsPbBr_3$, have demonstrated great potential for optoelectronic applications, including solar cells, light-emitting diodes, photodetectors, and scintillators [37,43,45]. These materials are industrially appealing due to their low cost, both in terms of raw materials and manufacturing, thanks to their solution processability. Recent developments have significantly improved the performance of semiconductor devices [25,39]. As mentioned in Chapter 1.4, incorporating quantum dots (QDs) into the perovskite active layer of solar cells, light-emitting diodes, photodetectors, and scintillators can further enhance their performance [35,40]. Adjusting the particle diameter of QDs offers an easy way to tune the band gap due to the quantum confinement of charge carriers within the dots. In some cases, adding QDs has been shown to increase the stability of the perovskite layer, even in humid or high-temperature environments [148–150]. Embedded QDs can serve as bright luminescent centers with tunable emission wavelengths, which are especially useful in light-emitting diodes and scintillator applications.

A schematic of the typical emission mechanism in QD-embedded LHPs is shown in Fig. 4.1. The LHP matrix primarily absorbs incoming X-rays. During absorption, core electrons are excited to energies well above the bottom of the conduction band (at 293 K). As the excited electrons relax, energy is transferred through multiple electron excitations, populating the conduction band while leaving holes in the valence band. Eventually, the charge carriers are collected by QDs, which are chosen to have valence and conduction bands entirely within the bandgap of the LHP. In the QDs, electrons and holes recombine, emitting near-infrared photons. The near-IR emission from QDs minimizes photon reabsorption by the LHP.

Our previous studies on PbS QD-doped $MAPbBr_3$ scintillators with six different

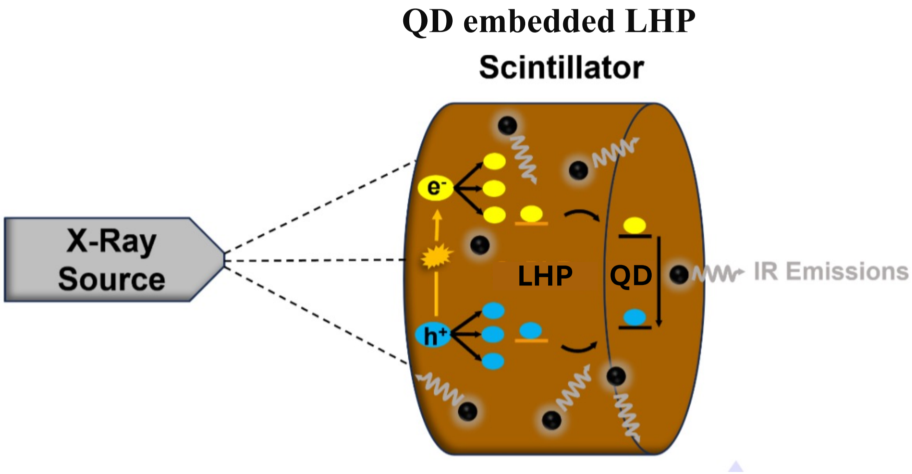

Figure 4.1: Schematic of emission mechanism in Quantum Dot (QD) embedded Lead Halide Perovskite (LHP) scintillator.

QD loadings (QD = 0.01%, 0.05%, 0.1%, 0.5%, 1%, 2%) showed that the scintillator is brightest (Fig. 4.2(A)) and exhibits maximum light yield (Fig. 4.2(A)) at an intermediate QD loading of 0.1%, beyond which the light yield decreases [35]. We hypothesize this is due to the interplay between the distance between QDs, the number of QD emission sites, and the QD reabsorption of photons. PbS QDs tend to reabsorb the emitted low-energy photons in the infrared regime. Therefore, at lower QD concentrations, fewer emission sites result in lower light yield and radioluminescence (RL) intensity, while less reabsorption by QDs increases light yield and RL intensity. At higher concentrations, more emission sites increase light yield and RL intensity, but more reabsorption by QDs reduces light yield and RL intensity. This might explain the maximum scintillator performance at intermediate QD loadings, where the number of emission sites and reabsorption are optimally balanced.

To understand the microscopic mechanism behind the interplay of a number of emission sites and inter-dot interactions, it is necessary to study the size and spatial distribution of QDs in the perovskite matrix. Small-Angle Neutron Scattering (SANS) is ideal for this purpose, as it probes distances much larger than atomic separations, allowing us to capture signals from particles larger than 10 nm and separated by distances greater than 20 nm. However, the large incoherent scattering background from hydrogen interferes with detecting relevant signals. Therefore, we conducted SANS measurements on fully inorganic PbS QD-doped $CsPbBr_3$ with six different QD loadings (QD = 0.01%, 0.05%, 0.1%, 0.5%, 1%, 2%) to investigate QD spatial distribution, along with RL measurements.

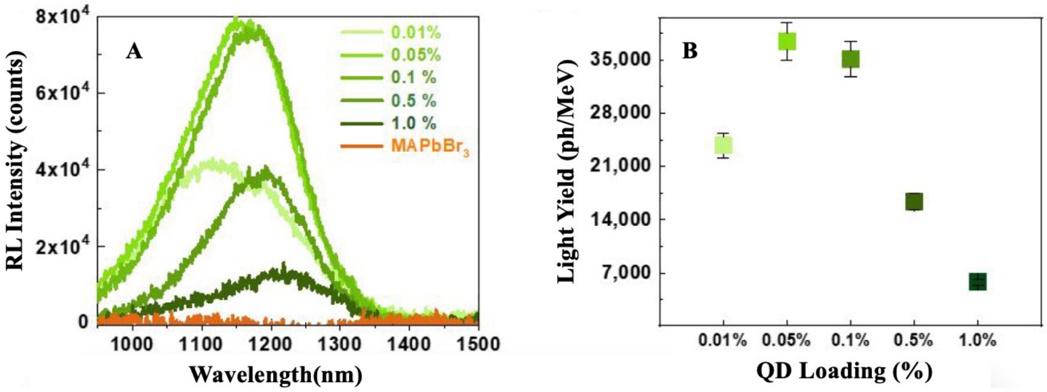

Figure 4.2: RL intensity (A) and Light Yield (B) of PbS (QD) embedded $MAPbBr_3$ with six different QD loadings (QD = 0.01%, 0.05%, 0.1%, 0.5%, 1%, 2%).

Based on our analysis, we found that, similar to PbS-embedded $MAPbBr_3$, PbS-embedded $CsPbBr_3$ exhibited maximum RL intensity at an intermediate loading of 0.5%. Additionally, from SANS, we quantified the QD spatial distribution, which was in the same order of magnitude as the calculated values. Above 0.1%, we did not observe a significant change in the spatial distribution; instead, it appeared to saturate. We hypothesize that this could be due to the inhomogeneous distribution of QDs at higher loadings, with closer QDs in some areas and farther apart QDs in others. This uneven distribution could affect the interactions between QDs, resulting in increased photon reabsorption and reduced RL. Our study highlights that the optoelectronic properties of these systems are very sensitive to the synthesis methods, which in turn affect the incorporation of QDs. We confirm that by optimizing the separation between QDs, the scintillator performance can be significantly improved.

4.1 Experimental Details

The powder samples of PbS embedded $CsPbBr_3$ were synthesized at the Department of Chemical Engineering, University of Virginia, through collaboration (synthesis details provided in Appendix A). Powder X-Ray diffraction to confirm the pure phase was performed at the Malvern PANalytical Empyrean Multipurpose X-ray Diffractometer equipped with a Cu anode in the Department of Chemistry, University of Virginia. Radioluminescence (RL) measurements were conducted with a modified PTI QuantaMaster 400 spectrofluorometer with a model R2658 Visible PMT detector and a Model H10330-75 PMT NIR detector. The X-ray source is a Moxtek 60 kV, 12 W MagPro with a Cr target operated at 40 kV and 300 μA. A $BaSO_4$ coated integrating sphere housed the sample for measurement, and the sample holder was aligned by maximizing the signal of a lab standard scintillator. SANS measurements were performed using the 40 m SANS at HANARO, Republic of Korea. All samples were in powder form and thus measured in a titanium cell at room temperature. The configurations covered the Q range of $0.0008\,\text{Å}^{-1} < Q < 0.5370\,\text{Å}^{-1}$ for all samples, such that the scattering vector, Q, is defined by $Q = \frac{4\pi}{\lambda}\sin\left(\frac{\theta}{2}\right)$. Here, θ and λ are the scattering angle and wavelength, respectively, with $\lambda = 7.49\,\text{Å}$. To cover the entire Q range, the scattering intensities measured under three different SANS configurations (sample to detector distances of 19.8 m, 4.7 m, and 1.16 m) were overlapped. To measure the data in the low Q regions near $0.0008\,\text{Å}^{-1}$ at 19.8 m, a lens was used to refocus the neutron beam. Collected 2D images were converted and reduced to a 1D plot for sample analysis.

4.2 Results and Analysis

4.2.1 X-Ray Diffraction

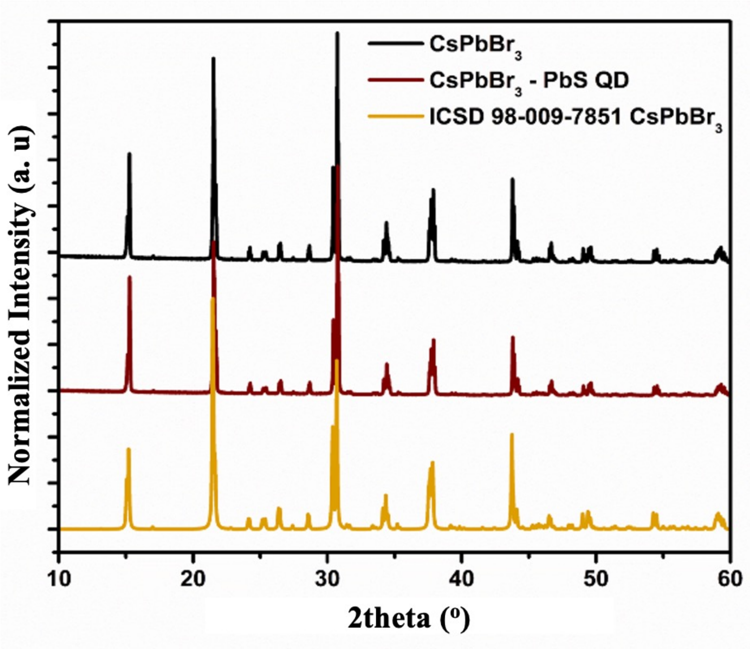

Figure 4.3: Powder X-Ray Diffraction patterns of PbS embedded and not embedded $CsPbBr_3$ compared to the ICSD standard.

The room temperature powder X-Ray Diffraction patterns for $CsPbBr_3$ and PbS embedded $CsPbBr_3$, compared to an ICSD standard shown in Fig. 4.3 The synthesized samples crystallize in the expected orthorhombic phase with a space group Pnma. Signatures from PbS are not expected to be visible in the XRD pattern due to a combination of both low phase percentage and peak broadness associated with its nanoscale domains. The RL and SANS measurement results for these phase-confirmed samples will be presented in the next section.

4.2.2 Radioluminescence Measurements

When X-Ray is incident on the PbS embedded $CsPbBr_3$, they emit radiation in the near-infrared range, indicating transfer of energy from $CsPbBr_3$ to PbS QD. In the previous studies of PbS embedded $MAPbBr_3$, the RL peak position was previously shown to be dependent on the QD loading percentage ranging from a redshift, relative to the 830 nm excited oleate QD PL, of 63 meV at 1 wt% PbS loading to a blue shift of 34 meV at 0.01 wt% loading [35]. Similarly, in PbS embedded $CsPbBr_3$ (Fig. 4.4(A)), a redshift up to 63 meV at 2 wt% PbS and a blueshifts down to 123 meV at 0.05 wt% PbS is observed.

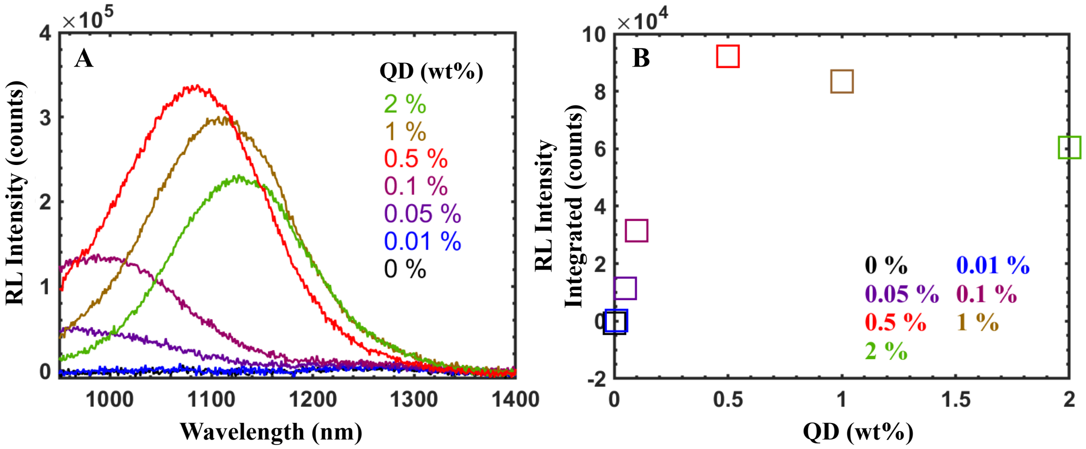

Figure 4.4: RL intensity (A) and RL integrated intensity (B) of PbS embedded $CsPbBr_3$.

It is interesting to note the integrated RL intensity (Fig. 4.4(B)), which gives an indication of luminescence or brightness (count of emitted photons), increases from 0.01 wt% up to 0.5 wt% after which it starts to decrease. This is similar to the previous observation made on PbS embedded $MAPbBr_3$ where maximum RL intensity is observed at an intermediate QD loading (0.1 wt%), after which it decreases. This could be due to the interplay of a decrease in spatial separation between QDs, resulting in the reabsorption of emitted photons, and an increase in the number of QDs, resulting in increased emission sites. The trade-off between these two processes could result in an optimal value at which the scintillator brightness is the maximum. The details of how these QDs are distributed in the perovskite matrix will be discussed in the next section.

4.2.3 Spatial Distribution of Quantum Dots from SANS

We performed SANS on the parent system $CsPbBr_3$ and six different PbS QD loadings on $CsPbBr_3$. The raw SANS data (Fig. 4.5) can be divided into three regions: Region I corresponds to length scales greater than 20 nm, Region II spans between 1 nm and 20 nm, and Region III covers scales below 1 nm. Region III typically corresponds to the length scale probed by neutron diffraction and inelastic neutron scattering, where one can investigate atomic-scale features like the unit cell and scattering from different lattice planes. This region is generally not resolvable in a SANS experiment, as the incident neutron wavelength is designed to probe larger real-space distances between particles.

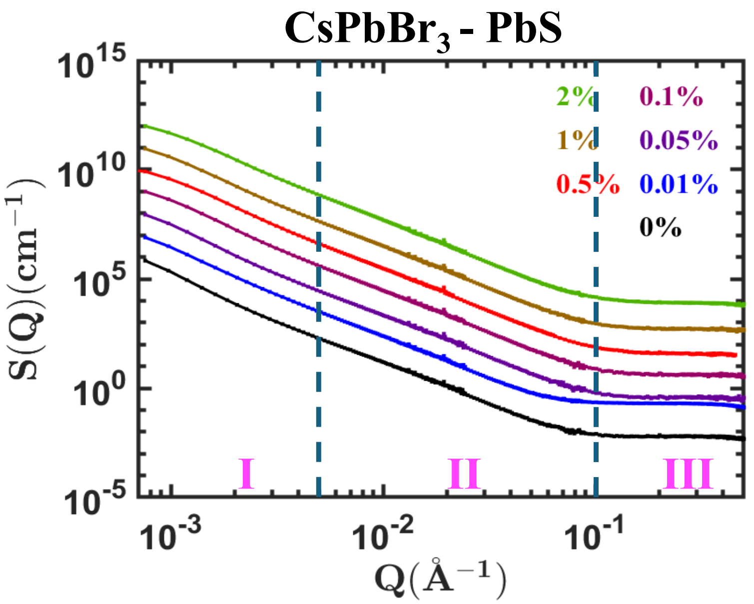

Figure 4.5: SANS measurements of PbS embedded $CsPbBr_3$ with six different QD loadings (QD = 0.01%, 0.05%, 0.1%, 0.5%, 1%, 2%). Each measurement was offset from the lower concentration measurement by a factor of 10.

In reciprocal space, $Q = \frac{2\pi}{d}$, where d is the characteristic length scale. For large distances in the system and with a large detector-to-sample distance, the small-angle approximation $Q \sim \frac{1}{d}$ holds. We focus on analyzing Regions I and II based on the small angle approximation. Region II exhibits a logarithmic slope scaling with Q^{-4}, which results from scattering off macroscopic particles or perovskite domains. In Region I, the slope decreases, which is believed to be due to scattering from the embedded PbS QDs, which varies depending on the PbS concentration. To better observe the changes in Region I, we plot its derivative.

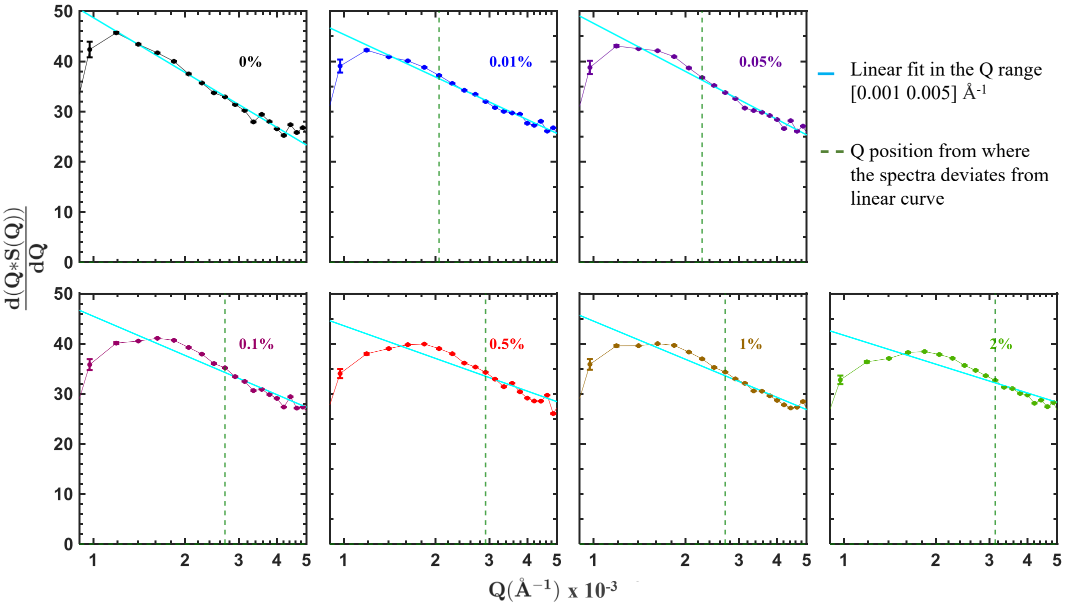

Figure 4.6: First derivative of the intensity of SANS spectra with respect to Q for various QD loadings on $CsPbBr_3$. The blue line represents a linear fit in the Q range [0.001, 0.005] $Å^{-1}$. The green dashed line represents the point in Q (Q_C) from which the spectra deviate from the linear fit.

From the derivative plot (Fig. 4.6), we observe that when no QDs are present, the curve appears linear. However, upon introducing QDs (QD 0.1 wt%), a plateau-like region emerges, deviating from the linear trend. By performing a linear fit, we identify a crossover point, Q_c, which marks the point where the scattering intensity deviates from the linear curve. By taking the reciprocal of Q_c we obtain the real space distance corresponding to the crossover region. Figure 4.7 presents a comparative analysis of $1/Q_c$ with the calculated inter-QD distance* based on a uniformly distributed array of 3.1 nm PbS QDs in a $CsPbBr_3$ matrix using bulk densities to convert from a wt% to a volume% (Appendix E). Upon comparing the calculated distance between QDs and the inverse of Q_c obtained from the experimental analysis, we observe that both

---

*The calculations of inter-QD distance was performed in collaboration with Dr. Grayson C Johnson from the department of Chemical Engineering.

these values are of the same order, varying between 10 nm and 90 nm. Both $1/Q_c$ and calculated distance between QDs gradually decrease with an increase in QD loading percentages, with no huge change above 0.5%. That these values are not significantly reduced suggests against PbS particle aggregation in the matrix. Our analysis on PbS loaded $CsPbBr_3$ systems concludes that SANS measurement could provide an estimation of the distance between QDs and, thus, how QDs are distributed in the perovskite matrix.

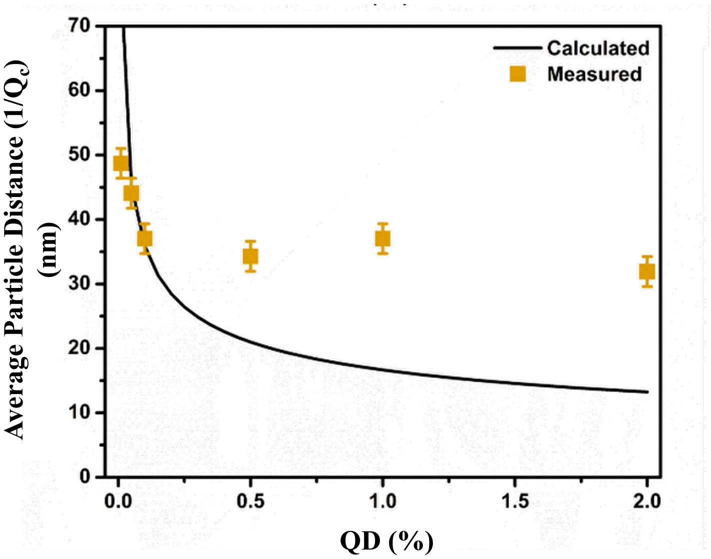

Figure 4.7: Comparison of the calculated average particle distance assuming an isotropic distribution of particles to the average particle distance determined from the SANS data.

4.3 Discussions & Conclusions

The experimentally determined average particle distance tends to saturate at PbS concentrations above 0.5%. The calculated values for QD separation were obtained, assuming a uniform distribution of QDs within the perovskite matrix. Therefore, the deviation observed in the experimental average particle distance at higher loadings likely suggests an inhomogeneous distribution of PbS QDs, with some QDs positioned closer together while others are farther apart. This inhomogeneous distribution could also explain the decrease in radioluminescence intensity observed beyond 0.5%. The proximity of certain QDs may lead to photon reabsorption, while the increased number of QDs still allows for sufficient emission.

Our previous study on Yb-doped $CsPbCl_3$ revealed an inhomogeneous distribution of Yb within the perovskite matrix, as demonstrated by Scanning Electron Microscopy coupled with Energy Dispersive X-ray Spectroscopy (SEM-EDS) mapping. It would be valuable to perform a similar SEM-EDS mapping analysis on PbS-embedded $CsPbCl_3$ to confirm the spatial distribution of the QDs. Future work should focus on optimizing the synthesis method to achieve a more homogeneous incorporation of PbS into the perovskite matrix.

This study highlights that the light yield and scintillator brightness are very sensitive to the spatial distribution of QDs. Controlling the QD distribution to achieve a homogeneous or inhomogeneous arrangement could result in a wide range of scintillator materials, with performance tailored to meet specific application requirements.

4.4 Summary

In this chapter, we discussed our work on fully inorganic PbS quantum dot (QD) embedded $CsPbBr_3$ perovskite scintillators. X-ray diffraction confirmed that the sample crystallized in the orthorhombic phase as expected. Using Small Angle Neutron Scattering (SANS), we quantified the spatial distribution of QDs within the perovskite matrix and proposed a possible mechanism for how it affects the radioluminescence emission intensity. Our findings suggest that controlling the spatial distribution of QDs offers a way to tune the scintillation properties of materials.

Chapter 5

Lattice Dynamics of 3D HOIP Single Crystals

Metal Halide Perovskites have achieved striking success as low-cost photovoltaic [7,8] and light-emitting device materials [10,11]. Among them, $MAPbBr_3$ and $FAPbBr_3$ are two widely studied 3D Hybrid Organic-Inorganic Perovskites (HOIP) due to their highly dynamic nature, resulting from strong structural disorder, reorientation of the organic molecules, polaron formation from the rotation of organic molecules and optical phonons, and diffusion of organic cations and halide ions [79,151,152]. Due to these phenomena, efforts to explain the optoelectronic properties of these materials based on their long-range structure alone fall short. Therefore, it is crucial to focus on short-range order interactions that have been shown to significantly affect their physical properties. For example, previous studies have shown that in $MAPbBr_3$, as the system transitions from a state of lower rotational entropy of organic molecules to a state of higher rotational entropy, the lifetime of the charge carrier increases [127]. Additionally, polaron formation due to interactions between charge carriers and optical phonons has shown to prolong the charge carrier lifetime by shielding the carriers from defects and phonon scattering [89]. Another critical factor influencing charge carrier lifetime is acoustic phonon scattering. The "melting" of acoustic phonons at higher temperatures has shown to enhance charge carrier lifetimes by minimizing energy loss through acoustic phonon scattering [90]. Thus, the properties of MHPs can be fine-tuned based on the interplay between phonon dynamics, polaron formation, and structural reorientation under external factors such as temperature, pressure, and doping.

A recent study of inelastic neutron scattering on the purely inorganic $CsPbBr_3$ revealed the overdamping of transverse acoustic (TA) phonons along the path $\Gamma-\mathrm{M}-\mathrm{R}-\Gamma$ in both tetragonal and cubic phases (Fig. 5.1) [95]. The low-energy modes along

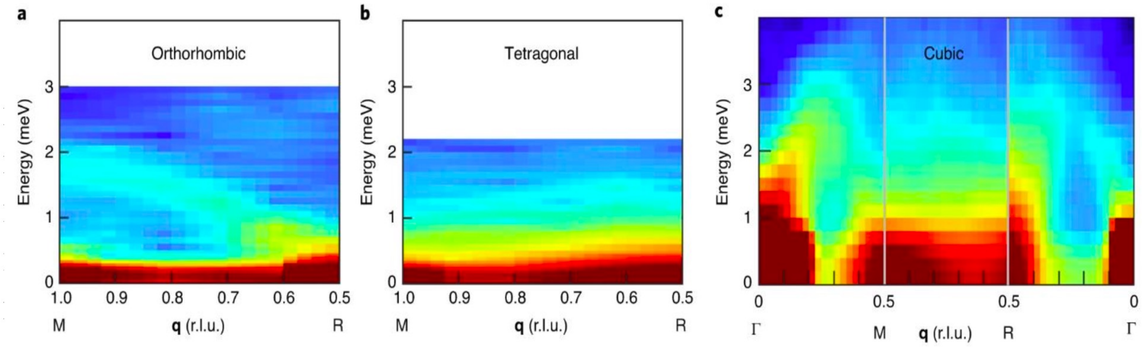

Figure 5.1: Acoustic phonons of $CsPbBr_3$ along the Γ–M–R–Γ direction in the three structural phases, i.e. orthorhombic ($T < 361$ K), tetragonal ($361 \text{ K} < T < 400$ K), and cubic phase ($T > 400$ K) observed from inelastic neutron scattering. The figure is extracted from Ref [95], measured at CNCS (Cold Neutron Chopper Spectrometer) at Oak Ridge National Lab.

this direction were dominated by Br-Br motions. If phonon overdamping leads to excessive lattice disorder, such as increased halide ion diffusion or dynamic structural instabilities, it can introduce defects or scattering centers that promote non-radiative recombination. Specifically, the anharmonic Br-Br motion from phonon overdamping along the M-R direction in $CsPbBr_3$ induces local lattice disorder, which facilitates the loss of charge carrier energy through electron-phonon scattering, thereby reducing charge carrier lifetime. This local disorder is particularly detrimental to device performance. Additionally, halide ion diffusion contributes to structural instability, further undermining the long-term stability of the devices [153]. As $MAPbX_3$ (X=Cl,Br,I) continues its journey towards commercial solar applications, particularly in tandem solar cells, it is crucial to understand how phonon dynamics evolve along specific crystallographic directions. This understanding will help us fine-tune the material's properties to minimize detrimental effects on device performance, such as increased non-radiative recombination or instability.

In this project, we performed temperature-dependent and orientation-dependent X-Ray diffuse scattering (XDS) and inelastic neutron scattering (INS) on a single crystal of $MAPbBr_3$ to study the behavior of low-energy phonons in the orthorhombic, tetragonal, and cubic phases. Based on our measurements, we found phonon overdamping in the M-R direction, similar to what was reported for $CsPbBr_3$. Additionally, we observed diffuse signals along the X-M direction in all three structural phases, likely arising from transverse acoustic phonons in the Γ-X-M-Γ direction as observed from INS. Similar to the observations made on $MAPbI_3$ by Chen et al [127] we observe $MAPbBr_3$ transitioning from lower molecular rotational entropy to higher molecular rotational entropy during structural change from orthorhombic to tetragonal and cubic phase. Diffuse signal from these rotational modes cannot be observed in XDS, as it is not sensitive to lighter atoms like H, C and N, but visible in INS in the quasi-elastic region. Based on density functional theory (DFT) calculations of these materials from the literature [94], these low-energy acoustic phonons primarily involve vibrations of the inorganic layers, particularly Br-Br motions. But in contrast to the completely inorganic $CsPbBr_3$, the phonon overdamping in the M-R and X-M direction might have indirect influence from molecular rotation and organic cation diffusion. This was evident from the increased neutron incoherent scattering background in the tetragonal and cubic phases. Our study suggest that for 3D HOIPs understanding the interplay of ion diffusion, molecular rotation and phonon vibrations are important to understand the possible effects on charge carrier lifetime. Minimizing the impact of ion diffusion and enhancing polaron formation from molecular rotation is essential for improving the performance and stability. Our study highlights the importance of understanding various atomic motions in HOIPs to optimize their performance in photovoltaic and light-emitting devices.

5.1 Experimental Details

The single crystals of $MAPbBr_3$ were synthesized in-house at the Department of Physics, University of Virginia (synthesis details provided in Appendix A). X-Ray diffuse scattering (XDS) measurements were performed at beamline BL02B1 [154] with an incident energy of 40 keV at SPring-8 (Super Photon Ring, 8 GeV), Japan, with an instrument resolution of $\sim 0.02, \text{Å}$. The collected XDS data were analyzed using the software CrysAlisPro [155]. Inelastic neutron scattering (INS) was carried out using the Cold Neutron Chopper Spectrometer (CNCS) at Oak Ridge National Laboratory [156], with an incident energy of 6.95 meV and an energy resolution of 0.25 meV. The collected INS data was processed using the software Shiver [157] and Mantid [158].

5.2 Results and Analysis

5.2.1 Phonon dynamics from X-Ray Diffuse Scattering

As mentioned in Chapter 2.1.4, when a system contains local disorder or thermal vibrations (phonons), the X-ray diffuse scattering (XDS) will exhibit diffuse intensities away from the Bragg peaks. These patterns can appear as continuous streaks or scattering rods. To investigate the phonon dynamics across different structural phases of $\mathrm{MAPbBr_3}$, we performed XDS at three temperatures corresponding to its phases: 100 K for orthorhombic ($T < 145$ K), 200 K for tetragonal ($145 < T < 210$ K), and 300 K for cubic ($T > 210$ K).

If the Brillouin zone (BZ) center point, Γ has a wavevector $Q = (H, K, L)$, the X point is at $Q = (H + 0.5, K, L)$, the M point is at $Q = (H + 0.5, K + 0.5, L)$, and the R point is at $Q = (H + 0.5, K + 0.5, L + 0.5)$. A schematic of the high-symmetry directions in a typical cubic structure is shown in Fig. 5.2.

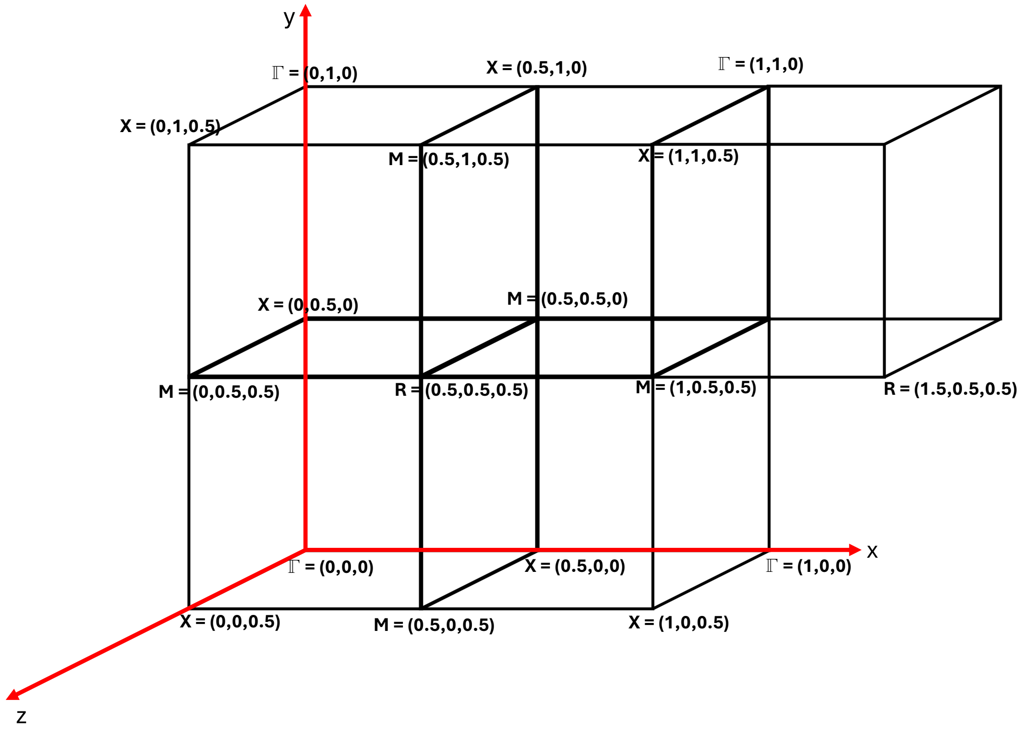

Figure 5.2: High-symmetry points in a simple cubic Brillouin Zone (BZ).

Since it is challenging to visualize the thermal diffuse patterns for $(H, K, L) = (H, K, 0)$ due to the presence of strong Bragg scattering, we focus on $(H, K, L) = (H, K, 0.5)$ (Fig. 5.3). We observe diffuse patterns or cylindrical rods along the M-R direction for both the tetragonal and cubic phases and not in the orthorhombic phase (red dashed lines in Fig. 5.3 (D, E, F)). This is similar to the previous observations made for $\mathrm{CsPbBr_3}$ [95], which is shown in Fig. 5.3(A, B, C). Additionally, the R point becomes a Bragg peak in the tetragonal and orthorhombic phases. Many superlattice peaks emerge during the tetragonal to orthorhombic phase transition, which was unexpected. This could be due to lattice distortion associated with rapid cooling of

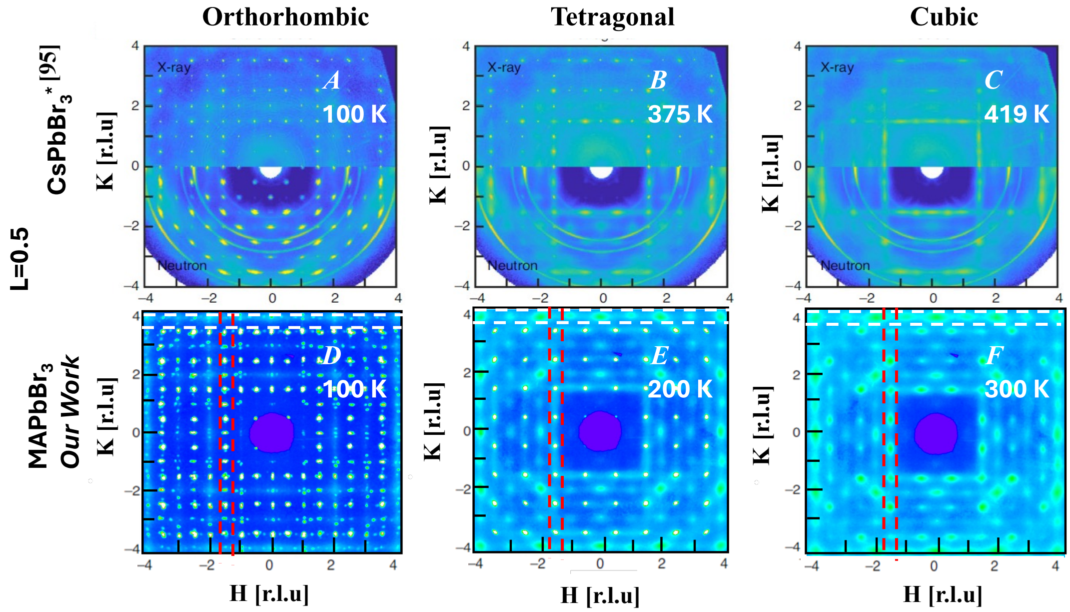

Figure 5.3: Temperature dependent X-Ray diffuse scattering of $CsPbBr_3$ (A, B, C) extracted from literature [95]* and $MAPbBr_3$ (D, E, F) (our work) in the L=0.5 plane. The white dashed line represents the X-M direction along Q=(H, 4, 0.5), and the red dashed lines represent the M-R direction along Q=(-1.5, K, 0.5).

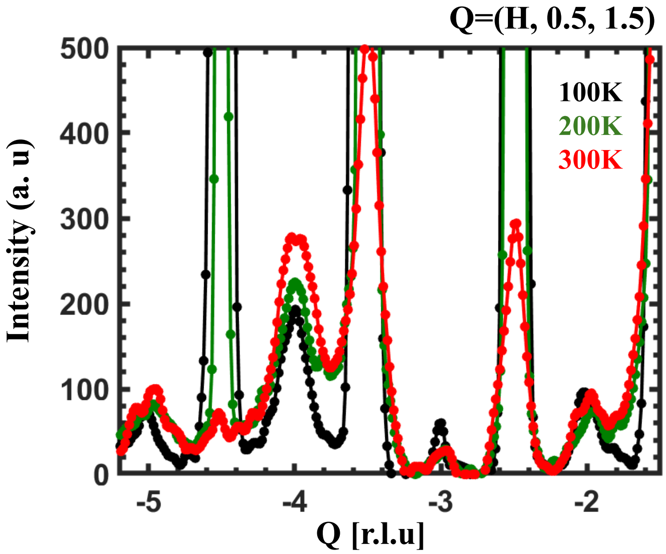

Figure 5.4: Temperature dependent X-Ray diffuse scattering of $MAPbBr_3$ along the M-R direction (Q=(H, 0.5, 1.5)).

the samples, which results in incommensurate modulation of the lattice. A depiction

---

*T. Lanigan-Atkins et al.,Nature Materials, vol. 20, no. 7, pp. 977–983, 2021.

of the emergence of these superlattice peaks at the orthorhombic phase along the M-R direction is shown in Fig. 5.4. All M points ((H, 0.5, 1.5), for integer H) show a similar trend with temperature in the cubic and tetragonal phases. In contrast the orthorhombic phase shows different behavior at different M points. The scattered intensity at the M point is narrow at (-3, 0.5, 1.5), compared to the tetragonal phase, whereas at (-4, 0.5, 1.5), it is broader, similar to the higher temperature phases. Thus, a quantified spectral broadening from phonons will be more reliable in the tetragonal and cubic phases. In addition to the diffuse rods in the M-R direction, we also observed diffuse rods along the X-M direction for all three structural phases (white dashed lines in Fig. 5.3 (D, E, F)) similar to the previous observations made for $CsPbBr_3$ [95] (Fig. 5.3 (A, B, C)).

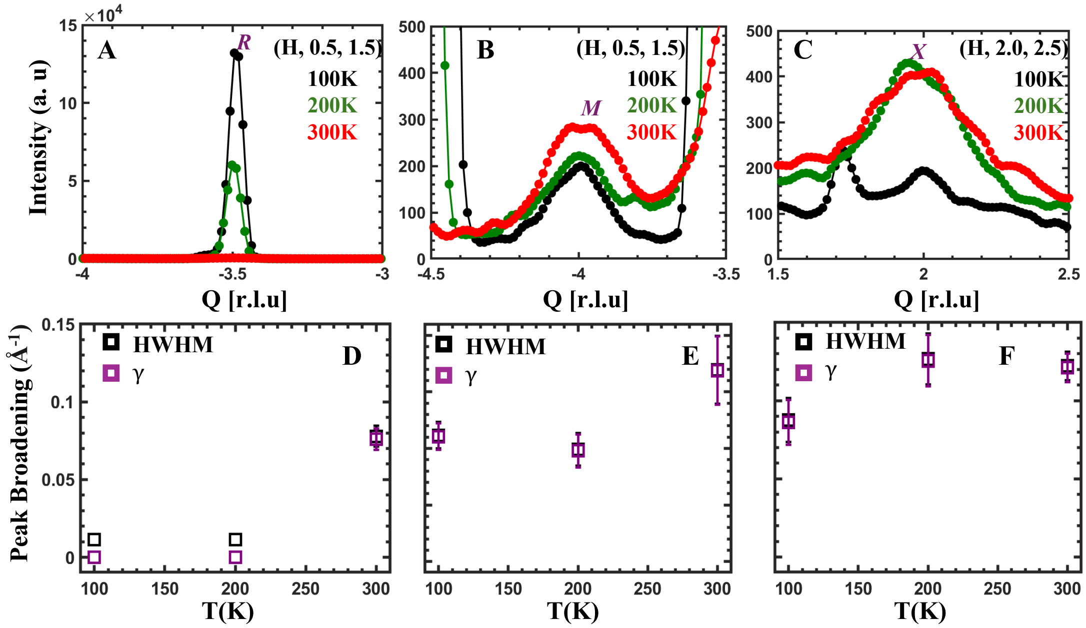

Figure 5.5: Temperature dependent X-Ray diffuse scattering of $MAPbBr_3$ at (A) R point, (B) M point and (C) X point along with their HWHM and Lorentzian broadening (γ) obtained from Voigt fit in D, E and F respectively.

To see how the diffuse signal changes with temperature, we performed a Voigt fit, convoluting the Lorentzian function based on Ornstein-Zernike theory, as mentioned in Chapter 2.1.4, with a Gaussian function representing the instrument resolution (see Appendix F for various temperature fitted curves). A sudden discontinuous jump towards reduced spectral broadening is observed at the R point (Fig. 5.5(A)) as the system transitions from the cubic to the tetragonal phase. This occurs because the R point becomes the Γ point in the tetragonal phase, thus producing Bragg scattering. Furthermore, the point R is also a Γ point in the orthorhombic phase.

Thus, at the orthorhombic and tetragonal phase, the Gaussian function (instrumental resolution function) was enough to explain the spectral shape and spectral width (HWHM), resulting in a negligible Lorentzian broadening (γ) (Fig. 5.5(D)). But as the system transitions to the cubic phase, the R point becomes diffuse rods, and thus γ contributes significantly to the HWHM.

A perfect crystal with no local lattice disorder or phonon overdamping should not result in any scattered intensity in the M and X points as these are not Γ points. However, we observe diffuse intensities at both the M and X points, suggesting a local disorder, which might be coming from phonons. The HWHM shows significant contributions from the Lorentzian part γ for both M and X points (Fig. 5.5(E)(F)). The diffuse signal is stronger at the M point for the cubic phase in the M-R direction (Fig. 5.5 (B)), while the X point shows diffuse intensity in all three phases, with a broader diffuse signal in the tetragonal and cubic phases (Fig. 5.5 (C)). This suggest the presence of phonon overdamping in the X-M direction at both tetragonal and cubic phases, and phonon overdamping in the M-R direction in the cubic phase. It is important to note that γ does not vary much from the orthorhombic phase to the tetragonal phase at the M point, suggesting the non-reliable fitting of the orthorhombic phase due to the superlattice peaks.

Based on the γ values extracted from the fit, we plot its reciprocal, which is the correlation length (ξ) (Fig. 5.6). As mentioned, the ξ obtained in the orthorhombic phase might not be exact due to superlattice peaks. The correlation length obtained

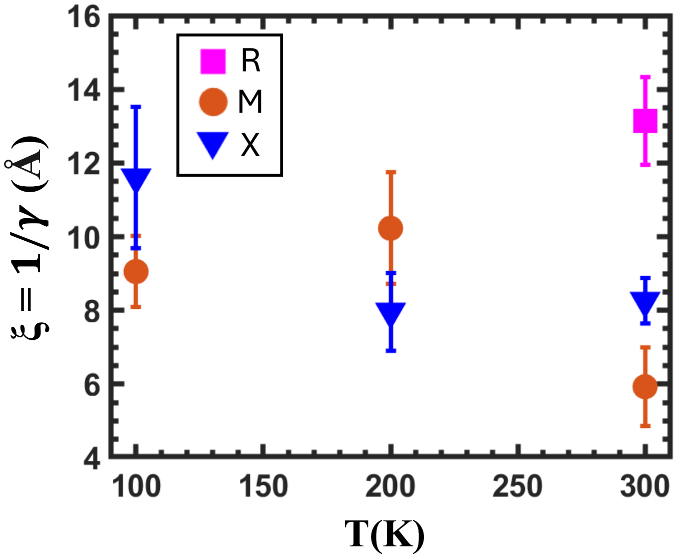

Figure 5.6: Correlation length (ξ) from X-Ray diffuse scattering of $MAPbBr_3$ at X (blue triangles), M (orange squares) and R (magenta circles) points.

for R points at 300 K (13(1) Å) and M points at 300 K (6(2) Å) and 200 K (10(2) Å) are close to the reported correlation length of 19(2) Å for R points and 10(2) Å for M points in the literature for the same system at 250 K [94]. Interestingly the correlation length for X points lies approximately in the same range as M.

From XDS measurements, we found scattering rods across the M-R direction in the cubic phase and in the X-M direction in all three structural phases with much broader diffuse signals in the tetragonal and cubic phase. To understand what types of phonon could be causing these diffuse signals, we analyzed the inelastic neutron scattering (INS) data, which will be discussed in the next section.

5.2.2 Phonon and Rotational Dynamics from Inelastic Neutron Scattering

We performed INS on two aligned single crystals of $MAPbBr_3$, each with approximate dimensions of $0.5\times0.5\times0.2cm^3$. Unlike X-ray scattering, which typically requires crystals of sizes less than $0.1\times0.1\times0.1cm^3$, neutron scattering requires a comparably larger size and amount of sample due to the lower scattering cross section of neutrons. We used an incident energy of 6.95 meV to analyze the low-energy phonons.

We carefully looked into the BZ directions Γ-X-M-Γ (Fig. 5.7) and the M-R directions (Fig. 5.8). The Γ-X path corresponds to [H, 2, 0] for $-0.5 < H < 0$, X-M path corresponds to [-0.5, 2.0, H] for $0 < H < 0.5$ and Γ-M path corresponds to [-H, 2, H] for $0 < H < 0.5$. The M-R path corresponds to [-0.5, K, 0.5] for $1.5 < K < 2$. Since the transverse acoustic (TA) phonons in the completely inorganic $CsPbBr_3$ underwent overdamping during structural phase transitions [95], here we are trying to probe similar effects in $MAPbBr_3$. Thus, all the BZ paths were chosen so that we could investigate the phonons in the transverse direction.

TA phonons between 2 meV and 5 meV along Γ -X and Γ -M have been identified and analyzed in many neutron and X-ray scattering studies on $MAPbX_3$ (X=Br, I, Cl), and our study confirmed the same [54, 94, 159–161]. Acoustic phonons (in phase atomic vibrations) tend to follow a linear dispersion at small wavevectors (k) following the relation $\omega \propto$ k starting from the Γ point [162]. They tend to flatten out as they approach the zone boundaries (X and M points with higher values of k). We identify these low-energy TA phonons at $\sim$ 3 meV at X and M points to extend towards each other in the X-M direction.

Optical phonons differ from acoustic phonons because they have a non-zero energy at the Γ point. We observe a weak branch of the phonon at $\sim$ 4.9 meV in the X-M direction, and based on how it extends to the M-Γ direction, we identify it as

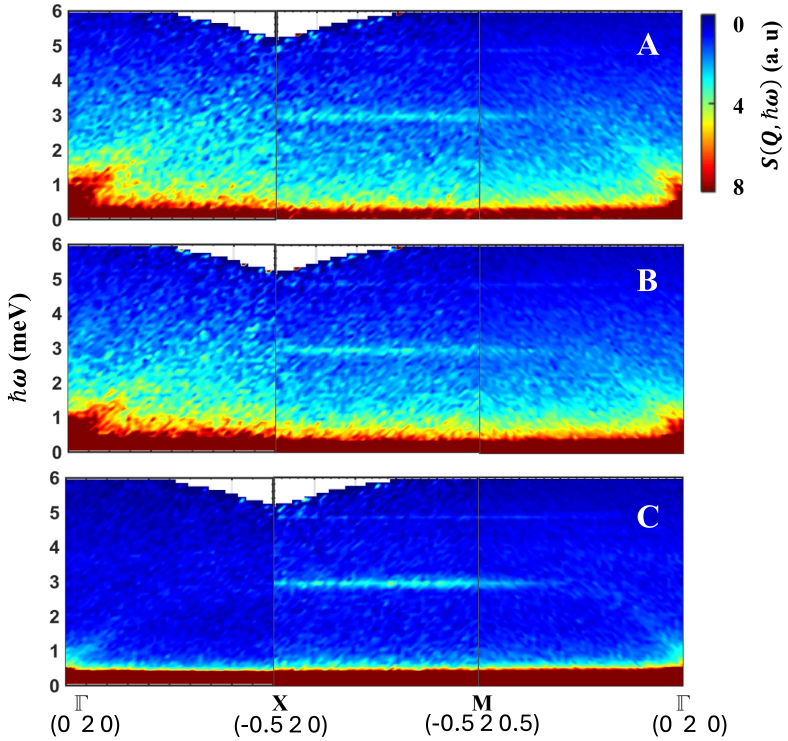

Figure 5.7: Temperature dependent INS spectra of $MAPbBr_3$ along the BZ direction Γ-X-M-Γ: cubic phase (A) ($T = 300$ K), tetragonal (B) ($T = 200$ K), and orthorhombic (C) ($T = 80$ K). The Γ-X path corresponds to [H, 2, 0] for $-0.5 < H < 0$, X-M path corresponds to [-0.5, 2, H] for $0 < H < 0.5$ and Γ-M path corresponds to [-H, 2, H] for $0 < H < 0.5$.

a Transverse Optical (TO) phonon. The weak intensities of this phonon branch, along with the strong incoherent scattering background from hydrogen, make their quantitative analysis difficult [126, 127].

The phonon signals are also weak along the M-R direction. Based on previous literature studies [95, 163, 164], we expected TA phonons in the M-R direction in the tetragonal and orthorhombic phases (since the R points become a Γ point), and overdamped phonon signals in the cubic phase. However, apart from the acoustic phonons at the M point, we do not see any apparent phonon intensities towards the R point. Compared to the visible and robust acoustic phonon signals in the X-M direction, the M-R direction might have a feeble, low-energy signal as we move toward R. The possibility of a low intense phonon signal in the M-R direction, along with the strong neutron-incoherent scattering background of hydrogen, might be limiting their clear capture.

Studies on $MAPbI_3$ have shown that when the system transitions from orthorhom-

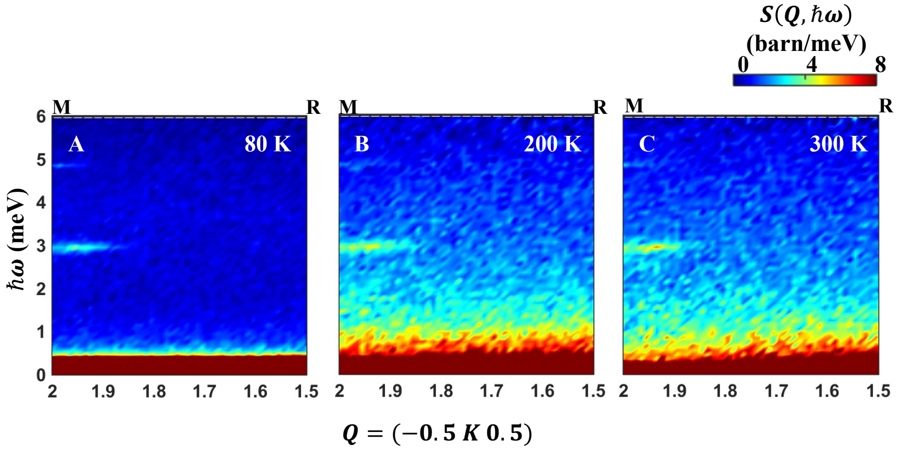

Figure 5.8: Temperature dependent INS spectra of $MAPbBr_3$ along the BZ direction M-R: orthorhombic (A) (T = 80 K), tetragonal (B) (T = 200 K), and cubic phase (C) (T = 300 K). The M-R path corresponds to [-0.5, K, 0.5] for $1.5 < K < 2$. All the BZ paths are chosen so that we can measure the transverse acoustic or optical phonons.

bic to tetragonal and cubic phase, additional rotational modes on the organic molecule get activated, thus increasing the incoherent scattering background [127]. Rotations manifest themselves as diffusion of the elastic channel intensity in the low-energy inelastic region [102]. A more dynamic rotation increases the diffusion, thus broadening the elastic channel intensity. Therefore, it is essential to study the quasi-elastic region ([0.3, 1] meV) of the INS data for the bromide equivalent of $MAPbI_3$.

To understand how the phonon and rotational dynamics vary with temperature along the X-M and M-R direction, we performed Voigt fit at the X, M, and R points. These points were selected for the convenience of a future comparison with the results from XDS measurements (Refer Appendix G for various temperature fitted curves). As mentioned, the Voigt function is the convolution of the Gaussian (instrument resolution) and the Lorentzian function (spectral broadening). We perform Q (momentum space) cuts to isolate the X, M, and R points and quantify how the phonon spectrum with respect to energy varies with temperature. Based on the uncertainity principle, the lifetime for a phonon centered around its normal mode energy can be calculated using the relation $\hbar/\gamma$, where γ is the lorentzian width. Similarly, the average lifetime of molecular rotation can be calculated from the γ obtained by fitting the quasi-elastic region using a voigt function centered around zero energy.

Similar to our observations from XDS, the R point becomes a Γ point in the tetragonal and orthorhombic phase (Fig. 5.9(A)). Thus, the instrument resolution function could explain the spectral shape well. Although we expected a significant

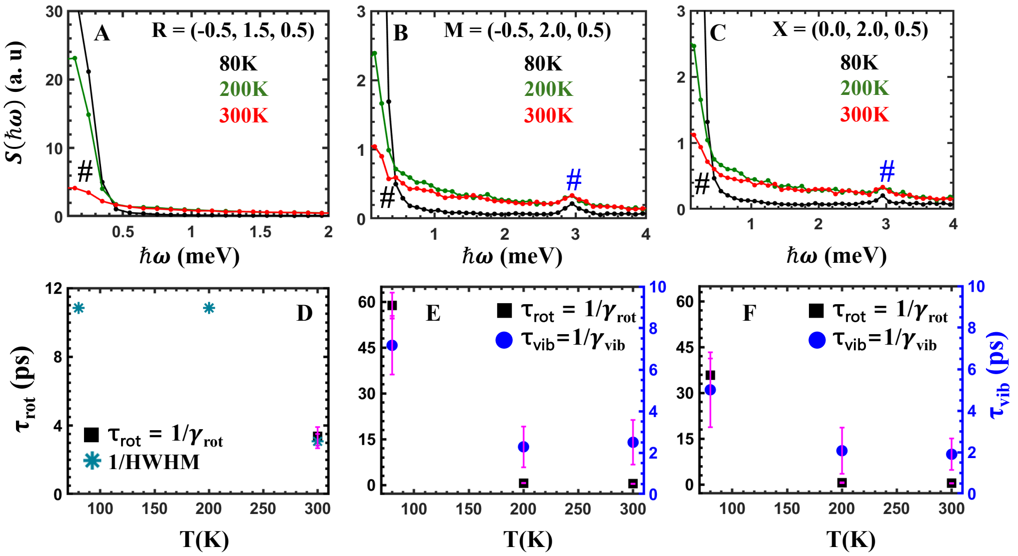

Figure 5.9: Panel A, B and C represent the scattered intensity (S($\hbar\omega$)) for R, M and X points respectively. These points were selected for the convenience of a future comparison with the results from XDS measurements. The chosen Q integration range was K=[1.4, 1.6] Å^{-1} in the path [-0.5, K, 0.5] for R point, H=[-0.55, -0.45] Å^{-1} in the path [H, 2, 0.5] for M point and H=[-0.05, 0.05] Å^{-1} in the path [H, 2, 0.5] for X point. The blue # symbol represent the phonon peak and black # symbol represent the rotational intensity in the quasi-elastic region. Panels C, D and E represent the obtained lifetime for phonons (τ_{rot}, blue circles) and molecular rotations (τ_{rot}, black squares) in the R, M and X points respectively based on Voigt fit. Refer Appendix G for various temperature fitted curves. We are only plotting the lifetime of molecular rotations in the cubic phase for R point (D), as it is a Γ point in the tetragonal and cubic phase resulting in bragg scattering. Furthermore any phonons present are very weak making it non-resolvable. To showcase how the R point elastic channel intensity broadens when system transitions to cubic phase we plot the inverse of HWHM which has only contributions from the instrument resolution at the low temperature phases.

broadening of the elastic channel intensity in the tetragonal phase due to rotational dynamics, the strong Bragg scattering at the R point made it appear less prominent. However, we observed significant contributions from rotational dynamics in the quasi-elastic region for the R point at the cubic phase and the M (Fig. 5.9(B)) and X point (Fig. 5.9(C)) at the tetragonal and cubic phase. The average lifetime of molecular rotations (τ_{rot}) in the tetragonal and cubic phase at the X and M points is approximately 0.5 ps, indicating both strong rotational dynamics and organic cation diffusion. τ_{rot} observed for the R point in the cubic phase is approximately 3 ps.

Based on a previous study [127], we expected an average lifetime of less than 1 ps for rotational modes. Therefore, we suggest that some weak, broad energy phonons could be present at the R point, which is not resolvable from our INS measurements. This could result in an over-fitting of the molecular rotations in the quasi-elastic region for the R point, thus showing an average rotational lifetime higher than X and M points. It is important to note that we are not expecting the molecular rotation, which is incoherent, to change with different BZ directions.

Acoustic phonons at X and M points tend to have a shorter phonon lifetime (τ_{vib}) in the tetragonal and cubic phases compared to the orthorhombic phase. An increased phonon occupation upon warming can increase the phonon-phonon scattering process, leading to an enhanced anharmonic reaction. This, in turn, results in faster energy dissipation and reduced phonon lifetime. However, rather than a continuous decrease in phonon lifetime throughout warming, the phonon lifetime from our experiment shows similar values in the tetragonal and cubic phases and a sudden increase in the orthorhombic phase. This might suggest TA phonon overdamping in the tetragonal and cubic phases. A comparison of how TA phonons contribute to the diffuse signals observed in XDS is necessary to complete the bigger picture of the phonon dynamics in MAPbBr_3 and how it can be detrimental to the performance of these materials in functional devices.

5.2.3 Discussions & Conclusions

In this work, to compare the temperature dependence of the phonons, we choose to evaluate the correlation length from XDS and the lifetime of the phonon from INS (Table. 5.1). The correlation length from XDS will give an idea of the nature of the interaction, whether long-range or short-range, and how spatially correlated the interactions are. If the phonon interactions are long-range and correlated over large distances, we expect the phonon to dissipate its energy slowly and thus increase the phonon lifetime. If the phonon gets overdamped in specific directions, resulting in local disorder in the system, the interactions will be short-range and correlated over short distances, thus quicker dissipation of energy and reduced phonon lifetime. Due to the superlattice peaks in the orthorhombic phase, we compare the phonon lifetime and correlation length in the tetragonal and cubic phases.

For both X and M points, the phonon lifetimes did not show much variation as the system transitioned from tetragonal to cubic phase; similarly, the correlation length obtained from the XDS diffuse rods did not show significant change. Interestingly, our work also shows that the X point behaves similarly to the M point. This indicates that the diffuse rods observed in the X and M points from XDS correspond to the

Table 5.1: Correlation length (ξ) measured from XDS and phonon (τ_{vib}) and moleular rotation (τ_{rot}) lifetime measured from INS of $MAPbBr_3$ at selected BZ edges for the different structural phases.

T(K)	$\varepsilon = 1/\gamma$ (Å)		τ_{vib} (ps)		τ_{rot} (ps)		
	Diffuse Rods		Phonons		Molecular Rotation		
	X	M	X	M	X	M	R
100	-	-	5(2)	7(1)	36(5)	59(4)	-
200	8(1)	10(2)	2(1)	2(1)	0.6(1)	0.7(1)	-
300	8(1)	6(1)	2(1)	2(1)	0.5(1)	0.5(1)	3.1(4)

TA phonons in the X-M direction as observed from INS. Additionally, as previously observed from Fig. 5.6, the diffuse rods at R point have a larger spatial correlation in the cubic phase than those at M and X points. The correlation length from XDS corresponds to the correlation in the $PbBr_3$ as signals from lighter atoms like C, N, and H are significantly weak. Instead, INS is very sensitive to H; hence, the molecular rotations could dramatically affect the observation of low-energy phonons. Molecular rotations tend to be more dynamic at cubic and tetragonal phases, evident from their lower lifetime compared to the phonon lifetime. Based on previous work from our group, we are expecting two intrinsic rotational modes for $MAPbBr_3$: a C_3 mode of the NH_3 and CH_3 groups in MA molecule at all the three structural phases and a C_4 mode of the entire MA molecule about the crystallographic c-axis which gets activated only at the tetragonal phase.

Based on DFT calculations performed in literature studies [94,95,163], we identify the overdamping of TA phonons found at M point likely arising from the Br-Br motions and in-plane octahedral tilting. It is important to note that the M point showed only slight variation in the diffuse rod intensity, correlation length, and phonon lifetime on cubic to tetragonal phase transition. Therefore, the TA phonon at the M point appears to be related to the tetragonal to the orthorhombic phase transition. In contrast, in completely inorganic $CsPbCl_3$ [165], the TA phonon condensation at the M point is associated with the cubic to the tetragonal phase transition. The overdamping of phonons along the X-M direction is so far less explored in the literature. Although the low-energy phonons in these materials are primarily dominated by the inorganic layer, as a next step, it is essential to understand what exact atomic motion corresponds to the overdamping of acoustic phonons in the X-M direction. Unlike in $CsPbBr_3$ [95], in $MAPbBr_3$, in addition to Br-Br ion diffusions and inplane octahedral tilting, organic cation diffusion and off-centering might also contribute to the overall behavior of low-energy phonons. Hence, the TA phonon overdamping in the X-M direction could also be an indirect effect of the molecular rotations. Due to the feeble almost nonresolvable phonon signals in the M-R direction we were not able to see phonon overdamping from INS, but the diffuse rods from XDS confirmed the presence of the same.

The halide ion diffusion and organic cation diffusion can have detrimental effects on the charge carrier lifetime of these systems by reducing the stability and incorporating defects. However, polaron formation from molecular rotation can enhance the charge carrier lifetime in these systems through dielectric screening. Thus, a closer inspection of the interplay of polaron formation, inorganic layer tilting, and ion diffusions on the charge carrier lifetime of HOIPs is necessary. Nevertheless, our study highlights the presence of molecular rotation and phonon overdamping along specific BZ directions in a 3D HOIP. Quantifying these rotational and phonon dynamics is necessary to understand their possible impact on the optoelectronic properties.

5.2.4 Summary

This chapter discussed our work on the structural dynamics of 3D HOIPs along different BZ directions for various structural phases. From a comparative study of X-Ray Diffuse Scattering and Inelastic Neutron Scattering, we identified and analyzed phonon overdamping along the X-M and M-R directions. Additionally, we observed enhanced rotational dynamics as the system transitioned from the orthorhombic to the tetragonal phases. Our findings suggest that the overall behavior of phonons in HOIPs can have an indirect influence from halide anions and organic cation diffusion, and molecular rotations. Thus, understanding the interplay of various types of atomic motions is necessary to understand its possible effect on optoelectronic properties.

Chapter 6

General Conclusion

In this thesis, we discussed the potential of Metal Halide Perovskites (MHPs) for Photovoltaic (PV) and Light-Emitting Device (LED) applications. A wide variety of MHPs can be generated, including fully inorganic perovskites and hybrid organic-inorganic perovskites (HOIPs). The highly dynamic nature of these systems stems from structural reorientations, phonon overdamping, molecular rotations, ion diffusion, and cation off-centering. The interplay of these interactions can be beneficial or detrimental to their performance depending upon the type of materials present, temperature, pressure, and doping. Much research focuses on their surface morphology, defects, recombination mechanism, etc. However, understanding the microscopic details of various structural dynamics is still incomplete. For a better picture of the MHPs, we used neutron and X-ray scattering techniques as a major tool, along with Raman scattering, photoluminescence, and radioluminescence measurements for confirmative and optoelectronic property studies under various temperatures and dopings.

Firstly, we reported a comparative study on two 2D HOIPs, $(BA)_2PbI_4$ and $(PEA)_2PbI_4$. The study aimed to understand how molecular rotations and lattice vibrations can affect the recombination mechanism in these systems. We used inelastic neutron scattering to probe the phonon dynamics along with Raman scattering for comparative analysis, quasi-elastic neutron scattering to understand the rotational dynamics, and photoluminescence measurements to understand the possible effects of phonon and molecular rotations on the recombination mechanism. Based on our analysis, we suggested that in these two 2D HOIPs, increasing temperature activates and enhances the rotational motion of polarized organic molecules and is inversely correlated to their non-radiative recombination rate. In contrast, the lattice vibrations did not exhibit a clear relationship. We thus proposed a scenario in which the rotational motion of polarized organic molecules might interfere with the dielectric environment surrounding confined excitons, potentially reducing the EBE or breaking the binding energy degeneracy, enhancing the non-radiative decay of charge carriers by phonon or defect scattering, thus reducing the charge carrier lifetime. A reduced charge carrier lifetime is generally detrimental to device performance. However, we recall that a low EBE is preferred for PV devices. Thus, 2D HOIPs, which have sufficient freedom for molecular rotation while maintaining minimal phonon scattering, will be optimal for PV device applications. On the other hand, a higher EBE is typically preferred for LEDs. Thus, 2D HOIPs with more restricted molecular rotations will be ideal for them. Furthermore, in contrast to 2D HOIPs, a more robust molecular rotation appears to extend the charge carrier lifetime (or reduce non-radiative recombination) in 3D HOIPs. Thus, the study is an ideal example of how the same structural dynamic can pose contrasting charge carrier dynamics under reduced dimensionality in the conduction.

Different from our previous study, in which temperature was the external condition, our subsequent study aimed at understanding the effect of doping on specific MHPs known for their scintillator properties. Particularly, we tried to understand how the spatial distribution of dopants in the perovskite matrix could impact their luminescence property. We performed small angle neutron scattering on six different PbS Quantum Dot (QD) loaded $CsPbBr_3$ (0%, 0.01%, 0.05% 0.1%, 0.5%, 1%, 2%) along with their radioluminescence (RL) measurements. The QD spatial distribution decreased, and RL intensity increased towards higher QD loading up to 0.5%, beyond which the spatial distribution did not show much change, and RL intensity began to decrease. An inhomogeneous distribution of QDs with closer QDs in some areas and farther apart in others is possible at higher QD loadings, resulting in an increased emitted photon reabsorption and reduced luminescence. Thus, understanding the interplay of distance between QDs, the number of QD emission sites, and QD reabsorption of photons is necessary to optimize the performance of scintillator materials tailored to meet specific application requirements. Although QD-loaded perovskites have achieved luminescence on par with conventional scintillators, challenges associated with structurally dynamic MHPs still exist in their industrial scaling. Controlling the spatial distribution of QDs offers a way to overcome any potential quenching of their efficiency from the perovskite matrix lattice dynamics.

The previous two studies focused on powder samples of MHPs, where information about any directional dependence is lost. Thus, we decided to explore single crystals of a 3D HOIP, which could have different lattice dynamics along different directions. We performed a comparative study using X-ray diffuse scattering and inelastic neutron scattering on $MAPbBr_3$ single crystals. Our analysis identified overdamping of transverse acoustic phonons along the specific Brillouin zone directions, M-R [H+0.5, K+0.5, L+δ] and X-M [H, K+0.5, L+δ], where Γ= [H, K, L], as the system transitioned from orthorhombic structural phase to tetragonal and cubic phases upon warming. Although these phonons are primarily dominated by atomic motions from the inorganic $PbBr_3$ layer, molecular rotation, and organic cation diffusion appear to indirectly affect their behavior and visualization in experiments. Our study reiterates the need for a more comprehensive analysis on the interplay of rotational and lattice dynamics, organic cation and halide anion diffusions, and its possible impacts on the efficiency of HOIPs in functional devices.

Overall, through the three different projects, we were able to contribute to the research efforts in the field of MHPs. We highlighted the importance of various scattering techniques, especially neutron scattering, and the kind of insights they can provide. A combination of studies on various crystal types (powder, thin films, single crystals, etc.) under varying external conditions like temperature, pressure, doping, and, more recently, magnetic fields could develop highly efficient MHPs for optoelectronic devices scalable for commercial use.

Appendix A

Synthesis Details

A.1 Synthesis of $(BA)_2PbI_4$ and $(PEA)_2PbI_4$

The synthesis of powdered 2D lead halide perovskites, specifically n-butylammonium lead iodide (BA_2PbI_4) and 2-phenylethylammonium lead iodide (PEA_2PbI_4), was carried out using a layered solution method [166]. First, 75 mg (0.16 mmol) of lead iodide (PbI_2) was dissolved in 3 mL of hydroiodic acid (HI). A slight excess of the appropriate amine (0.5 mL) was then added to 3 mL of methanol and layered over the lead iodide solution. This layered solution was sealed and allowed to sit undisturbed for a week to facilitate crystal growth. Following this period, the resulting crystals were rinsed, filtered with diethyl ether, and vacuum-dried. Crystals were crushed into fine powders for powder X-ray diffraction (XRD) measurements. Also, a slow cooling method was employed for crystal growth, where a mixture of 10 mL of HI, 2 mL of hypophosphorous acid (H_3PO_2), 2 mmol of PbI_2, and 4 mmol of the appropriate amine was heated to 120 °C to ensure complete dissolution. This solution was then cooled at a rate of 2 °C/min to promote the formation of single crystals, which were subsequently filtered with diethyl ether and vacuum-dried.

These samples were synthesized by Dr. Grayson C Johnson and Dr. Alexander Z Chen at the Department of Chemical Engineering, University of Virginia, through collaboration.

A.2 Synthesis of PbS Embedded $CsPbBr_3$

To synthesize the 3.1 nm PbS quantum dots (QDs), 2 mmol of lead(II) oxide (PbO) was added to 12.7 mL 1-octadecene (1-ODE) and 2.2 mL oleic acid (OAc) in a three-neck flask. The flask was degassed under vacuum at 120°C for at least 1 hour, allowing the PbO to dissolve. In a N_2-filled glovebox, a bis(trimethylsilyl) sulfide $(TMS)_2S$ solution was prepared by dissolving 210μL in 10 mL of 1-ODE. The degassed lead oleate solution was then placed under an Ar atmosphere, and the $(TMS)_2S$ solution was injected quickly. The reaction produced a black solution and progressed for 30 seconds before the reactor was removed from heat to cool naturally. The crude product was separated by precipitation with methyl acetate and centrifugation at 6000 RPM for 8 minutes. The resulting pellet was redispersed in hexanes, and the washing procedure was repeated once more. The final solution was stored in hexanes for future use.

$CsPbBr_3$ powder was synthesized according to a modified procedure from [167]. $PbBr_2$ (0.5 M in NMF) and CsBr (2.5 M in DI H_2O) were mixed in a 1:1 ratio to generate an orange $CsPbBr_3$ precipitate. The $CsPbBr_3$ powder was washed twice with 35 mL of isopropyl alcohol (IPA) and separated via centrifugation at 6000 RPM for 5 minutes each. The residual IPA was removed via vacuum drying. PbS QDs were doped into the powder by mixing the QDs into the $PbBr_2$ solution prior to precipitation. In a standard preparation of 0.2wt% QD in perovskite material, 69.6μL of oleate-capped PbS QDs in hexanes (25 mg/mL) were added to 3 mL of 0.5M$PbBr_2$ solution, forming two layers. The vial was shaken vigorously for 30 seconds, and the PbS QDs were observed to transfer from the hexane layer to the NMF layer, indicating successful ligand exchange. The hexanes were removed using a Pasteur pipette, and the solution was washed three times with 1 mL of hexanes. The brown $PbBr_2$/PbS/NMF solution was then precipitated with 600μL of 2.5 M CsBr as an orange-brown solid. The powder was washed and dried in the same manner as the undoped material.

These samples were synthesized by Dr. Grayson C Johnson at the Department of Chemical Engineering, University of Virginia, through collaboration.

A.3 Synthesis of single crystals of $MAPbBr_3$

We synthesized the single crystals of $MAPbBr_3$ using the vapor-assisted crystallization method [168]. Initially, 408 mg of methylammonium bromide (MABr) and 1.198 g of lead(II) bromide ($PbBr_2$) were accurately weighed and transferred into a glass vial. These precursors were then completely dissolved in 3 ml of N-methylformamide (NMF) using a magnetic stirrer.

Once dissolved, the solution was carefully filtered into a separate small glass vial that had been pre-rinsed with NMF to remove any potential contaminants. The filtered solution in the small glass vial was then placed in a larger glass vial, where isopropanol was introduced into the gap between the two vials as an antisolvent. The system was set aside to allow the vapor from the isopropanol to enter the small glass vial, facilitating the precipitation and crystallization process. Over approximately 24 hours, this vapor-assisted method promoted the growth of $MAPbBr_3$ single crystals of various sizes, ranging from 100 μm to 1 cm. Crystal sizes greater than 0.3 cm required multiple synthesis attempts by varying the amount of NMF in a trial-and-error process. For our experimental conditions, 3 mL or 4 mL of NMF yielded crystal sizes greater than 0.1 cm (Fig. A.1, A.2).

The single crystals were synthesized partially by the author herself, at the in lab facility at the Department of Physics, University of Virginia and Dr. Grayson C Johnson at the Department of Chemical Engineering, University of Virginia, through collaboration.

Figure A.1: Image of a lab grown $MAPbBr_3$ single crystal.

Figure A.2: Sample holder containing $MAPbBr_3$ single crystal for inelastic neutron scattering measurements.

Appendix B

Vibrational Energy Fraction Calculation

Based on the DFT calculations, we characterized the phonon modes into three different types: inorganic phonon modes, hybrid phonon modes, and organic phonon modes in terms of the vibration energy fraction from different atoms in the following way. The vibrational energy fraction $V_{AT}(s,q)$ is defined as the energy contribution of each atomic type (AT) within the unit cell, encompassing the atoms $\mathrm{Pb}, \mathrm{I}, \mathrm{N}, \mathrm{C}$, and H.

$$V_{AT}(s,q) = \frac{\sum_{i=1}^{n_{AT}} m_i \omega_s(q)^2 \left|u_i(s,q)\right|^2}{\sum_{AT \epsilon \text{ atoms}} \sum_{i=1}^{n_{AT}} m_i \omega_s(q)^2 \left|u_i(s,q)\right|^2} \tag{B.0.1}$$

where s and q represent the phonon mode index and phonon wavevector respectively. n_{AT} is the number of a specific atomic type in the unit cell, $\left|u_i(s,q)\right|^2$ is the mean square displacement of the i-th atom due to the activation of phonon mode s, $\hbar$ is the reduced Planck constant, m_i is the mass of the i-th atom and $\omega_s(q)$ is the eigen frequency of phonon mode s at q.

The vibrational energy fractions at Γ point of the inorganic layer, V_{PbI} were calculated by summing up the vibrational energy fraction of $\mathrm{Pb}\,(V_{Pb})$ and vibrational energy fraction of $\mathrm{I}\,(V_I)$. Fig. B.1 shows the histogram of number of phonon modes with certain inorganic Pb-I energy fractions $[V_{PbI}, V_{PbI} + \Delta V]$ for both systems, where ΔV represents the histogram bin width, which is 2%. The modes are categorized into inorganic phonons modes $V_{PbI} > 70\%$ for (BA$_2$PbI$_4$ and $V_{PbI} > 65\%$ for (PEA))$_2$PbI$_4$, organic phonons when $V_{PbI} < 2\%$, and hybrid phonons in between. The vibrational energy fractions of other atomic types C, H, and N were also calculated, and the contributions from all atomic types to each phonon mode at the Γ point for (BA)$_2$PbI$_4$ and (PEA) $_2$PbI$_4$ are shown in Figs. 3.9, 3.10 panels (D) of the main text. Most of the inorganic phonons lie in the energy range of $\hbar\omega < 10$meV; the hybrid phonons mostly locate in the energy range of 10 ~ 35meV; and the energies of organic phonons usually range from a few tens to hundreds of meV .

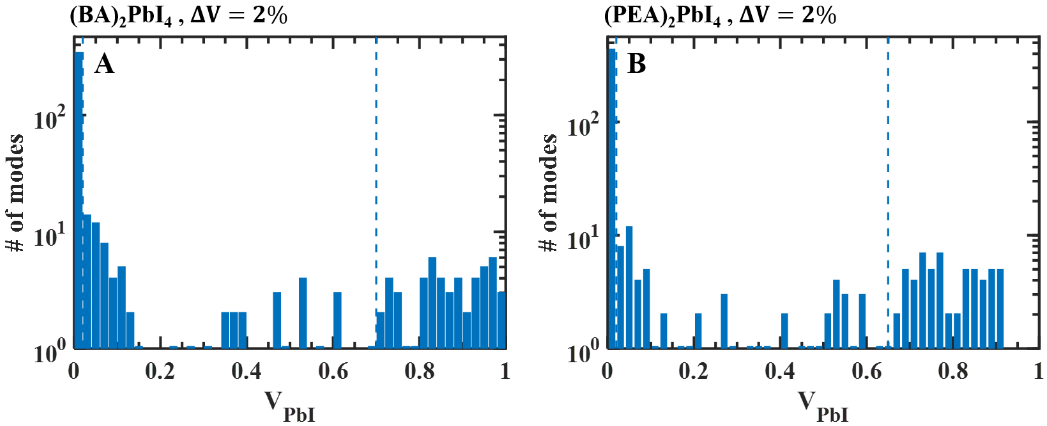

Figure B.1: Statistics of number of phonon modes with different Pb -I vibrational energy fractions for $(BA)_2PbI_4$ and $(PEA)_2PbI_4$. The vertical bars represent the number of phonon modes with certain $\mathrm{Pb-I}$ energy fractions $[V_{PbI}, V_{PbI} + \Delta V]$. The minimum non-zero value is 1 . Vertical dashed lines represent the threshold $\mathrm{Pb - I}$ energy fractions that separate the inorganic modes ($V_{PbI} > 70\%$ for $(BA)_2PbI_4$ and 65% for $(PEA)_2PbI_4$) from organic modes ($V_{PbI} < 2\%$), and hybrid modes in between.

Appendix C

Normalization to Elastic Incoherent Scattering Intensity

The scattered intensity from neutron scattering can be normalized to absolute units by fitting for the elastic incoherent scattering background [143]. Due to the presence of hydrogen in the materials studied in Chapter 1 and Chapter 3 and the strong incoherent scattering background of neutrons from hydrogen, the elastic incoherent scattering background is quite strong. We first integrate $I(Q, \hbar\omega)$ in the elastic energy region to isolate the elastic incoherent scattering.

$$I_{\text{inc}}^{el}(Q) = \int_{-Eres}^{+\text{Eres}} I(Q, \hbar\omega) d(\hbar\omega) \tag{C.0.1}$$

The resulting intensity, dependent on Q, will have the Bragg peaks from the crystal structure along with the elastic incoherent scattering background. We can manually isolate the elastic incoherent scattering background by removing these Bragg peaks or excluding these regions during curve fitting. We can describe the elastic incoherent scattering background, using the equation,

$$I_{\text{inc}}^{el}(Q) = \frac{N}{4\pi} \sum_{j} \sigma_j^{inc} e^{-2W} R_0 \tag{C.0.2}$$

Here R_0 is the resolution volume, e^{-2W} is the Debye Waller factor, σ_j^{inc} is the icoherent scattering length. The Debye-Waller factor is assumed to be 1 at the base temperature, as the temperature-dependent atomic displacements are minimal. Thus, we can extract the normalization constant based on the equation below.

$$NR_0 = 4\pi \cdot A = \frac{I_{inc}^{el}(Q)}{\sum_j \sigma_j^{inc} e^{-2W}} \tag{C.0.3}$$

Appendix D

Photoluminescence: Various Temperature Fitted Curves

Figures D.1 and D.2 displays the fitted curves of photoluminescence (PL) data for various temperatures for $(BA)2PbI_4$ and $(PEA)2PbI_4$, respectively. A Voigt function [169], which is a convolution of Gaussian and Lorentzian functions, was used for the fitting. The Gaussian component represents the instrument resolution function. Therefore, the fitted parameters for the Gaussian part obtained from the lowest temperature curve fitting were fixed for the higher temperature fittings, allowing only the Lorentzian part to vary. Consequently, any spectral broadening indicates effects from the sample.

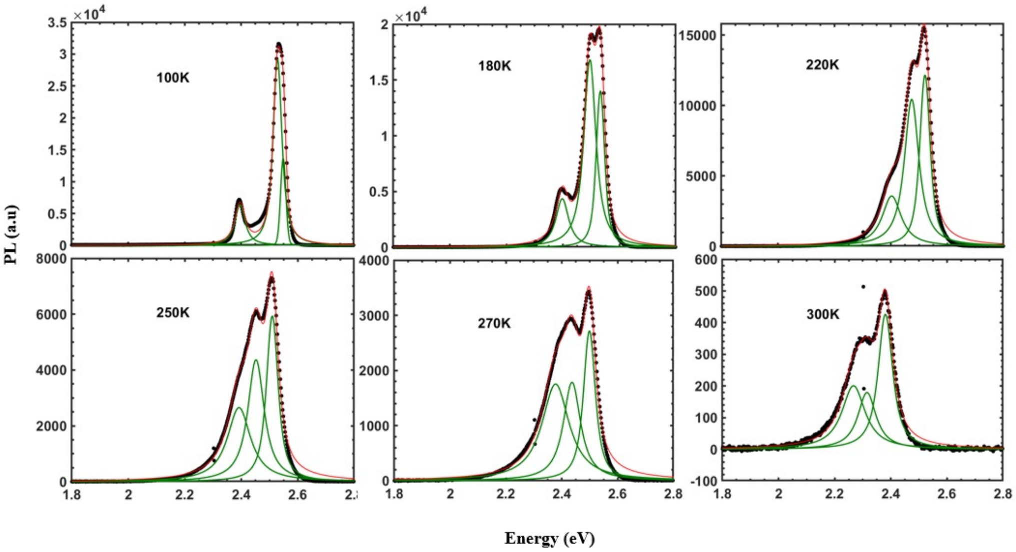

Figure D.1: Temperature dependent fitting and peak splitting for the PL spectra of $(BA)_2PbI_4$

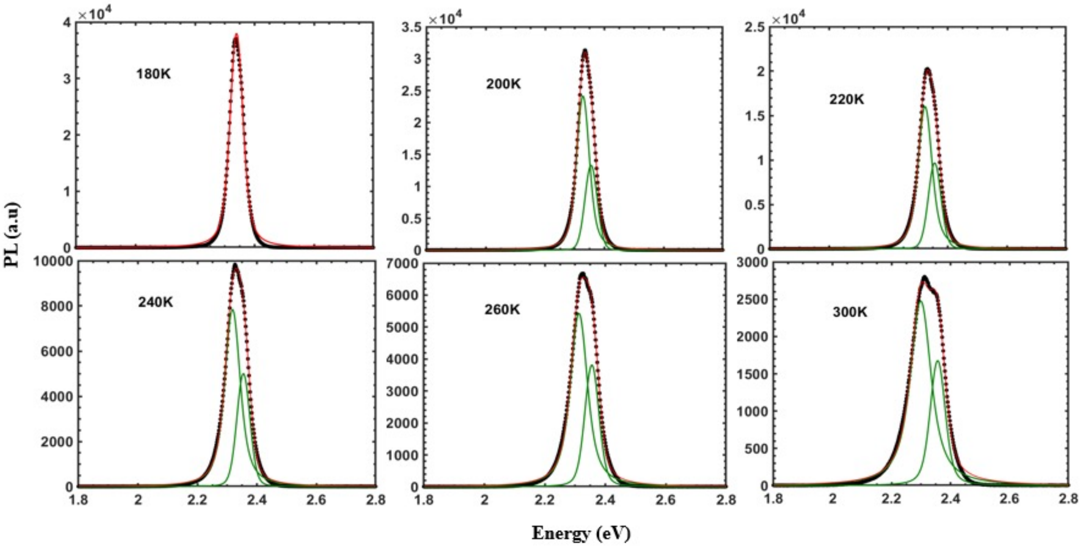

Figure D.2: Temperature dependent fitting and peak splitting for the PL spectra of $(PEA)_2PbI_4$

Appendix E

Average Quantum Dot Seperation Distance Calculations

The wt% of the PbS relative to $CsPbBr_3$ is related to the partial volumes of PbS and $CsPbBr_3$ by

$$\frac{\rho_{\mathrm{PbS}} V_{\mathrm{PbS}}}{\rho_{\mathrm{CsPbBr_3}} V_{\mathrm{CsPbBr_3}}} = \mathrm{wt\%} \tag{E.0.1}$$

where ρ is density and V is volume. A volume percentage is given by

$$V\% = \frac{V_{\mathrm{PbS}}}{V_{\mathrm{PbS}} + V_{\mathrm{CsPbBr_3}}} \tag{E.0.2}$$

If we define a term, α, to describe the ratio of volumes of PbS and $CsPbBr_3$ required for a given wt %, we find

$$\alpha[\mathrm{wt\%}] = \frac{V_{\mathrm{PbS}}}{V_{\mathrm{CsPbBr_3}}} = \frac{\rho_{\mathrm{CsPbBr_3}}}{\rho_{\mathrm{PbS}}} \cdot \mathrm{wt\%} \tag{E.0.3}$$

Note that wt% here is the weight of PbS only. To convert from the experimental parameter, we assumed that the measured weight has only 50% of the organic ligands. A total volume of material, V_{tot}, is defined as the sum of partial volumes and can be related to the percentage of volume according to

$$V_{\mathrm{tot}} = V_{\mathrm{PbS}} \cdot \frac{\alpha[\mathrm{wt\%}] + 1}{\alpha[\mathrm{wt\%}]} \tag{E.0.4}$$

Since we know the approximate volume of the PbS QDs from TEM images from a previous study [35], we can calculate the total volume required to encapsulate a single QD to achieve a given wt%. Taking the cubic root of this volume gives the distance between particles calculated in Figure 4.7. These calculations were performed in collaboration with Dr. Grayson C Johnson from the department of Chemical Engineering.

Appendix F

Diffuse X-Ray Scattering: Various Temperature Fitted Curves

Figure F.1 displays the various temperature-fit curves using the Voigt function for the intensity of X-ray diffuse scattering across the three structural phases of $MAPbBr_3$: orthorhombic ($T = 100$ K), tetragonal ($T = 200$ K) and cubic ($T = 300$ K) at the R, M and X points. The details of a Voigt function is mentioned in Appendix D.

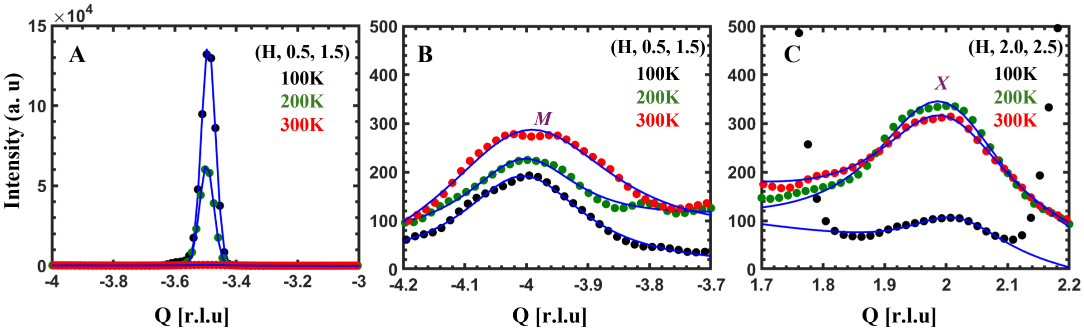

Figure F.1: Temperature dependent fitting for X-Ray diffuse scattering of $MAPbBr_3$ at (A) R point, (B) M point and (C) X point. The blue line represent the fitted curves for all the temperatures.

Appendix G

Inelastic Neutron Scattering: Various Temperature-fitted Curves

Figure G.1 displays the various temperature fitted curves using Voigt function for the intensity of inelastic neutron scattering across all the three structural phases of $\mathrm{MAPbBr_3}$: orthorhombic ($T = 80$ K), tetragonal ($T = 200$ K), and cubic ($T = 300$ K) at the R, M, and X points. The details of a Voigt function is mentioned in Appendix D.

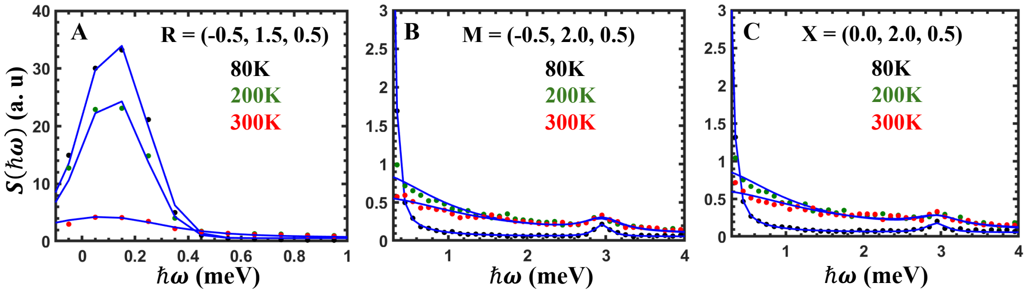

Figure G.1: Temperature dependent fitting for inelastic neutron scattering of $\mathrm{MAPbBr_3}$ at (A) R point, (B) M point and (C) X point. The blue line represent the fitted curves for all the temperatures. The chosen Q integration range was K=[1.4, 1.6] $\mathrm{\AA^{-1}}$ in the path [-0.5, K, 0.5] for R point, H=[-0.55, -0.45] $\mathrm{\AA^{-1}}$ in the path [H, 2, 0.5] for M point and H=[-0.05, 0.05] $\mathrm{\AA^{-1}}$ in the path [H, 2, 0.5] for X point.

Bibliography

[1] A. Mei, X. Li, L. Liu, Z. Ku, T. Liu, Y. Rong, M. Xu, M. Hu, J. Chen, Y. Yang, *et al.*, "A hole-conductor–free, fully printable mesoscopic perovskite solar cell with high stability," *science*, vol. 345, no. 6194, pp. 295–298, 2014.

[2] E. H. Jung, N. J. Jeon, E. Y. Park, C. S. Moon, T. J. Shin, T.-Y. Yang, J. H. Noh, and J. Seo, "Efficient, stable and scalable perovskite solar cells using poly (3-hexylthiophene)," *Nature*, vol. 567, no. 7749, pp. 511–515, 2019.

[3] W. S. Yang, B.-W. Park, E. H. Jung, N. J. Jeon, Y. C. Kim, D. U. Lee, S. S. Shin, J. Seo, E. K. Kim, J. H. Noh, *et al.*, "Iodide management in formamidinium-lead-halide–based perovskite layers for efficient solar cells," *Science*, vol. 356, no. 6345, pp. 1376–1379, 2017.

[4] Q. Jiang, Y. Zhao, X. Zhang, X. Yang, Y. Chen, Z. Chu, Q. Ye, X. Li, Z. Yin, and J. You, "Surface passivation of perovskite film for efficient solar cells," *Nature Photonics*, vol. 13, no. 7, pp. 460–466, 2019.

[5] S. Yang, S. Chen, E. Mosconi, Y. Fang, X. Xiao, C. Wang, Y. Zhou, Z. Yu, J. Zhao, Y. Gao, *et al.*, "Stabilizing halide perovskite surfaces for solar cell operation with wide-bandgap lead oxysalts," *Science*, vol. 365, no. 6452, pp. 473–478, 2019.

[6] T. M. Brenner, D. A. Egger, L. Kronik, G. Hodes, and D. Cahen, "Hybrid organic—inorganic perovskites: low-cost semiconductors with intriguing charge-transport properties," *Nature Reviews Materials*, vol. 1, no. 1, pp. 1–16, 2016.

[7] W. Xu, Q. Hu, S. Bai, C. Bao, Y. Miao, Z. Yuan, T. Borzda, A. J. Barker, E. Tyukalova, Z. Hu, *et al.*, "Rational molecular passivation for high-performance perovskite light-emitting diodes," *Nature Photonics*, vol. 13, no. 6, pp. 418–424, 2019.

[8] L. N. Quan, F. P. García de Arquer, R. P. Sabatini, and E. H. Sargent, "Perovskites for light emission," *Advanced Materials*, vol. 30, no. 45, p. 1801996, 2018.

[9] Z.-K. Tan, R. S. Moghaddam, M. L. Lai, P. Docampo, R. Higler, F. Deschler, M. Price, A. Sadhanala, L. M. Pazos, D. Credgington, *et al.*, "Bright light-emitting diodes based on organometal halide perovskite," *Nature nanotechnology*, vol. 9, no. 9, pp. 687–692, 2014.

[10] G. Xing, N. Mathews, S. S. Lim, N. Yantara, X. Liu, D. Sabba, M. Grätzel, S. Mhaisalkar, and T. C. Sum, "Low-temperature solution-processed wavelength-tunable perovskites for lasing," *Nature materials*, vol. 13, no. 5, pp. 476–480, 2014.

[11] H. Zhu, Y. Fu, F. Meng, X. Wu, Z. Gong, Q. Ding, M. V. Gustafsson, M. T. Trinh, S. Jin, and X. Zhu, "Lead halide perovskite nanowire lasers with low lasing thresholds and high quality factors," *Nature materials*, vol. 14, no. 6, pp. 636–642, 2015.

[12] C. Li, H. Wang, F. Wang, T. Li, M. Xu, H. Wang, Z. Wang, X. Zhan, W. Hu, and L. Shen, "Ultrafast and broadband photodetectors based on a perovskite/organic bulk heterojunction for large-dynamic-range imaging," *Light: Science & Applications*, vol. 9, no. 1, p. 31, 2020.

[13] H. Jing, R. Peng, R.-M. Ma, J. He, Y. Zhou, Z. Yang, C.-Y. Li, Y. Liu, X. Guo, Y. Zhu, *et al.*, "Flexible ultrathin single-crystalline perovskite photodetector," *Nano letters*, vol. 20, no. 10, pp. 7144–7151, 2020.

[14] P. D. Dissanayake, K. M. Yeom, B. Sarkar, D. S. Alessi, D. Hou, J. Rinklebe, J. H. Noh, and Y. S. Ok, "Environmental impact of metal halide perovskite solar cells and potential mitigation strategies: A critical review," *Environmental Research*, vol. 219, p. 115066, 2023.

[15] W. Xiang, S. F. Liu, and W. Tress, "A review on the stability of inorganic metal halide perovskites: challenges and opportunities for stable solar cells," *Energy & Environmental Science*, vol. 14, no. 4, pp. 2090–2113, 2021.

[16] S. Sharma, K. K. Jain, and A. Sharma, "Solar cells: in research and applications—a review," *Materials Sciences and Applications*, vol. 6, no. 12, pp. 1145–1155, 2015.

[17] C. McCombie and M. Jefferson, “Renewable and nuclear electricity: Comparison of environmental impacts,” *Energy Policy*, vol. 96, pp. 758–769, 2016.

[18] J. D. Mariano, F. R. Santos, G. W. Brito, J. U. Junior, and E. F. C. Junior, “Hydro, thermal and photovoltaic power plants: A comparison between electric power generation, environmental impacts and co2 emissions in the brazilian scenario,” *International Journal of Energy and Environment*, vol. 7, no. 4, p. 347, 2016.

[19] M. V. Dambhare, B. Butey, and S. Moharil, “Solar photovoltaic technology: A review of different types of solar cells and its future trends,” in *Journal of Physics: Conference Series*, vol. 1913, p. 012053, IOP Publishing, 2021.

[20] G.-W. Kim and A. Petrozza, “Defect tolerance and intolerance in metal-halide perovskites,” *Advanced Energy Materials*, vol. 10, no. 37, p. 2001959, 2020.

[21] Y. Fu, H. Zhu, J. Chen, M. P. Hautzinger, X.-Y. Zhu, and S. Jin, “Metal halide perovskite nanostructures for optoelectronic applications and the study of physical properties,” *Nature Reviews Materials*, vol. 4, no. 3, pp. 169–188, 2019.

[22] S. D. Stranks and H. J. Snaith, “Metal-halide perovskites for photovoltaic and light-emitting devices,” *Nature nanotechnology*, vol. 10, no. 5, pp. 391–402, 2015.

[23] S.-T. Ha, R. Su, J. Xing, Q. Zhang, and Q. Xiong, “Metal halide perovskite nanomaterials: synthesis and applications,” *Chemical science*, vol. 8, no. 4, pp. 2522–2536, 2017.

[24] S. K. Yadav, G. K. Grandhi, D. P. Dubal, J. C. de Mello, M. Otyepka, R. Zbořil, R. A. Fischer, and K. Jayaramulu, “Metal halide perovskite@ metal-organic framework hybrids: Synthesis, design, properties, and applications,” *Small*, vol. 16, no. 47, p. 2004891, 2020.

[25] National Renewable Energy Laboratory, “Cell efficiency.” `https://www.nrel.gov/pv/cell-efficiency.html`, n.d. Accessed: 2024-09-13.

[26] S. Derenzo, M. Weber, E. Bourret-Courchesne, and M. Klintenberg, “The quest for the ideal inorganic scintillator,” *Nuclear Instruments and Methods in Physics Research Section A: Accelerators, Spectrometers, Detectors and Associated Equipment*, vol. 505, no. 1-2, pp. 111–117, 2003.

[27] S. Kasap, J. B. Frey, G. Belev, O. Tousignant, H. Mani, J. Greenspan, L. Laperriere, O. Bubon, A. Reznik, G. DeCrescenzo, *et al.*, "Amorphous and polycrystalline photoconductors for direct conversion flat panel x-ray image sensors," *Sensors*, vol. 11, pp. 5112–5157, 2011.

[28] J. Glodo, Y. Wang, R. Shawgo, C. Brecher, R. H. Hawrami, J. Tower, and K. S. Shah, "New developments in scintillators for security applications," *Physics Procedia*, vol. 90, pp. 285–290, 2017.

[29] D. Yu, P. Wang, F. Cao, Y. Gu, J. Liu, Z. Han, B. Huang, Y. Zou, X. Xu, and H. Zeng, "Two-dimensional halide perovskite as β-ray scintillator for nuclear radiation monitoring," *Nature Communications*, vol. 11, no. 1, p. 3395, 2020.

[30] J. Zhao, L. Zhao, Y. Deng, X. Xiao, Z. Ni, S. Xu, and J. Huang, "Perovskite-filled membranes for flexible and large-area direct-conversion x-ray detector arrays," *Nature Photonics*, vol. 14, no. 10, pp. 612–617, 2020.

[31] S. Kasap, "X-ray sensitivity of photoconductors: application to stabilized a-se," *Journal of physics D: Applied physics*, vol. 33, no. 21, p. 2853, 2000.

[32] A. Jana, S. Cho, S. A. Patil, A. Meena, Y. Jo, V. G. Sree, Y. Park, H. Kim, H. Im, and R. A. Taylor, "Perovskite: Scintillators, direct detectors, and x-ray imagers," *Materials Today*, vol. 55, pp. 110–136, 2022.

[33] M. Nikl, "Scintillation detectors for x-rays," *Measurement Science and Technology*, vol. 17, no. 4, p. R37, 2006.

[34] Z. Lin, S. Lv, Z. Yang, J. Qiu, and S. Zhou, "Structured scintillators for efficient radiation detection," *Advanced science*, vol. 9, no. 2, p. 2102439, 2022.

[35] A. M. Conley, E. S. Sarabamoun, K. A. Dagnall, L. U. Yoon, H. S. Rajeev, S.-H. Lee, and J. J. Choi, "Quantum-dot-doped lead halide perovskites for ionizing radiation detection," *ACS Applied Optical Materials*, vol. 1, no. 3, pp. 715–723, 2023.

[36] Q. Chen, J. Wu, X. Ou, B. Huang, J. Almutlaq, A. A. Zhumekenov, X. Guan, S. Han, L. Liang, Z. Yi, *et al.*, "All-inorganic perovskite nanocrystal scintillators," *Nature*, vol. 561, no. 7721, pp. 88–93, 2018.

[37] A. Wibowo, M. A. K. Sheikh, L. J. Diguna, M. B. Ananda, M. A. Marsudi, A. Arramel, S. Zeng, L. J. Wong, and M. D. Birowosuto, "Development and

challenges in perovskite scintillators for high-resolution imaging and timing applications," *Communications Materials*, vol. 4, no. 1, p. 21, 2023.

[38] M. D. Birowosuto, P. Dorenbos, C. Van Eijk, K. Krämer, and H. Güdel, "High-light-output scintillator for photodiode readout: Lui3: Ce3+," *Journal of applied physics*, vol. 99, no. 12, 2006.

[39] A. Xie, F. Maddalena, M. E. Witkowski, M. Makowski, B. Mahler, W. Drozdowski, S. V. Springham, P. Coquet, C. Dujardin, M. D. Birowosuto, *et al.*, "Library of two-dimensional hybrid lead halide perovskite scintillator crystals," *Chemistry of Materials*, vol. 32, no. 19, pp. 8530–8539, 2020.

[40] K. A. Dagnall, A. M. Conley, L. U. Yoon, H. S. Rajeev, S.-H. Lee, and J. J. Choi, "Ytterbium-doped cesium lead chloride perovskite as an x-ray scintillator with high light yield," *ACS omega*, vol. 7, no. 24, pp. 20968–20974, 2022.

[41] R. Ali and M. Yashima, "Space group and crystal structure of the perovskite catio3 from 296 to 1720 k," *Journal of Solid State Chemistry*, vol. 178, no. 9, pp. 2867–2872, 2005.

[42] Y. Han, S. Yue, and B.-B. Cui, "Low-dimensional metal halide perovskite crystal materials: structure strategies and luminescence applications," *Advanced Science*, vol. 8, no. 15, p. 2004805, 2021.

[43] C. Ge, Y. Xue, L. Li, B. Tang, and H. Hu, "Recent progress in 2d/3d multidimensional metal halide perovskites solar cells," *Frontiers in Materials*, vol. 7, p. 601179, 2020.

[44] M. Sakata, T. Nishiwaki, and J. Harada, "Neutron diffraction study of the structure of cubic cspbbr3," *Journal of the Physical Society of Japan*, vol. 47, no. 1, pp. 232–233, 1979.

[45] L. Qiu, S. He, L. K. Ono, and Y. Qi, "Progress of surface science studies on abx3-based metal halide perovskite solar cells," *Advanced Energy Materials*, vol. 10, no. 13, p. 1902726, 2020.

[46] N. Ashari-Astani, S. Meloni, A. H. Salavati, G. Palermo, M. Gratzel, and U. Rothlisberger, "Computational characterization of the dependence of halide perovskite effective masses on chemical composition and structure," *The Journal of Physical Chemistry C*, vol. 121, no. 43, pp. 23886–23895, 2017.

[47] G. Giorgi, J.-I. Fujisawa, H. Segawa, and K. Yamashita, “Cation role in structural and electronic properties of 3d organic–inorganic halide perovskites: A dft analysis,” *The Journal of Physical Chemistry C*, vol. 118, no. 23, pp. 12176–12183, 2014.

[48] M. Bokdam, J. Lahnsteiner, and D. Sarma, “Exploring librational pathways with on-the-fly machine-learning force fields: Methylammonium molecules in mapbx3 (x= i, br, cl) perovskites,” *The Journal of Physical Chemistry C*, vol. 125, no. 38, pp. 21077–21086, 2021.

[49] K. Momma and F. Izumi, “Vesta 3 for three-dimensional visualization of crystal, volumetric and morphology data,” *Journal of applied crystallography*, vol. 44, no. 6, pp. 1272–1276, 2011.

[50] C. C. Stoumpos, D. H. Cao, D. J. Clark, J. Young, J. M. Rondinelli, J. I. Jang, J. T. Hupp, and M. G. Kanatzidis, “Ruddlesden–popper hybrid lead iodide perovskite 2d homologous semiconductors,” *Chemistry of Materials*, vol. 28, no. 8, pp. 2852–2867, 2016.

[51] H. Tsai, W. Nie, J.-C. Blancon, C. C. Stoumpos, R. Asadpour, B. Harutyunyan, A. J. Neukirch, R. Verduzco, J. J. Crochet, S. Tretiak, *et al.*, “High-efficiency two-dimensional ruddlesden–popper perovskite solar cells,” *Nature*, vol. 536, no. 7616, pp. 312–316, 2016.

[52] D. H. Cao, C. C. Stoumpos, O. K. Farha, J. T. Hupp, and M. G. Kanatzidis, “2d homologous perovskites as light-absorbing materials for solar cell applications,” *Journal of the American Chemical Society*, vol. 137, no. 24, pp. 7843–7850, 2015.

[53] M. Baranowski and P. Plochocka, “Excitons in metal-halide perovskites,” *Advanced Energy Materials*, vol. 10, no. 26, p. 1903659, 2020.

[54] A. Létoublon, S. Paofai, B. Ruffle, P. Bourges, B. Hehlen, T. Michel, C. Ecolivet, O. Durand, S. Cordier, C. Katan, *et al.*, “Elastic constants, optical phonons, and molecular relaxations in the high temperature plastic phase of the ch3nh3pbbr3 hybrid perovskite,” *The journal of physical chemistry letters*, vol. 7, no. 19, pp. 3776–3784, 2016.

[55] Y. Guo, O. Yaffe, D. W. Paley, A. N. Beecher, T. D. Hull, G. Szpak, J. S. Owen, L. E. Brus, and M. A. Pimenta, “Interplay between organic cations and

inorganic framework and incommensurability in hybrid lead-halide perovskite ch 3 nh 3 pbbr 3," *Physical Review Materials*, vol. 1, no. 4, p. 042401, 2017.

[56] Z. Li, Y. Chen, and C. Burda, "Photoexcited dynamics in metal halide perovskites: From relaxation mechanisms to applications," *The Journal of Physical Chemistry C*, vol. 123, no. 6, pp. 3255–3269, 2019.

[57] S. G. Motti, M. Kober-Czerny, M. Righetto, P. Holzhey, J. Smith, H. Kraus, H. J. Snaith, M. B. Johnston, and L. M. Herz, "Exciton formation dynamics and band-like free charge-carrier transport in 2d metal halide perovskite semiconductors," *Advanced Functional Materials*, vol. 33, no. 32, p. 2300363, 2023.

[58] B. A. Gregg, "The photoconversion mechanism of excitonic solar cells," *MRS bulletin*, vol. 30, no. 1, pp. 20–22, 2005.

[59] A. Moyez, A. Dhar, P. Sarkar, H. S. Jung, and S. Roy, "A review of the multiple exciton generation in photovoltaics," *Reviews in Advanced Sciences and Engineering*, vol. 5, no. 1, pp. 51–64, 2016.

[60] A. Kitai, *Principles of Solar Cells, LEDs and Diodes: The role of the PN junction*. John Wiley & Sons, 2011.

[61] O. Yaffe, Y. Guo, L. Z. Tan, D. A. Egger, T. Hull, C. C. Stoumpos, F. Zheng, T. F. Heinz, L. Kronik, M. G. Kanatzidis, *et al.*, "Local polar fluctuations in lead halide perovskite crystals," *Physical review letters*, vol. 118, no. 13, p. 136001, 2017.

[62] K. Miyata, D. Meggiolaro, M. T. Trinh, P. P. Joshi, E. Mosconi, S. C. Jones, F. De Angelis, and X.-Y. Zhu, "Large polarons in lead halide perovskites," *Science advances*, vol. 3, no. 8, p. e1701217, 2017.

[63] D. A. Egger, A. Bera, D. Cahen, G. Hodes, T. Kirchartz, L. Kronik, R. Lovrincic, A. M. Rappe, D. R. Reichman, and O. Yaffe, "What remains unexplained about the properties of halide perovskites?," *Advanced Materials*, vol. 30, no. 20, p. 1800691, 2018.

[64] A. Forde, S. Tretiak, and A. J. Neukirch, "Dielectric screening and charge-transfer in 2d lead-halide perovskites for reduced exciton binding energies," *Nano Letters*, vol. 23, no. 24, pp. 11586–11592, 2023.

[65] K. R. Hansen, C. Y. Wong, C. E. McClure, B. Romrell, L. Flannery, D. Powell, K. Garden, A. Berzansky, M. Eggleston, D. J. King, *et al.*, "Mechanistic origins

of excitonic properties in 2d perovskites: Implications for exciton engineering," *Matter*, vol. 6, no. 10, pp. 3463–3482, 2023.

[66] B. Cheng, T.-Y. Li, P. Maity, P.-C. Wei, D. Nordlund, K.-T. Ho, D.-H. Lien, C.-H. Lin, R.-Z. Liang, X. Miao, *et al.*, "Extremely reduced dielectric confinement in two-dimensional hybrid perovskites with large polar organics," *Communications Physics*, vol. 1, no. 1, p. 80, 2018.

[67] J. V. Passarelli, C. M. Mauck, S. W. Winslow, C. F. Perkinson, J. C. Bard, H. Sai, K. W. Williams, A. Narayanan, D. J. Fairfield, M. P. Hendricks, *et al.*, "Tunable exciton binding energy in 2d hybrid layered perovskites through donor–acceptor interactions within the organic layer," *Nature chemistry*, vol. 12, no. 8, pp. 672–682, 2020.

[68] C. C. Chan, K. Fan, H. Wang, Z. Huang, D. Novko, K. Yan, J. Xu, W. C. Choy, I. Lončarić, and K. S. Wong, "Uncovering the electron-phonon interplay and dynamical energy-dissipation mechanisms of hot carriers in hybrid lead halide perovskites," *Advanced Energy Materials*, vol. 11, no. 9, p. 2003071, 2021.

[69] T. Chen, W.-L. Chen, B. J. Foley, J. Lee, J. P. Ruff, J. P. Ko, C. M. Brown, L. W. Harriger, D. Zhang, C. Park, *et al.*, "Origin of long lifetime of band-edge charge carriers in organic–inorganic lead iodide perovskites," *Proceedings of the National Academy of Sciences*, vol. 114, no. 29, pp. 7519–7524, 2017.

[70] M. Birowosuto, D. Cortecchia, W. Drozdowski, K. Brylew, W. Lachmanski, A. Bruno, and C. Soci, "X-ray scintillation in lead halide perovskite crystals," *Scientific reports*, vol. 6, no. 1, p. 37254, 2016.

[71] M. Kobayashi, K. Omata, S. Sugimoto, Y. Tamagawa, T. Kuroiwa, H. Asada, H. Takeuchi, and S. Kondo, "Scintillation characteristics of cspbcl3 single crystals," *Nuclear Instruments and Methods in Physics Research Section A: Accelerators, Spectrometers, Detectors and Associated Equipment*, vol. 592, no. 3, pp. 369–373, 2008.

[72] Z. Yang, J. Song, H. Zeng, and M. Wang, "Organic composition tailored perovskite solar cells and light-emitting diodes: perspectives and advances," *Materials Today Energy*, vol. 14, p. 100338, 2019.

[73] C. Zheng and F. Zheng, "Carrier transport in 2d hybrid organic-inorganic perovskites: the role of spacer molecules," *The Journal of Physical Chemistry Letters*, vol. 15, no. 5, pp. 1254–1263, 2024.

[74] C. C. Stoumpos, C. D. Malliakas, and M. G. Kanatzidis, “Semiconducting tin and lead iodide perovskites with organic cations: phase transitions, high mobilities, and near-infrared photoluminescent properties,” *Inorganic chemistry*, vol. 52, no. 15, pp. 9019–9038, 2013.

[75] K. Wang, Z. Jin, L. Liang, H. Bian, D. Bai, H. Wang, J. Zhang, Q. Wang, and S. Liu, “All-inorganic cesium lead iodide perovskite solar cells with stabilized efficiency beyond 15%,” *Nature communications*, vol. 9, no. 1, p. 4544, 2018.

[76] J. D. Ziegler, K.-Q. Lin, B. Meisinger, X. Zhu, M. Kober-Czerny, P. K. Nayak, C. Vona, T. Taniguchi, K. Watanabe, C. Draxl, *et al.*, “Excitons at the phase transition of 2d hybrid perovskites,” *ACS Photonics*, vol. 9, no. 11, pp. 3609–3616, 2022.

[77] M. Dyksik, H. Duim, X. Zhu, Z. Yang, M. Gen, Y. Kohama, S. Adjokatse, D. K. Maude, M. A. Loi, D. A. Egger, *et al.*, “Broad tunability of carrier effective masses in two-dimensional halide perovskites,” *ACS Energy Letters*, vol. 5, no. 11, pp. 3609–3616, 2020.

[78] D. Wiedemann, J. Breternitz, D. W. Paley, and S. Schorr, “Hybrid perovskite at full tilt: Structure and symmetry relations of the incommensurately modulated phase of methylammonium lead bromide, mapbbr3,” *The Journal of Physical Chemistry Letters*, vol. 12, no. 9, pp. 2358–2362, 2021.

[79] G. Mannino, I. Deretzis, E. Smecca, A. La Magna, A. Alberti, D. Ceratti, and D. Cahen, “Temperature-dependent optical band gap in cspbbr3, mapbbr3, and fapbbr3 single crystals,” *The journal of physical chemistry letters*, vol. 11, no. 7, pp. 2490–2496, 2020.

[80] H. Lu, H. Zhang, S. Yuan, J. Wang, Y. Zhan, and L. Zheng, “An optical dynamic study of mapbbr 3 single crystals passivated with mapbcl 3/i 3-mapbbr 3 heterojunctions,” *Physical Chemistry Chemical Physics*, vol. 19, no. 6, pp. 4516–4521, 2017.

[81] D. Kim, E. S. Vasileiadou, I. Spanopoulos, M. G. Kanatzidis, and Q. Tu, “In-plane mechanical properties of two-dimensional hybrid organic–inorganic perovskite nanosheets: Structure–property relationships,” *ACS Applied Materials & Interfaces*, vol. 13, no. 27, pp. 31642–31649, 2021.

[82] K. Miyata, T. L. Atallah, and X.-Y. Zhu, “Lead halide perovskites: Crystal-liquid duality, phonon glass electron crystals, and large polaron formation,” *Science Advances*, vol. 3, no. 10, p. e1701469, 2017.

[83] G. Xing, N. Mathews, S. Sun, S. S. Lim, Y. M. Lam, M. Grätzel, S. Mhaisalkar, and T. C. Sum, “Long-range balanced electron-and hole-transport lengths in organic-inorganic ch3nh3pbi3,” *Science*, vol. 342, no. 6156, pp. 344–347, 2013.

[84] Q. Dong, Y. Fang, Y. Shao, P. Mulligan, J. Qiu, L. Cao, and J. Huang, “Electron-hole diffusion lengths¿ 175 μm in solution-grown ch3nh3pbi3 single crystals,” *Science*, vol. 347, no. 6225, pp. 967–970, 2015.

[85] D. Shi, V. Adinolfi, R. Comin, M. Yuan, E. Alarousu, A. Buin, Y. Chen, S. Hoogland, A. Rothenberger, K. Katsiev, *et al.*, “Low trap-state density and long carrier diffusion in organolead trihalide perovskite single crystals,” *Science*, vol. 347, no. 6221, pp. 519–522, 2015.

[86] D. Emin, *Polarons.* Cambridge University Press, 2012.

[87] K. Wang, Z. Jin, L. Liang, H. Bian, H. Wang, J. Feng, Q. Wang, and S. F. Liu, “Chlorine doping for black γ-cspbi3 solar cells with stabilized efficiency beyond 16%,” *Nano energy*, vol. 58, pp. 175–182, 2019.

[88] H.-H. Fang, L. Protesescu, D. M. Balazs, S. Adjokatse, M. V. Kovalenko, and M. A. Loi, “Exciton recombination in formamidinium lead triiodide: nanocrystals versus thin films,” *small*, vol. 13, no. 32, p. 1700673, 2017.

[89] S. Tombe, G. Adam, H. Heilbrunner, D. H. Apaydin, C. Ulbricht, N. S. Sariciftci, C. J. Arendse, E. Iwuoha, and M. C. Scharber, “Optical and electronic properties of mixed halide (x= i, cl, br) methylammonium lead perovskite solar cells,” *Journal of Materials Chemistry C*, vol. 5, no. 7, pp. 1714–1723, 2017.

[90] H. Kim, J. Hunger, E. Cánovas, M. Karakus, Z. Mics, M. Grechko, D. Turchinovich, S. H. Parekh, and M. Bonn, “Direct observation of mode-specific phonon-band gap coupling in methylammonium lead halide perovskites,” *Nature communications*, vol. 8, no. 1, p. 687, 2017.

[91] K.-z. Du, Q. Tu, X. Zhang, Q. Han, J. Liu, S. Zauscher, and D. B. Mitzi, “Two-dimensional lead (ii) halide-based hybrid perovskites templated by acene alkylamines: crystal structures, optical properties, and piezoelectricity,” *Inorganic chemistry*, vol. 56, no. 15, pp. 9291–9302, 2017.

[92] J. E. Post and D. L. Bish, “Rietveld refinement of crystal structures using powder x-ray diffraction data,” *Modern powder diffraction*, vol. 20, pp. 277–308, 1989.

[93] D. Zhang, X. Hu, T. Chen, D. L. Abernathy, R. Kajimoto, M. Nakamura, M. Kofu, B. J. Foley, M. Yoon, J. J. Choi, *et al.*, "Temporally decoherent and spatially coherent vibrations in metal halide perovskites," *Physical Review B*, vol. 102, no. 22, p. 224310, 2020.

[94] N. J. Weadock, T. C. Sterling, J. A. Vigil, A. Gold-Parker, I. C. Smith, B. Ahammed, M. J. Krogstad, F. Ye, D. Voneshen, P. M. Gehring, *et al.*, "The nature of dynamic local order in $ch_3nh_3pbi_3$ and $ch_3nh_3pbbr_3$," *Joule*, vol. 7, no. 5, pp. 1051–1066, 2023.

[95] T. Lanigan-Atkins, X. He, M. J. Krogstad, D. M. Pajerowski, D. L. Abernathy, G. N. M. N. Xu, Z. Xu, D.-Y. Chung, M. G. Kanatzidis, S. Rosenkranz, *et al.*, "Two-dimensional overdamped fluctuations of the soft perovskite lattice in $cspbbr_3$," *Nature Materials*, vol. 20, no. 7, pp. 977–983, 2021.

[96] M. A. Flatken, A. Hoell, R. Wendt, E. Härk, A. Dallmann, A. Prause, J. Pascual, E. Unger, and A. Abate, "Small-angle scattering to reveal the colloidal nature of halide perovskite precursor solutions," *Journal of Materials Chemistry A*, vol. 9, no. 23, pp. 13477–13482, 2021.

[97] C. J. Dahlman, N. R. Venkatesan, P. T. Corona, R. M. Kennard, L. Mao, N. C. Smith, J. Zhang, R. Seshadri, M. E. Helgeson, and M. L. Chabinyc, "Structural evolution of layered hybrid lead iodide perovskites in colloidal dispersions," *ACS nano*, vol. 14, no. 9, pp. 11294–11308, 2020.

[98] G. L. Squires, *Introduction to the theory of thermal neutron scattering.* Courier Corporation, 1996.

[99] N. R. Group, "Vibrational and diffraction analysis of ba_2pbi_4." `https://discovery.phys.virginia.edu/research/groups/nextlab/research/BA2PbI4_vibfraction.html`, 2024. Accessed: 2024-10-06.

[100] K. D. Berry and Y. Diawara, "Neutron detection materials, detector properties, and selection," in *Neutron Detectors for Scattering Applications*, pp. 1–25, Springer, 2023.

[101] J. R. Copley and T. J. Udovic, "Neutron time-of-flight spectroscopy," *Journal of research of the National Institute of Standards and Technology*, vol. 98, no. 1, p. 71, 1993.

[102] M. Bée, *Quasielastic neutron scattering.* Bristol and Philadelphia: Adam Hilger, 1988.

[103] A. J. Jackson, "Introduction to small-angle neutron scattering and neutron reflectometry," *NIST Center for Neutron Research*, pp. 1–24, 2008.

[104] National Institute of Standards and Technology, "Chrns summer school on neutron scattering: Course materials," 2024. Accessed: 2024-10-09.

[105] International Atomic Energy Agency, "Technical document te-1486," 2024.

[106] A. Anderson and F. F. Cleveland, "The raman effect. volume 1: Principles," 1972.

[107] T. Ruf, *Phonon Raman scattering in semiconductors, quantum wells and superlattices*. Springer Tracts in Modern Physics, 1997.

[108] W. H. Weber and R. Merlin, *Raman scattering in materials science*, vol. 42. Springer Science & Business Media, 2013.

[109] T. Welberry and B. Butler, "Interpretation of diffuse x-ray scattering via models of disorder," *Journal of applied crystallography*, vol. 27, no. 3, pp. 205–231, 1994.

[110] H. Jagodzinski, "Diffuse x-ray scattering from crystals," *Progress in crystal growth and characterization*, vol. 14, pp. 47–102, 1987.

[111] T. R. Welberry and T. Weber, "One hundred years of diffuse scattering," *Crystallography Reviews*, vol. 22, no. 1, pp. 2–78, 2016.

[112] M. Trigo, M. Fuchs, J. Chen, M. Jiang, M. Cammarata, S. Fahy, D. M. Fritz, K. Gaffney, S. Ghimire, A. Higginbotham, *et al.*, "Fourier-transform inelastic x-ray scattering from time-and momentum-dependent phonon–phonon correlations," *Nature Physics*, vol. 9, no. 12, pp. 790–794, 2013.

[113] R. Xu and T. C. Chiang, "Determination of phonon dispersion relations by x-ray thermal diffuse scattering," *Zeitschrift für Kristallographie-Crystalline Materials*, vol. 220, no. 12, pp. 1009–1016, 2005.

[114] D. Case and F. R. Manby, "The ornstein–zernike equation in molecular electronic structure theory," *Molecular Physics*, vol. 108, no. 3-4, pp. 307–314, 2010.

[115] X. Gong, O. Voznyy, A. Jain, W. Liu, R. Sabatini, Z. Piontkowski, G. Walters, G. Bappi, S. Nokhrin, O. Bushuyev, *et al.*, "Electron–phonon interaction in efficient perovskite blue emitters," *Nature materials*, vol. 17, no. 6, pp. 550–556, 2018.

[116] K. N. Shinde, S. Dhoble, H. Swart, K. Park, K. N. Shinde, S. Dhoble, H. Swart, and K. Park, "Basic mechanisms of photoluminescence," *Phosphate Phosphors for Solid-State Lighting*, pp. 41–59, 2012.

[117] H. B. Bebb and E. Williams, "Photoluminescence i: theory," in *Semiconductors and semimetals*, vol. 8, pp. 181–320, Elsevier, 1972.

[118] J. S. Klein, C. Sun, and G. Pratx, "Radioluminescence in biomedicine: physics, applications, and models," *Physics in Medicine & Biology*, vol. 64, no. 4, p. 04TR01, 2019.

[119] S. Bicknese, Z. Shahrokh, S. B. Shohet, and A. Verkman, "Single photon radioluminescence. i. theory and spectroscopic properties," *Biophysical journal*, vol. 63, no. 5, pp. 1256–1266, 1992.

[120] S. Zhang, C. Yi, N. Wang, Y. Sun, W. Zou, Y. Wei, Y. Cao, Y. Miao, R. Li, Y. Yin, *et al.*, "Efficient red perovskite light-emitting diodes based on solution-processed multiple quantum wells," *Advanced Materials*, vol. 29, no. 22, p. 1606600, 2017.

[121] B. Traore, L. Pedesseau, L. Assam, X. Che, J.-C. Blancon, H. Tsai, W. Nie, C. C. Stoumpos, M. G. Kanatzidis, S. Tretiak, *et al.*, "Composite nature of layered hybrid perovskites: assessment on quantum and dielectric confinements and band alignment," *ACS nano*, vol. 12, no. 4, pp. 3321–3332, 2018.

[122] C. Katan, N. Mercier, and J. Even, "Quantum and dielectric confinement effects in lower-dimensional hybrid perovskite semiconductors," *Chemical reviews*, vol. 119, no. 5, pp. 3140–3192, 2019.

[123] N. Wang, L. Cheng, R. Ge, S. Zhang, Y. Miao, W. Zou, C. Yi, Y. Sun, Y. Cao, R. Yang, *et al.*, "Perovskite light-emitting diodes based on solution-processed self-organized multiple quantum wells," *Nature Photonics*, vol. 10, no. 11, pp. 699–704, 2016.

[124] Z. He, Y. Liu, Z. Yang, J. Li, J. Cui, D. Chen, Z. Fang, H. He, Z. Ye, H. Zhu, *et al.*, "High-efficiency red light-emitting diodes based on multiple quantum wells of phenylbutylammonium-cesium lead iodide perovskites," *Acs Photonics*, vol. 6, no. 3, pp. 587–594, 2019.

[125] E. Da Como, F. De Angelis, H. Snaith, and A. Walker, *Unconventional Thin Film Photovoltaics.* Royal Society of Chemistry, 2016.

[126] H. S. Rajeev, X. Hu, W.-L. Chen, D. Zhang, T. Chen, M. Kofu, R. Kajimoto, M. Nakamura, A. Z. Chen, M. Yoon, *et al.*, "The influence of structural dynamics in two-dimensional hybrid organic-inorganic perovskites on their photoluminescence efficiency–neutron scattering analysis," *arXiv preprint arXiv:2402.15658*, 2024.

[127] T. Chen, B. J. Foley, B. Ipek, M. Tyagi, J. R. Copley, C. M. Brown, J. J. Choi, and S.-H. Lee, "Rotational dynamics of organic cations in the ch 3 nh 3 pbi 3 perovskite," *Physical chemistry chemical physics*, vol. 17, no. 46, pp. 31278–31286, 2015.

[128] A. S. Bruker and A. Bruker, "Inc., madison, wisconsin, usa, 2004,(b) sheldrick," *Acta Cryst. A*, vol. 46, pp. 467–473, 1990.

[129] K. Nakajima, S. Ohira-Kawamura, T. Kikuchi, M. Nakamura, R. Kajimoto, Y. Inamura, N. Takahashi, K. Aizawa, K. Suzuya, K. Shibata, *et al.*, "Amateras: a cold-neutron disk chopper spectrometer," *Journal of the Physical Society of Japan*, vol. 80, no. Suppl. B, p. SB028, 2011.

[130] R. Kajimoto, M. Nakamura, Y. Inamura, F. Mizuno, K. Nakajima, S. Ohira-Kawamura, T. Yokoo, T. Nakatani, R. Maruyama, K. Soyama, *et al.*, "The fermi chopper spectrometer 4seasons at j-parc," *Journal of the Physical Society of Japan*, vol. 80, no. Suppl. B, p. SB025, 2011.

[131] M. Nakamura, R. Kajimoto, Y. Inamura, F. Mizuno, M. Fujita, T. Yokoo, and M. Arai, "First demonstration of novel method for inelastic neutron scattering measurement utilizing multiple incident energies," *Journal of the Physical Society of Japan*, vol. 78, no. 9, p. 093002, 2009.

[132] G. Kresse and J. Furthmüller, "Efficiency of ab-initio total energy calculations for metals and semiconductors using a plane-wave basis set," *Computational materials science*, vol. 6, no. 1, pp. 15–50, 1996.

[133] G. Kresse and D. Joubert, "From ultrasoft pseudopotentials to the projector augmented-wave method," *Physical review b*, vol. 59, no. 3, p. 1758, 1999.

[134] J. P. Perdew, K. Burke, and M. Ernzerhof, "Generalized gradient approximation made simple," *Physical review letters*, vol. 77, no. 18, p. 3865, 1996.

[135] D. G. Billing and A. Lemmerer, "Synthesis, characterization and phase transitions in the inorganic–organic layered perovskite-type hybrids [(cnh2n+ 1nh3)

2pbi4], n= 4, 5 and 6," *Acta Crystallographica Section B: Structural Science*, vol. 63, no. 5, pp. 735–747, 2007.

[136] Y. Xiao, C. Xue, X. Wang, Y. Liu, Z. Yang, and S. Liu, "Bulk heterostructure ba2pbi4/mapbi3 perovskites for suppressed ion migration to achieve sensitive x-ray detection performance," *ACS Applied Materials & Interfaces*, vol. 14, no. 49, pp. 54867–54875, 2022.

[137] Y. Cao, Y. Wang, Y. Zhang, X. Liu, and J. Lin, "Stable and rapid thermochromic reversibility in acene alkylamine intercalated layered hybrid perovskites," *Materials Today Communications*, vol. 37, p. 107544, 2023.

[138] D. Kowal, M. Makowski, M. Witkowski, R. Calà, M. K. Sheikh, M. H. Mahyuddin, E. Auffray, W. Drozdowski, D. Cortecchia, and M. D. Birowosuto, "Pea2pbi4: fast two-dimensional lead iodide perovskite scintillator with green and red emission," *Materials Today Chemistry*, vol. 29, p. 101455, 2023.

[139] S. Bonomi, V. Armenise, G. Accorsi, S. Colella, A. Rizzo, F. Fracassi, L. Malavasi, and A. Listorti, "The effect of extended ball-milling upon three-dimensional and two-dimensional perovskite crystals properties," *Applied Sciences*, vol. 10, no. 14, p. 4775, 2020.

[140] B. H. Toby and R. B. Von Dreele, "Gsas-ii: the genesis of a modern open-source all-purpose crystallography software package," *Journal of Applied Crystallography*, vol. 46, no. 2, pp. 544–549, 2013.

[141] T. Chen, B. J. Foley, C. Park, C. M. Brown, L. W. Harriger, J. Lee, J. Ruff, M. Yoon, J. J. Choi, and S.-H. Lee, "Entropy-driven structural transition and kinetic trapping in formamidinium lead iodide perovskite," *Science advances*, vol. 2, no. 10, p. e1601650, 2016.

[142] Y. Cheng, L. L. Daemen, A. I. Kolesnikov, and A. J. Ramirez-Cuesta, "Simulation of inelastic neutron scattering spectra using oclimax," *Journal of chemical theory and computation*, vol. 15, no. 3, pp. 1974–1982, 2019.

[143] G. Xu, Z. Xu, and J. Tranquada, "Absolute cross-section normalization of magnetic neutron scattering data," *Review of Scientific Instruments*, vol. 84, no. 8, 2013.

[144] T. Sheikh, V. Nawale, N. Pathoor, C. Phadnis, A. Chowdhury, and A. Nag, "Molecular intercalation and electronic two dimensionality in layered hybrid perovskites," *Angew. Chem.*, vol. 132, pp. 11750–11756, 2020.

[145] R. DeCrescent, X. Du, R. Kennard, N. Venkatesan, C. Dahlman, M. Chabinyc, and J. Schuller, "Even-parity self-trapped excitons lead to magnetic dipole radiation in two-dimensional lead halide perovskites," *ACS Nano*, vol. 14, pp. 8958–8968, 2020.

[146] Y. Wang, C. He, Q. Tan, Z. Tang, L. Huang, L. Liu, J. Yin, Y. Jiang, X. Wang, and A. Pan, "Exciton–phonon coupling in two-dimensional layered $(ba)_2pbi_4$ perovskite microplates," *RSC Adv.*, vol. 13, pp. 5893–5899, 2023.

[147] Q. Du, C. Zhu, Z. Yin, G. Na, C. Cheng, Y. Han, N. Liu, X. Niu, H. Zhou, H. Chen, and L. Zhang, "Stacking effects on electron–phonon coupling in layered hybrid perovskites via microstrain manipulation," *ACS Nano*, vol. 14, pp. 5806–5817, 2020.

[148] J. Han *et al.*, "Hybrid pbs quantum-dot-in-perovskite for high-efficiency perovskite solar cell," *Small*, vol. 14, no. 31, p. 1801016, 2018.

[149] X. Zhang *et al.*, "Inorganic cspbi3 perovskite coating on pbs quantum dot for highly efficient and stable infrared light converting solar cells," *Advanced Energy Materials*, vol. 8, no. 6, p. 1702049, 2018.

[150] Z. Shi *et al.*, "Strategy of solution-processed all-inorganic heterostructure for humidity/temperature-stable perovskite quantum dot light-emitting diodes," *ACS Nano*, vol. 12, no. 2, pp. 1462–1472, 2018.

[151] M. Maczka and M. Ptak, "Temperature-dependent raman studies of $fapbbr_3$ and $mapbbr_3$ perovskites: effect of phase transitions on molecular dynamics and lattice distortion," *Solids*, vol. 3, no. 1, pp. 111–121, 2022.

[152] S. Govinda, B. P. Kore, D. Swain, A. Hossain, C. De, T. N. Guru Row, and D. Sarma, "Critical comparison of fapbx3 and mapbx3 (x= br and cl): how do they differ?," *The Journal of Physical Chemistry C*, vol. 122, no. 25, pp. 13758–13766, 2018.

[153] Y. Yuan and J. Huang, "Hysteresis suppression in perovskite solar cells using a ferroelectric polymer," *Nature materials*, vol. 15, no. 5, pp. 561–567, 2016.

[154] H. KONISHI and M. YAMAKATA, "Crystal structure analysis," 1997.

[155] Rigaku Oxford Diffraction, "CrysAlisPro Software System," 2024. Version 171.43.112a.

[156] O. R. N. L. (ORNL), "Cold Neutron Chopper Spectrometer (CNCS), BL-5, SNS," 2024.

[157] O. R. N. L. (ORNL), "SHIVER: Oak Ridge National Laboratory's Software for Interactive Visualization of Elastic Response," 2024.

[158] O. Arnold, J.-C. Bilheux, J. M. Borreguero, A. Buts, S. I. Campbell, L. Chapon, M. Doucet, N. Draper, R. F. Leal, M. A. Gigg, V. E. Lynch, A. Markvardsen, D. Mikkelson, R. L. Mikkelson, R. Miller, K. Palmen, P. Parker, G. Passos, T. G. Perring, P. F. Peterson, S. Ren, M. A. Reuter, A. T. Savici, J. W. Taylor, R. J. Taylor, R. Tolchenov, W. Zhou, and J. Zikovsky, "Mantid–data analysis and visualization package for neutron scattering and μsr experiments," *Nuclear Instruments and Methods in Physics Research Section A: Accelerators, Spectrometers, Detectors and Associated Equipment*, vol. 764, pp. 156–166, 2014.

[159] A. Ferreira, A. Létoublon, S. Paofai, S. Raymond, C. Ecolivet, B. Rufflé, S. Cordier, C. Katan, M. I. Saidaminov, A. A. Zhumekenov, *et al.*, "Elastic softness of hybrid lead halide perovskites," *Physical review letters*, vol. 121, no. 8, p. 085502, 2018.

[160] A. Ferreira, S. Paofai, A. Létoublon, J. Ollivier, S. Raymond, B. Hehlen, B. Rufflé, S. Cordier, C. Katan, J. Even, *et al.*, "Direct evidence of weakly dispersed and strongly anharmonic optical phonons in hybrid perovskites," *Communications Physics*, vol. 3, no. 1, p. 48, 2020.

[161] A. Gold-Parker, P. M. Gehring, J. M. Skelton, I. C. Smith, D. Parshall, J. M. Frost, H. I. Karunadasa, A. Walsh, and M. F. Toney, "Acoustic phonon lifetimes limit thermal transport in methylammonium lead iodide," *Proceedings of the National Academy of Sciences*, vol. 115, no. 47, pp. 11905–11910, 2018.

[162] N. W. Ashcroft, N. D. Mermin, and S. Rodriguez, "Solid state physics," *American Journal of Physics*, vol. 46, no. 1, pp. 116–117, 1978.

[163] R. Comin, M. K. Crawford, A. H. Said, N. Herron, W. E. Guise, X. Wang, P. S. Whitfield, A. Jain, X. Gong, A. J. McGaughey, *et al.*, "Lattice dynamics and the nature of structural transitions in organolead halide perovskites," *Physical Review B*, vol. 94, no. 9, p. 094301, 2016.

[164] A. N. Beecher, O. E. Semonin, J. M. Skelton, J. M. Frost, M. W. Terban, H. Zhai, A. Alatas, J. S. Owen, A. Walsh, and S. J. Billinge, "Direct observation

of dynamic symmetry breaking above room temperature in methylammonium lead iodide perovskite," *ACS energy Letters*, vol. 1, no. 4, pp. 880–887, 2016.

[165] Y. Fujii, S. Hoshino, Y. Yamada, and G. Shirane, "Neutron-scattering study on phase transitions of cspb cl 3," *Physical Review B*, vol. 9, no. 10, p. 4549, 1974.

[166] D. B. Mitzi, "A layered solution crystal growth technique and the crystal structure of $(c_6h_5c_2h_4nh_3)_2pbcl_4$," *Journal of Solid State Chemistry*, vol. 145, no. 2, pp. 694–704, 1999.

[167] B. Zhou, D. Ding, Y. Wang, S. Fang, Z. Liu, J. Tang, H. Li, H. Zhong, B. Tian, and Y. Shi, "A scalable h2o–dmf–dmso solvent synthesis of highly luminescent inorganic perovskite-related cesium lead bromides," *Advanced Optical Materials*, vol. 9, no. 3, p. 2001435, 2021.

[168] R. Muslimawati, M. Manawan, K. Takahashi, Y. Furukawa, and A. Bahtiar, "Single crystal perovskite mapbbr3 prepared by using anti-solvent vapor-assisted crystallization method," in *Journal of Physics: Conference Series*, vol. 2376, p. 012005, IOP Publishing, 2022.

[169] D. Balzar, "Voigt-function model in diffraction line-broadening analysis," *Defect and microstructure analysis by diffraction*, pp. 94–126, 1999.